Chirality in diffractive plasmonic nanostructures

Christian Kuppe

A thesis submitted for the degree of Doctor of Philosophy

University of Bath
Department of Physics
February 2019

Signature of Author .....

(Christian Kuppe)

Abstract

Historically, chirality was mostly studied in molecules over which control is naturally limited. However, the ability to produce artificial, chiral structures with feature sizes smaller than the wavelength of light, allows to execute hitherto unseen control over geometrical parameters which govern the emergence and evolution of the research around chirality.

The presence of chirality in molecules can be measured with light. However, the resulting chiral optical response is typically very weak. Interestingly, it is possible to combine artificially created nanostructures and chiral molecules to enhance the chiral optical response of the latter. Nanostructures which are specifically tailored to enhance the response of a certain molecule are therefore needed.

However, such nanostructures also present a predicament: If the nanostructures themselves are chiral, they will overshadow the chiral optical response of the molecule. If the nanostructures are achiral (non-chiral) they cannot be spectrally tailored to the molecule as they do not yield any chiral optical response in the far-field.

A promising solution is offered by diffractive nanostructures which have been shown to yield extremely large responses. However, previous studies have been limited in scale and a physical explanation for the observed behaviour is still elusive. Developing an experimental apparatus to optically characterise various nanogratings, supported by numerical simulations and mathematical models, this thesis provides both an explanation and the means for chiral sensing in diffracted beams. The apparatus enables the detection of chirality through circular intensity measurements of the light diffracted by such nanogratings. Starting with a proof-of-principle study of higher-order diffraction spectroscopy, various nanograting designs and their far-field responses are investigated. Consequently, the potential of such nanogratings to enhance the response of chiral molecules is demonstrated. Of special interest are racemic nanogratings, i.e. consisting of an equal number of both chiral configurations. The reason for this lies in the fact that racemic nanogratings yield no net chiral optical response but, by means of diffraction spectroscopy, it is possible to unveil such a behaviour in the far-field which is the first time this has been reported. Although the far-field chiral optical response of a racemic nanograting accumulates to a net zero, individual diffracted beams do yield non-zero values and hence can now be spectrally tailored to that of the molecules.

The results of a proof-of-principle study with chiral molecules demonstrate the potential of artificially created nanogratings to become a platform to detect chirality

in molecular films with light. The presented findings contribute to the advancement in the design and characterisation of chiral materials.

Acknowledgements

I would like to take this opportunity to thank my supervisor Dr. Ventsislav K. Valev for making this project possible as well as for your constant support over the years. You started this research group just before I joined the team and made it what it is today with your unique drive and enthusiasm. The sometimes challenging but always interesting work environment you created, forged the team into a highly collaborative and tight-knit group of which I am proud to have been a part of. For starting this journey with me, I am grateful to my fellow team members David Hooper and Joel T. Collins. The kind of team spirit we have developed over the years made you both my valued colleagues as well as good friends. Lately, we have been joined by Alex Murphy and Lukáš Ohnoutek – in this short time you have become friends and I thank you especially for your helpful input to this thesis.

I also thank everyone in the Centre for Photonics and Photonic Materials for creating the most approachable and inspiring atmosphere I could have hoped for. Special thanks go to the technical staff; particularly to Martin Fullick and Paul Reddish. Your depth of expertise and experience helped me to finalise the experimental apparatus. For sparking my initial interest in the chemistry aspect of this project I thank Dr. Fabienne Pradaux-Caggiano and Dr. Dave Carbery. In addition, I would like to thank Dave for our numerous truly inspiring meetings throughout this project, your enthusiasm about science in general and your interest in my work in particular. Dora Răsădean and Dr. Dan Pantoş, I am grateful for all your work and insights in the final part of this project.

I would like to express my gratitude to Dr. Calum Williams who fabricated all nanogratings for this work. Over the years you have been crucial to my development as a scientist and have become a good friend. I thank you for hosting me in Cambridge and visiting Bath in return as well as your constructive feedback on earlier versions of this thesis – it has been a pleasure to work on this project with you.

I would like to express my sincerest thanks to my family. You have always been there for me and knew exactly what I needed: be it emotional support or a reminder of a world apart from physics.

Bhargavi Thakker, from our first year as undergraduates until now, you have been my great friend and made my Bath experience so fantastic – I thank you for your friendship and for your help with this thesis.

My deepest affection and appreciation go to Rebecca Weyers: my partner and companion. You helped me through this often strenuous time with your presence and love. I am forever grateful for your support.

List of Publications

1. C. Kuppe, X. Zheng, C. Williams, J. T. Collins, S. Gordeev, G. A. E. Vandenbosch, V. K. Valev, *Measuring chirality in the far-field from a racemic nanomaterial: diffraction spectroscopy from plasmonic nanogratings*, (2019) submitted

2. C. Kuppe, K. R. Rusimova, L. Ohnoutek, D. Slavov, V. K. Valev, *Review article*, Adv. Opt. Mater. (2019) Invited, in preparation

3. Z. Liu, A. W. A. Murphy, C. Kuppe, D. C. Hooper, V. K. Valev, A. Ilie, *WS2 Nanotubes, 2D Nanomeshes, and 2D In-plane Films Through One Single Chemical Vapor Deposition Route*, (2019) Submitted

4. D. C. Hooper, C. Kuppe, D, Wang, W. Wang, J. Guan, T. W. Odom, V. K. Valev, *Second harmonic spectroscopy of surface lattice resonances*, Nano Lett. 19, 165-172 (2019).

5. J. T. Collins, D. C. Hooper, A. G. Mark, C. Kuppe, V. K. Valev, *Second harmonic generation optical rotation solely attributable to chirality in plasmonic metasurfaces*, ACS Nano 12, 5445-5451 (2018).

6. C. Kuppe, C. Williams, J. You, J. T. Collins, S. N. Gordeev, T. D. Wilkinson, N. C. Panoiu, V. K. Valev, *Circular dichroism in higher-order diffraction beams from chiral quasi-planar nanostructures*, Adv. Opt. Mater. 6, 1800098 (2018).

7. J. T. Collins, C. Kuppe, D. C. Hooper, C. Sibilia, M. Centini, V. K. Valev, *Chirality and chiroptical effects in metal nanostructures: fundamentals and current trends*, Adv. Opt. Mater. 5, 1700182 (2017).

8. Y. Fu, C. Kuppe, V. K. Valev, H. Fu, L. Zhang, J. Chen, *Surface Enhanced Raman Spectroscopy: a Facile and Rapid Method for the Chemical Components Study of Individual Atmospheric Aerosol*, Environ. Sci. Technol. 51, 6260 (2017).

9. D. C. Hooper, A. G. Mark, C. Kuppe, J. T. Collins, P. Fischer, V. K. Valev, *Strong Rotational Anisotropies Affect Nonlinear Chiral Metamaterials*, Adv. Mater. 29, 1605110 (2017).

List of Abbreviations

AFM – Atomic Force Microscope

CB – Circular Birefringence

CD – Circular Dichroism

CPL – Circularly Polarised Light

CID – Circular Intensity Difference

CGH – Computer-Generated Holograms

DBF – Drude-Born-Fedorov

DC – Direct Current

DOE – Diffractive Optical Element

DDO – Dynamic Digital Optics

EBL – Electron Beam Lithography

EOA – Electronic Optical Activity

FDTD – Finite-Difference-Time-Domain

HOE – Holographic Optical Element

LCP – Left Circularly Polarised

LB – Linear Birefringence

LD – Linear Dichroism

LSP – Localised Surface Plasmon

NDI – Naphthalenediimide

OA – Optical Activity

OPO – Optical Parametric Oscillator

OR – Optical Rotation

ORD – Optical Rotatory Dispersion

PEM – Photoelastic Modulator

QWP – Quarter-Waveplate

R – Rectus (right)

RCP – Right Circularly Polarised

RCWA – Rigorous Coupled Wave Analysis

S – Sinister (left)

SEM – Scanning Electron Microscope

SPP – Surface Plasmon Polariton

SWE – Sub-Wavelength Digital Element

TE – Transverse Electric

TM – Transverse Magnetic

UV – Ultraviolet

VOA – Vibrational Optical Activity

Contents

Chapter 1

Introduction

For more than a century, the study of chirality has mostly been limited to the field of chemistry [1]. Chirality refers to the *handedness* of an object and is often associated with an object's twist, which can have a profound influence on the properties of biomolecules [2]. Thus, chirality naturally attracted strong interest from chemistry as well as pharmacology. The handedness of biomolecules can depend on a number of variables, such as the position of individual atoms and its overall structure. While there are numerous parameters influencing chirality, it is difficult to study chirality in this context, as the control over these parameters is limited [3]. That said, chirality can be probed with light by measuring the difference in light-matter interactions with respect to the handedness of the molecule. The observed chiral optical (chiroptical) response can be associated with the geometrical parameters of the molecule. However, chiroptical effects are typically very weak and therefore sparked interest in opportunities to enhance the molecular response and the chiral parameters in general.

The emergence of nanofabrication techniques has become a platform that allows promising possibilities in this regard, since it is now possible to create chiral metal nanostructures with near arbitrary geometry parameters [4]. Metallic nanoparticles can now be fabricated with sizes much smaller than the wavelength of the light, which yield strong chiroptical responses. These strong responses can be used to enhance the response of chiral molecules which are situated in close proximity of two metallic nanoparticles. This enhancement is due to the fact that two metallic nanoparticles can concentrate the electromagnetic fields in the gap between them which consequently couple to the response of the chiral molecule resulting in an intensified response [5].

However, nanoparticles can not only increase the molecular response, but also exhibit a large chiroptical response themselves [6]. Examples for this range from chiral arrangements of two metallic nanorods to larger numbers of nanoparticles and even artificially designed chiral networks. Hence, depending on the design complexity, it

is possible to create an abundance of chiral systems, which allows the study of the emergence and evolution of chirality.

1.1 Motivation

The endeavour for increased miniaturisation has thus led to a paradigm-shift from 'classical' optical equipment to ultra-thin optical devices to manipulate the properties of light and revealed phenomena such as the negative refractive index and superchirality. However, while deep-subwavelength material dimensions are enabling fascinating prospects, interesting opportunities for structures with features comparable to the wavelength of light seem to have been overlooked [7].

In this thesis, the chiroptical behaviour of quasi-planar, chiral and diffractive nanostructures is investigated. Such nanogratings have been shown to exhibit chiroptical responses in their diffracted order beams up to three orders of magnitude stronger than in the zeroth-order diffracted beam. Thus, nanogratings are promising candidates for extremely sensitive chiral sensing applications. Furthermore, previous studies have mostly been limited to the first-order diffracted beams. This thesis aims to fill this research gap by investigating the chiroptical response of various types of gold nanogratings in higher-order diffracted beams. The experimental findings are supported by numerical simulations as well as rigorous theoretical models. In addition, the auspicious prospects of nanogratings as a platform to enhance molecular chiroptical responses are presented, offering the potential for hyper-sensitive chiral sensing devices.

1.2 Organisation

This thesis is divided into four main parts – the theoretical framework (chapter 2), experimental methodology (chapter 3), the research contributions associated with this project (chapters 4 - 6) and a concluding chapter (chapter 7). The theory will outline the background with the main focus on chirality (section 2.1), plasmonics (section 2.2) and diffractive optics (section 2.3). In the experimental methodology chapter, a commercially available circular dichroism spectrometer as a tool to measure chiroptical responses from molecules is investigated and used as a foundation for the development of a laser-based system. The limitations associated with such a design are elaborated and the final apparatus presented. This section is followed by a brief description of the fabrication technique used to produce the nanogratings for this work.

Following the experimental methodology, the main research contributions are presented in three separate chapters. Chapter 4 is a proof-of-principle study demon-

strating the potential of higher-order diffraction spectroscopy for chiral sensing and is based on a published research article. Chapter 5 presents a geometrical study of various nanograting geometries, which ultimately explains how the chiroptical response of racemic nanogratings, consisting of equal amounts of both handednesses, can be measured in the far-field. The work bridges the gap to tailor the response of nanogratings to that of chiral molecules. Chapter 6 presents a proof-of-principle study to demonstrate the potential of racemic nanogratings for hyper-sensitive chiral sensing.

In the concluding chapter, the main findings of this work are summarised and presented in the context of current research. Furthermore, promising prospects for future work based on the given research contributions are discussed.

Chapter 2

Theoretical Background

2.1 Chirality

Section 2.1.5 of this chapter has been adapted from the published review *"Chirality and Chiroptical Effects in Metal Nanostructures: Fundamentals and Current Trends"*, Joel T. Collins et. al. [1]. The adapted section has been written by myself.

2.1.1 Historical origin and definition

In 1811, a scientist called Arago observed that linearly polarised light travelling through a quartz crystal experiences a rotation of its plane of polarisation [8]. Contrary to initial belief, Herschel and Biot soon found that this effect is not limited to quartz crystals, but is also observed in other crystalline structures [1]. Fresnel found that the rotation of the plane of linearly polarised light travelling through certain media can be linked to a difference in refractive indices for left- and right-circularly polarised light. However, it was not until Pasteur in 1848, that it was realised that this rotation is a phenomenon intrinsically linked to the basic structure of the compounds studied. The link between structural symmetry and circularly polarised light was validated by an experiment proving that crystals in their solid state interact with circularly polarised light in the same way as in their dissolved state [1].

Chirality is a word that stems from the Greek word for hand, or *kher*, and was first used to describe this phenomenon by Lord Kelvin in 1904 as *"I call any geometrical figure, or any group of points, chiral, and say that it has chirality, if its image in a plane mirror, ideally realised, cannot be brought to coincide with itself"* [9]. The key aspect lies in the fact that the symmetry of an object can be such that when the mirror image is studied, it looks different to the original – the object is said to exhibit a broken mirror-symmetry. The most notable example for this are hands, which are mirror images but cannot be superimposed via rotational operations. Therefore to distinguish between a chiral object and its mirror image,

the term *enantiomorph* (*enantiomer* for molecules) is used. An enantiomeric pair consists of two enantiomorphs with an opposite twist or *handedness* (left or right). In structurally simple molecules, chirality can be understood in much the same way and the handedness of each enantiomer is given in the molecule's name with the prefix R (*rectus*, Latin for right) or S (*sinister*, Latin for left).

If Lord Kelvin's definition of chirality to study nature is followed, it can be found that chiral objects exist on all length scales. Certain types of galaxies have a spiral-like shape and due to their rotation with respect to the direction of motion are chiral; similarly chirality can be found in phenomena such as hurricanes, whirlpools and can be tracked down to snail shells and even molecules. A prominent example is deoxyribonucleic acid, or DNA, which exhibits chirality with its well-known double helix structure. Interestingly, depending on the type of object, a dominant handedness can be found – in amino acids a left handedness is predominant, which led to the theory of homochirality. This theory proposes that homochirality is crucial to allow efficient biomechanisms [1].

Although chirality as a symmetry property of matter has been known for more than a century, its importance was only realised after the Contergan scandal in the 1950s in Germany. Contergan was designed as a painkiller to reduce the effects of morning sickness for pregnant women. Contergan is based on the molecule thalidomide, which is chiral. While one enantiomer of thalidomide is indeed an effective painkiller, the other enantiomer caused children to be born with no or shortened limbs [10]. Consequently, thousands of affected children were born, serving as gruesome evidence of the lack of understanding at that time.

However, while the Contergan scandal is undoubtedly one of the most well-known chiral medical drugs, there are numerous others. Examples include: Ketamine, with one enantiomer used as an anaesthetic, the other is known to cause hallucinations; Naproxen, which is used as an anti-inflammatory drug, while its other enantiomer causes liver poisoning. Other examples of chiral molecules used as medicines and their differing, sometimes disastrous, effects include: Levodopa (Parkinson's disease; Bacterial infection), Penicillamine (Arthritis; neurotoxic) and Ethambutol (Tuberculosis; blindness) just to name a few [1].

Today, the pharmaceutical industry strives to achieve a final product containing only one enantiomer. Although many studies have shown that conversion of one enantiomer into the other can occur both *in vitro* in the laboratory and *in vivo* in animals as well as humans [11, 12], a guaranteed single pure enantiomer in the production is still crucial for the safe development and use of medical drugs. Such a purity is difficult to achieve, since the process known as *asymmetric catalysis*, i.e. a chemical process favouring the formation of a single enantiomer, is extremely complex and thus not in widespread industrial use [13]. Instead, it is common to

produce an equal amount of both enantiomers – a mixture containing both enantiomers equally is referred to as being *racemic*. Racemic mixtures can subsequently be divided into their individual enantiomers by a process called chiral chromatography. Chiral chromatography has seen steady improvement, resulting in various techniques which can be applied depending on the chiral molecule in question [14]. Although there are various techniques to separate the enantiomers in racemic mixtures, most of them do not work perfectly and generally will still leave a residue of the unwanted enantiomer. The amount of residue can in most cases be reduced by repeating the process multiple times until the product reaches the required level of purity. However, the level of purity is determined by statistical methods. The ambition to find better methods for chiral sensing has therefore gained a lot of attention in recent years [15–18].

2.1.2 Types of chirality

While chirality on the macroscale (galaxies, hands, etc.) and even for simple molecules is rather intuitive, more complex molecules exhibit a form of chirality that is rich in nuances. Generally, chirality is divided into two major types – *intrinsic* and *pseudo-* chirality. Intrinsic chirality refers to the symmetry of the target object and thus refers to the object of interest directly. Different types of intrinsic chirality can be distinguished and depend largely on the complexity of the object. In Figure 2.1 a-f, examples of helical chirality are presented – this type is the nanoscale analog of propellers and spirals; and can be found for molecules as well as for specifically designed nanostructures [3]. A less intuitive example arises when an object is arranged with a certain twist g-i. Small deviations from perfectly straight configurations can result in chirality, which is often the case in naturally occurring molecules and is known as chiral coupling. Supramolecular chirality refers to objects arranged or stacked in a chiral fashion j-l, while it is important to note that the individual elements can be both chiral and achiral to form a chiral unit.

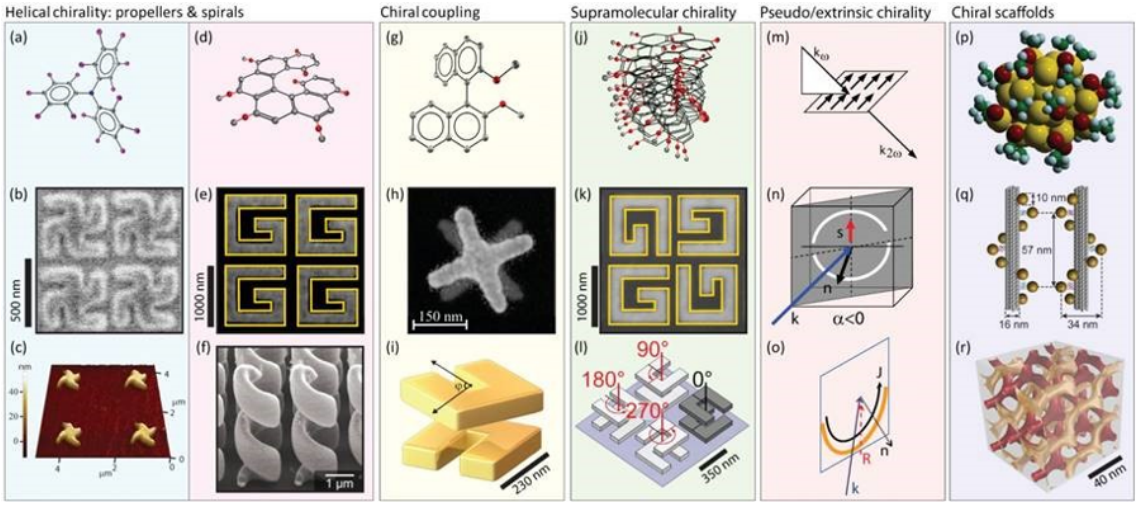

Figure 2.1: Different types of chirality in molecules and nanostructures. Adapted from [3].

Interestingly, studies found that it is possible to measure chirality, even if the sample itself is neither chiral nor arranged in an intrinsically chiral way [19–22]. The chirality was found to originate from the geometry of the experimental setup, or the k-vector (angle of incident light) relative to the sample. This type of chirality is what was previously termed pseudo-chirality and is sometimes also called extrinsic chirality m-o. The last type of chirality that shall be mentioned here are chiral networks or scaffolds p-r. Here, achiral objects can be assembled into large chiral networks.

2.1.3 True and false chirality

From the beginning, vigorous debates erupted about the definition and physical interpretation of chirality and led to what has since been called *true* and *false chirality*. In order to understand the importance of this distinction, it is crucial to understand the underlying physical principles. As previously mentioned, the definition of chirality is that two objects lack mirror-symmetry, i.e. they cannot be superimposed upon rotation. In mathematical terms, this approach is called *parity inversion* (denoted with the operator P), i.e. one or all spatial components are changed and the system checked for invariance. A system is invariant under parity inversion when the equations describing said system are identical under the operation $x = -x$ or equally replacing all spatial coordinates x, y, z, for example by rotating the whole coordinate system.

When testing whether an object is chiral or not, one therefore needs to investigate whether the object exhibits *inversion symmetry*. Inversion symmetry refers to the aforementioned parity, *time-reversal* and *charge conjugation*. Time-reversal (denoted with the operator T) does not refer to true reversal of time, which would be

unphysical, but rather a reverse of motion: imagining a sphere rotating clockwise; under time-reversal it would rotate anti-clockwise. Thus, the concept of true and false chirality is especially important when chirality arises in moving objects, such as charge carriers. Charge conjugation (denoted with the operator C) converts all particles of a system into their antiparticle counterparts and is particularly important for molecular chirality. These three concepts are known as the CPT theorem and are crucial to distinguish true and false chirality [2]. Since this work mainly focusses on larger structures, it will be limited to investigating P and T inversions. In order to distinguish true and false chirality, it is thus necessary to extend the previous definition, to *"True chirality is exhibited by systems existing in two distinct enantiomeric states that are interconverted by space inversion, but not by time reversal combined with any proper spatial rotation"* [2]. It is important to note, that this description specifically addresses moving objects (hence time reversal), and thus the previous definition of chirality is still valid for static objects [2].

The test for true chirality is presented in Figure 2.2. If an object is truly chiral, we should be able to perform parity inversion and time-reversal subsequently and end up with two objects which cannot be superimposed upon rotation.

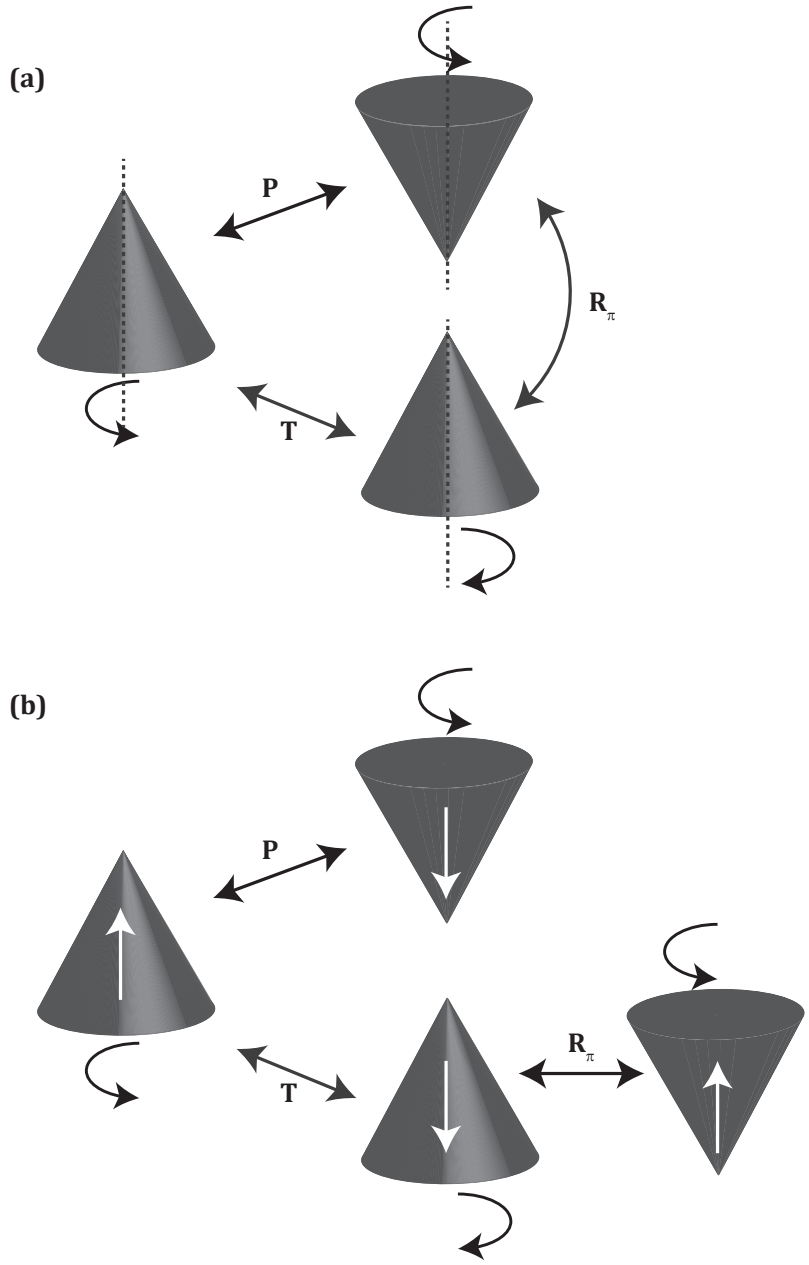

Figure 2.2: Effect of parity inversion **P**, time-reversal **T** and π rotation $\mathbf{R}_\pi$ for a stationary (a) and a moving (b) spinning cone. In the stationary case, the final rotational operation allows to convert one cone into the other, and therefore exhibits false chirality. The direction of the moving cone, however, reverses for the same sequence and thus the final cones are not superimposable and hence are an example of true chirality. Adapted from [2].

Nanoscience, or more specifically the ability to fabricate structures on the nanoscale, has produced ever smaller structures, that have dimensions comparable and even smaller than the wavelength of light used to investigate them. There are structures that are chiral in 2D, also known as planochiral or quasi-planar, which typically have a thickness of a few nanometres (thickness << wavelength). These structures would be falsely chiral – since the enantiomeric counterpart of such a

structure can be flipped upside down, and the two will be identical. True chirality in such cases can be recovered by fabricating planochiral structures on a substrate; this recovers the three-dimensionality due to the creation of additional interfaces [23]. If an 'air-planochiral object-substrate-air' profile is considered, the sample could be flipped upside down and would have an 'air-substrate-planochiral object-air' profile, which would lead to a break of symmetry and hence chirality. In such a case, it is important whether the chiral medium is *reciprocal*. A chiral medium is reciprocal if it interacts with light in the same way when the position of sample and detector are changed, i.e. when the light interacts with the sample from the opposite direction. Historically, a chiral medium is assumed to be reciprocal, however recently, based on chiral effects measured in non-reciprocal media, this definition has been extended [23].

For the scope of this thesis, only one more category will be added to describe a chiral medium – namely whether it is *isotropic*. A medium is optically isotropic if its interaction with light does not depend upon the direction of propagation of the light through the medium. On the other hand, if the medium's functions (for example the dielectric function) depend upon the direction in the medium as well as the position, the medium is called anisotropic [24].

2.1.4 Chiral light

Typically, electromagnetic waves, or simply light waves, are expressed as a plane wave. It is thus known that a plane wave propagating in the $+z$ direction can be expressed as:

$$\vec{E} = \vec{E_0} e^{\mathrm{i}(kz-\omega t)}, \tag{2.1}$$

with E_0 defined as:

$$\vec{E_0} = E_x \hat{x} \cos(kz - \omega t) + E_y \hat{y} \cos(kz - \omega t + \Phi), \tag{2.2}$$

where $\hat{x}$ is the unit vector in the x-direction, equally $\hat{y}$ for the y-direction; k is the wave number, ω is the angular frequency of the wave and t is the time. Φ is the phase difference between the wave components E_x and E_y. The polarisation of the plane wave can take three forms, i.e. linearly, elliptically and circularly polarised. A plane wave is linearly polarised, for example, when $E_x = E_y$ and $\Phi = 0$. The elliptical polarisation is realised when $E_x \neq E_y$ and $\Phi \neq 0$ – thus the polarisation changes in magnitude while rotating in the x-y-plane. Circularly polarised light (CPL) occurs when $E_x = E_y$, while the phase $\Phi = \pm\frac{\pi}{2}$, corresponding to a quarter of a wavelength phase shift. Conventionally, a positive phase shift is referred to as left-circularly polarised (LCP) and similarly a negative phase shift as right-circularly

polarised light (RCP). It is useful to note though, that various conventions are used in the literature which mainly depend on whether the wave is described from the point of view of the source or of the detector.

While linearly polarised light is naturally achiral, CPL is indeed chiral since it exhibits the typical twist and is variant under parity inversion, i.e. it has two distinct enantiomeric forms – LCP and RCP.

2.1.4.1 Light interaction with a chiral medium

A mathematical description is required to appreciate the fundamental effect of chirality on the interaction of light with matter. It is well known that the interaction of light with a dielectric medium is rigorously described by Maxwell's equations. Here, it is assumed that the medium has no unbound charges and Maxwell's equations are represented in their time-harmonic form, such that:

$$\vec{\nabla} \cdot \vec{E} = \rho_{\text{total}}, \tag{2.3a}$$

$$\vec{\nabla} \cdot \vec{B} = 0, \tag{2.3b}$$

$$\vec{\nabla} \times \vec{E} = -\frac{\partial \vec{B}}{\partial t} = -\mathrm{i}\omega\vec{B}, \tag{2.3c}$$

$$\vec{\nabla} \times \vec{H} = \frac{\partial \vec{D}}{\partial t} = \mathrm{i}\omega\vec{D}, \tag{2.3d}$$

where $\vec{E}$ and $\vec{B}$ are the electric and magnetic fields and $\vec{D}$ and $\vec{H}$ their respective auxiliary fields; $\omega = 2\pi f$ is the angular frequency and proportional to the frequency of oscillation f of the electromagnetic wave in the medium [25].

The auxiliary fields are linked to the electric and magnetic fields through the so-called *constitutive relations*, which in their general form are expressed by:

$$\vec{D} = \epsilon\vec{E} + \xi\vec{H}, \tag{2.4a}$$

$$\vec{B} = \mu\vec{H} + \zeta\vec{E}, \tag{2.4b}$$

with $\epsilon = \epsilon_0\epsilon_r$ and $\mu = \mu_0\mu_r$ representing the permittivity and permeability respectively; ξ and ζ are known as the electromagnetic cross-coupling terms and all four terms are material-dependent parameters. The electromagnetic cross-coupling

is nonzero for bi-anisotropic media, which is generally assumed when studying media [1].

These electromagnetic cross-coupling constants are intrinsically linked to the medium's reciprocity, described by the *Tellegen* χ and its chirality parameter κ, also known as the *Pasteur* parameter, such that:

$$\chi - \mathrm{i}\kappa = \frac{\xi}{\sqrt{\epsilon\mu}}, \tag{2.5a}$$

$$\chi + \mathrm{i}\kappa = \frac{\zeta}{\sqrt{\epsilon\mu}}. \tag{2.5b}$$

Historically, this has led to three models to describe the behaviour of chiral media through expressions of the medium's constitutive relations - Tellegen, Pasteur and Post's relations. These relations are linked through the previous set of equations (2.5a – 2.5b) and can thus be treated as equivalent. However, it is important to note that Tellegen and Pasteur's relations make assumptions about the type of material (reciprocity/chirality) and thus are not as general as Posts' relations, which is the reason why the latter forms the starting point of many rigorous studies [26–30].

In table 2.1, these three models are presented and compared to a fourth model – the Drude-Born-Fedorov (DBF) model. It is possible to express each model in terms of the other via Maxwell's equations in a source-free medium and thus it is often stated that they all can be treated as equivalent. However, there are reported situations where the DBF and the other models give differing results [31]. This difference in the predicted behaviour stems from the fact, that in the DBF model the constitutive relations depend on the spatial derivatives of the fields rather than from the introduction of cross-coupling terms. For example, if a chiral homogeneous material matrix is assumed, such that spiral-shaped objects are submerged in a solution and are made of a lossless dielectric, there is no electromagnetic cross-coupling and thus $\xi = \zeta = 0$, which means that such a chiral system cannot be described by means of Tellegen's/Pasteur's or Posts' model. However, it cannot be assumed that such a system would not exhibit chiral effects and thus the only remaining model is the DBF, which has been shown to predict said chiral effects. Here, β is associated with the structural chirality, or the chirality parameter and as such is sometimes replaced by the chirality parameter κ used in the other models [31].

	Tellegen/Pasteur	Post	Drude-Born-Fedorov
$\vec{D} =$	$\epsilon\vec{E} + (\chi + i\kappa\sqrt{\epsilon_0\mu_0})\vec{H}$	$\epsilon\vec{E} + i\xi\vec{B}$	$\epsilon(\vec{E} + \beta\vec{\nabla} \times \vec{E})$
$\vec{B} =$	$(\chi - i\kappa\sqrt{\epsilon_0\mu_0})\vec{E} + \mu\vec{H}$	$\mu(\vec{H} - i\xi\vec{E})$	$\mu(\vec{H} + \beta\vec{\nabla} \times \vec{H})$

Table 2.1: Three common models to study chiral media. If $\chi \neq 0$ and $\kappa = 0$ the distinction of the Tellegen medium is used, and if $\chi = 0$ and $\kappa \neq 0$ the Pasteur medium applies, which is what historically has been referred to as a chiral medium. Table adapted from [31] and adjusted with [27] for a more general expression for the Tellegen/Pasteur model.

For the scope of this thesis, the derivation will be limited to the case of the Pasteur medium, which classically is referred to when speaking about chiral media. In this case, $\chi = 0$ (i.e. medium is reciprocal) and thus the following constitutive relations are true:

$$\vec{D} = \epsilon\vec{E} + \mathrm{i}\gamma\vec{H}, \tag{2.6a}$$

$$\vec{H} = \frac{1}{\mu}(\vec{B} + \mathrm{i}\gamma\vec{E}), \tag{2.6b}$$

where $\gamma = \kappa\sqrt{\epsilon_0\mu_0}$. After equation (2.3c) is rearranged and substituted into equation (2.6b), this leads to:

$$\vec{H} = \frac{1}{\mu}(\mathrm{i}\gamma\vec{E} - \frac{1}{\mathrm{i}\omega}(\vec{\nabla} \times \vec{E})). \tag{2.7}$$

Rearranging (2.3d) and following Pasteur's constitutive relation for $\vec{D}$ in (2.6a), to get the expression:

$$\frac{1}{\mathrm{i}\omega}(\vec{\nabla} \times \vec{H}) = \epsilon\vec{E} + \mathrm{i}\gamma\vec{H}. \tag{2.8}$$

Subsequently, using (2.7) and substituting into (2.8):

$$\frac{1}{\mathrm{i}\omega\mu}\vec{\nabla} \times \left(\mathrm{i}\gamma\vec{E} - \frac{1}{\mathrm{i}\omega}(\vec{\nabla} \times \vec{E})\right) = \epsilon\vec{E} + \frac{\mathrm{i}\gamma}{\mu}\left(\mathrm{i}\gamma\vec{E} - \frac{1}{\mathrm{i}\omega}(\vec{\nabla} \times \vec{E})\right). \tag{2.9}$$

This expression can be rearranged:

$$\vec{\nabla} \times (\vec{\nabla} \times \vec{E}) + \omega\gamma(\vec{\nabla} \times \vec{E}) - \omega^2\epsilon\mu\vec{E} + \omega^2\gamma^2\vec{E} + \omega\gamma(\vec{\nabla} \times \vec{E}) = 0, \tag{2.10}$$

and after collecting equal terms, this leads to:

$$\vec{\nabla} \times (\vec{\nabla} \times \vec{E}) - (\epsilon\mu - \gamma^2)\omega^2\vec{E} + 2\omega\gamma(\vec{\nabla} \times \vec{E}) = 0. \tag{2.11}$$

Now, the vector identity $\vec{\nabla} \times (\vec{\nabla} \times \vec{A}) = \vec{\nabla}(\vec{\nabla} \cdot \vec{A}) - \vec{\nabla}^2 \vec{A}$ can be exploited to get the differential equation:

$$\nabla^2 \vec{E} + (\epsilon\mu - \gamma^2)\omega^2 \vec{E} - 2\omega\gamma(\vec{\nabla} \times \vec{E}) = 0. \tag{2.12}$$

So, if it is assumed that a plane wave propagating in the z-direction is of the form:

$$\vec{E} = \begin{bmatrix} E_x \\ E_y \\ 0 \end{bmatrix} e^{\mathrm{i}kz}, \tag{2.13}$$

substituting this expression for $\vec{E}$ in (2.12):

$$\nabla^2 \begin{bmatrix} E_x \\ E_y \\ 0 \end{bmatrix} e^{\mathrm{i}kz} + (\epsilon\mu - \gamma^2)\omega^2 \begin{bmatrix} E_x \\ E_y \\ 0 \end{bmatrix} e^{\mathrm{i}kz} - 2\omega\gamma\vec{\nabla} \times \begin{bmatrix} E_x \\ E_y \\ 0 \end{bmatrix} e^{\mathrm{i}kz} = 0. \tag{2.14}$$

The terms containing the $\vec{\nabla}$-operator can be solved, by using the straightforward solutions:

$$\nabla^2 \begin{bmatrix} E_x \\ E_y \\ 0 \end{bmatrix} e^{\mathrm{i}kz} = \begin{bmatrix} E_x \\ E_y \\ 0 \end{bmatrix} - k^2 e^{\mathrm{i}kz}, \qquad \vec{\nabla} \times \begin{bmatrix} E_x \\ E_y \\ 0 \end{bmatrix} e^{\mathrm{i}kz} = \begin{bmatrix} -E_y \\ E_x \\ 0 \end{bmatrix} \mathrm{i}k e^{\mathrm{i}kz}. \tag{2.15}$$

Thus, our expression in (2.14) becomes:

$$-k^2 \begin{bmatrix} E_x \\ E_y \end{bmatrix} e^{\mathrm{i}kz} + (\epsilon\mu - \gamma^2)\omega^2 \begin{bmatrix} E_x \\ E_y \end{bmatrix} e^{\mathrm{i}kz} - 2\mathrm{i}\omega\gamma k \begin{bmatrix} -E_y \\ E_x \end{bmatrix} e^{\mathrm{i}kz} = 0. \tag{2.16}$$

The final differential expression can be written in the eigenproblem form $M\vec{E} = 0$:

$$\begin{bmatrix} (\epsilon\mu - \gamma^2)\omega^2 - k^2 & -2\mathrm{i}\omega\gamma k \\ 2\mathrm{i}\omega\gamma k & (\epsilon\mu - \gamma^2)\omega^2 - k^2 \end{bmatrix} \begin{bmatrix} E_x \\ E_y \end{bmatrix} = 0. \tag{2.17}$$

This eigenvalue problem can be solved in the usual manner, by calculating its determinant, such that:

$$\det M = \begin{vmatrix} (\epsilon\mu - \gamma^2)\omega^2 - k^2 & -2\mathrm{i}\omega\gamma k \\ 2\mathrm{i}\omega\gamma k & (\epsilon\mu - \gamma^2)\omega^2 - k^2 \end{vmatrix} = 0, \tag{2.18}$$

to give:

$$\det M = \omega^4(\epsilon\mu - \gamma^2)^2 - 2k^2\omega^2(\epsilon\mu + \gamma^2) + k^4 = 0, \tag{2.19}$$

the solution to this expression results in the dispersion relation of light propagating through our medium with:

$$k_\pm = \omega(\sqrt{\epsilon\mu} \pm \gamma), \tag{2.20}$$

and since the wave number k is of the form $k_\pm = k_0 n$, and $k_0 = \dfrac{\omega}{c_0} = \omega\sqrt{\epsilon_0\mu}$; taking into account that $\gamma = \kappa\sqrt{\epsilon_0\mu_0}$, the expression for the refractive index of our chiral medium can be found to be:

$$n_\pm = \sqrt{\epsilon_r\mu_r} \pm \kappa. \tag{2.21}$$

This derivation shows that the refractive index of the chosen medium depends largely on its structural chirality κ, which can give rise to interesting phenomena, such as a negative refractive index [32–34]. The eigenwaves associated with our solution are:

$$\vec{E}_\pm = \begin{bmatrix} E_x \\ \pm \mathrm{i}E_y \end{bmatrix} e^{\mathrm{i}kz}, \tag{2.22}$$

with $\pm$ denoting LCP and RCP respectively. The result represents the mathematical foundation to describe the propagation of light in chiral media. In the following section, the physical phenomena that arise based on our analysis are introduced and discussed. Generally, all optical effects arising from the interaction of light with chiral media are collectively described as chiral optical (chiroptical) effects and can be exploited to study the symmetry of samples via their interaction with light.

2.1.5 Optical activity

Optical activity (OA) is associated with all phenomena accompanying the difference in the interaction of a chiral medium with LCP and RCP light [8]. It was previously established that such chiroptical effects arise from media with a nonzero chirality parameter κ. Molecular chirality is a fundamental property of molecules that is intrinsically linked to their geometry. As chirality is due to the geometry of the sample, symmetry arguments can be applied to differentiate chirality [3,35]. Optical activity is further differentiated into its two "classical" types – electronic OA (EOA) and vibrational OA (VOA) [8]. EOA is associated with electronic transitions in the visible and ultraviolet (UV) spectrum [35–37], while VOA refers to vibrational

transitions, that occur in the infrared spectral region [38, 39]. For the scope of this thesis, the following discussion will be limited to EOA.

2.1.5.1 Optical rotation

Optical rotation (OR) refers to a rotation of the plane of polarised light due to an interaction with a chiral medium [40–42]. It is a phenomenon similar to linear birefringence. For linear birefringence, a difference in the phase velocity of light can be observed along two crystallographic directions of propagation for linearly polarised light. In the case of OR, a difference in the phase velocity of light can be observed for LCP and RCP light, hence the effect is also sometimes referred to as circular birefringence [40, 42, 43].

On the microscopic level, infinitesimal rotations of the plane of polarised light can be observed for both chiral and achiral materials, however, in the achiral case the statistical net effect is zero. The reason for this is based on the symmetry of achiral media, as every infinitesimal rotation has an associated counter-rotation. In a chiral medium, the symmetry is broken and therefore these small rotations accumulate and result in a measurable rotation of the plane of polarised light.

To illustrate this point, it can be assumed that the incident electromagnetic wave is linearly polarised and is transmitted by an optically active medium. In this case, linearly polarised light can be represented as a combination of two circularly polarised waves. Furthermore, the assumption is made that the optically active medium has a refractive index that is different for RCP and LCP light, but the extinction coefficient is the same for both. Thus, the complex index of refraction $\tilde{n}$ can be rewritten such that:

$$\tilde{n} = n + \mathrm{i}\kappa_{\mathrm{ext}}, \tag{2.23}$$

where the real part $n = c/v_p$, with c as the speed of light and v_p as the phase velocity and κ_{ext} as the extinction coefficient (not to be confused with the chirality parameter). A difference in the refractive index for LCP and RCP light can only be due to a change in the phase velocity. While the phase for LCP and RCP light is different, the amplitude remains the same. The resulting wave is schematically shown in Figure 2.3. Propagating through the optically active medium, LCP (σ^-) and RCP (σ^+) lightwaves have different angular velocities; here σ^- is slower than σ^+. The difference in angular velocity is called retardation and, upon exiting the material, the resulting wave is rotated by an angle ϕ with respect to the vertical direction. This angle measures the optical rotation in degrees or radians [44, 45].

Circularly polarised light can also be represented by a set of linear waves:

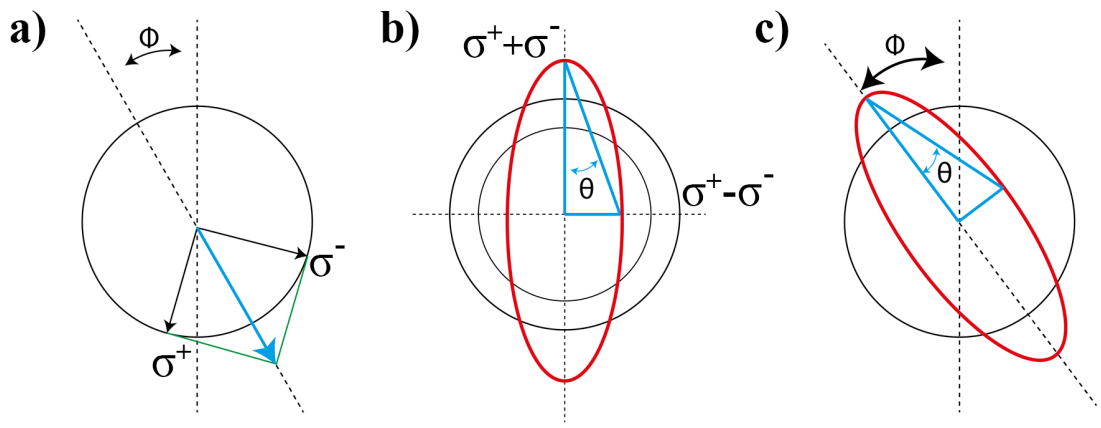

Figure 2.3: Schematics of (a) optical rotation with left (σ^-) and right (σ^+) circularly polarised light propagating with different phase velocities in the optically active medium. As a result, the plane of polarisation of the transmitted wave is rotated by an angle ϕ. In (b), the phenomenon of circular dichroism is shown. As the extinction coefficient for LCP (σ^-) and RCP (σ^+) light are different in a chiral medium, upon exiting the material, the electric field of the transmitted wave describes an ellipse (red), with an angle of ellipticity θ (blue). In the general case both optical rotation and circular dichroism happen simultaneously, which is shown in (c). Adapted from [1].

$$\begin{aligned} E_x^- &= A\cos\left(kz-\omega t\right) & E_x^+ &= A\cos\left(kz-\omega t\right), \\ E_y^- &= -A\sin\left(kz-\omega t\right) & E_y^+ &= A\sin\left(kz-\omega t\right), \end{aligned} \tag{2.24}$$

where E_x and E_y are the x- and y-components of the electromagnetic wave, in a three dimensional coordinate system in which the wave is propagating in the z-direction, for LCP (-) and RCP (+), A is a constant amplitude, k is the wave number, z the direction of propagation, ω the angular frequency and time t. The refractive index can be expressed as the average of the refractive index for RCP (+) and LCP (-) light, such that:

$$n = \frac{c}{v_p} = \frac{ck}{\omega} = \frac{n^+ + n^-}{2}. \tag{2.25}$$

Rearranging (2.24) and applying (2.25), then combining x- and y-components results in the following expression for the optical rotation ϕ:

$$\tan\phi = \frac{E_y}{E_x} = \frac{2A\cos\left[\frac{\omega}{c}\left(nz-ct\right)\right]\sin\left[\frac{\omega}{2c}\left(n^+-n^-\right)z\right]}{2A\cos\left[\frac{\omega}{c}\left(nz-ct\right)\right]\cos\left[\frac{\omega}{2c}\left(n^+-n^-\right)z\right]} = \tan\left[\frac{\omega}{2c}\left(n^+-n^-\right)z\right], \tag{2.26}$$

with

$$\phi = \frac{\omega}{2c}\left(n^+-n^-\right)z = \frac{\pi}{\lambda}\left(n^+-n^-\right)l, \tag{2.27}$$

where ϕ is expressed in radians, λ is the wavelength of the light, and l is the path length travelled through the medium. The refractive index of a medium is generally wavelength-dependent, i.e. dispersive, and therefore the differential refractive index, i.e. $n^+ - n^-$ is also wavelength-dependent. The wavelength-dependent change in OR (i.e. the OR spectrum) is defined as optical rotatory dispersion (ORD) [8, 46].

2.1.5.2 Circular Dichroism

Whereas OR is sensitive to the geometric arrangement of the electromagnetic field on the molecular or nanostructure level induced by the interaction of the light with the atoms' valence electrons, CD is sensitive to electronic energy transitions and thus strongest at resonance, or excitation, frequencies. The two effects are complementary [8]. In the case of OR spectra, the refractive index affects the phase velocity of LCP (σ^-) and RCP (σ^+) light differently, while the extinction coefficient is the same for both. For the case of CD, the phase velocities of LCP and RCP light are the same, while the extinction coefficient is different, as shown in Figure 2.3b. The difference in the extinction coefficient leads to different amplitudes for LCP and RCP light. The result is that the electric field vector of light describes an ellipse in the plane perpendicular to the direction of propagation. The ellipticity θ representing the typical measure of CD is given in degrees. This is a result of unit conversion rather than direct measurement, as commercial CD spectrometers usually do not measure the ellipticity directly [8].

Mathematically, the ellipticity is given by the following relation:

$$\tan(\theta) = \frac{|\sigma^+| - |\sigma^-|}{|\sigma^+| + |\sigma^-|}. \tag{2.28}$$

Most CD experiments measure differences in intensities, so equation (2.28) must be rearranged to be in terms of LCP (-) and RCP (+) light intensities (I^- and I^+, respectively), which can be expressed as:

$$\tan(\theta) = \frac{\sqrt{I^+} - \sqrt{I^-}}{\sqrt{I^+} + \sqrt{I^-}}. \tag{2.29}$$

In the small angle approximation, this reduces to:

$$\theta = \frac{\sqrt{I^+} - \sqrt{I^-}}{\sqrt{I^+} + \sqrt{I^-}}. \tag{2.30}$$

OR and CD are both expressions of the optical activity of a material and both are routinely used in characterising chiral materials [3].

In the general case, both the extinction coefficient and refractive index would be different for LCP and RCP light, which leads to the simultaneous occurrence of OR and CD. The resulting wave is schematically shown in Figure 2.3c. In the

early 1960s, Moscowitz found that OR and CD are strongly correlated. This was later formalised in the Kramers-Kronig relation, as shown in equation (2.31), owing to the fact that OR and CD relate to the real and imaginary parts of the complex refractive index, respectively [8]:

$$\begin{aligned} [\phi(\omega)] &= \tfrac{2}{\pi} PV \int_0^\infty \frac{\omega' \left[\theta\left(\omega'\right)\right]}{\omega'^2 - \omega^2} d\omega', \\ [\theta(\omega)] &= -\tfrac{2\omega}{\pi} PV \int_0^\infty \frac{\left[\phi\left(\omega'\right)\right]}{\omega'^2 - \omega^2} d\omega \end{aligned}, \tag{2.31}$$

where ω' is the excitation frequency and PV denotes the Cauchy principal value of the integral [46]. Using this set of equations, it is possible to obtain the ORD from measuring the spectrum of CD and vice versa.

2.1.5.3 Bisignate nature of optical activity

Chiroptical effects change sign over the wavelength spectrum of incident light, often several times, frequently resulting in bisignate ('of two sign') regions, where a negative peak is observed close to a positive peak [47]. For instance, close to the resonance, or excitation, frequency where CD is usually strongest, it is observed that the optical rotation changes sign. This particular sign change is known as the Cotton effect [48, 49]. It originates from the Kramers-Kronig relationship between CD and OR. For an intuitively appealing image, one can consider a driven mechanical oscillator near resonance. At the lower energy side of the resonance, the oscillations are in phase with the driving force. At the higher energy side of the resonance, the oscillations are out of phase with the driving force. It can be seen that, at resonance, the amplitude of the oscillations is large and the phase undergoes a sharp 180° transition. CD and OR can be seen as analogous to the amplitude and phase of the oscillator because CD is related to the extinction coefficient and OR is related to the phase velocity for circularly polarised light. It is therefore not surprising that when the CD is maximum, the OR undergoes a sharp variation.

The bisignate nature of optical activity was highlighted in 1930, when Kuhn stated a sum rule that requires the value of optical activity to be zero when integrated over the full spectrum of available resonances [50]. Kuhn considered a mechanical model for molecular bonds, where two linear oscillators are positioned perpendicularly and on top of each other. When the resonators are coupled, each one experiences a small force from the other. As a consequence, the resonances of both oscillators shift, due to the coupling term. For two oscillators of different frequency, the sign of the optical activity in the first oscillator depends on whether the resonant frequency of the second oscillator is higher or lower. Naturally though,

from the point of view of the second oscillator coupling to the first one, the situation is opposite. It follows that at the two resonance frequencies, the optical activities always have opposite signs. This principle can be extended to any number of coupled oscillators.

2.2 Plasmonics

2.2.1 Light interaction with metals

In the previous chapter, Maxwell's equations were used to describe the behaviour of light interacting with chiral media. In this section, Maxwell's equations will be used to study the interaction of electromagnetic waves and metals.

The specific interest in metals when studying light-matter interactions is based on the unique phenomenon associated with metal bonding. Metal-metal bonding creates a giant lattice of positively charged metal cores, while the electrons from the conductive band are delocalised from individual atoms. These delocalised electrons are free to move inside the metal lattice and are collectively referred to as the free electron sea. When illuminated with light, it is the free electron sea that governs the interaction with the lightwave. The lightwave causes the free electron sea to oscillate with an angular frequency $\omega = 2\pi f$, where f is the frequency of illumination. Interestingly, it can be found that the properties of metals under illumination can change dramatically around a material-specific *characteristic frequency* of oscillation, f_c which is usually of the order of 10^{15} Hz. For frequencies $< f_c$, typically in the visible and near-infrared (NIR) part of the electromagnetic spectrum, the metals yield high conductivity and permittivity causing the metal to be highly reflective. The reflective behaviour of metals in this low frequency regime is what is commonly referred to as *metallic* [51]. For frequencies $> f_c$, usually in the ultraviolet (UV) part of the electromagnetic spectrum, the properties of metals change dramatically and the metal acquires a more dielectric character – they become poor conductors and highly absorptive [3].

The drastic change in metal properties under light illumination is based on the complex dielectric functions conductivity σ and permittivity ϵ which are intrinsically linked quantities [25], formalised in the Fourier domain as:

$$\epsilon(\vec{K}, \omega) = 1 + \frac{\mathrm{i}\sigma(\vec{K}, \omega)}{\epsilon_0 \omega}, \tag{2.32}$$

with ω as the angular frequency, $\vec{K}$ as the wavevector inside the medium and ϵ_0 as the permittivity of free space and is known as the *Drude model* of the optical response of metals [51]. In general, permittivity and conductivity are represented

as complex functions, such that:

$$\epsilon(\omega) = \epsilon_1(\omega) + \mathrm{i}\epsilon_2(\omega), \tag{2.33a}$$

$$\sigma(\omega) = \sigma_1(\omega) + \mathrm{i}\sigma_2(\omega), \tag{2.33b}$$

Experimentally, these complex dielectric functions can be determined by measuring the complex refractive index, as presented in equation (2.23), since:

$$\tilde{n} = \sqrt{\epsilon}. \tag{2.34}$$

Manipulating Maxwell's equations, it can be shown that the combination of the curl of Maxwell's third (2.3c) and fourth (2.3d) equations lead to the wave equation describing the propagation of light in a medium without free currents:

$$\vec{\nabla} \times \vec{\nabla} \times \vec{E} = -\mu_0 \frac{\partial^2 \vec{D}}{\partial t^2}, \tag{2.35}$$

with μ_0, representing the permeability of free space and $\vec{E}$ and $\vec{D}$ as the vectors for the electric field and electric displacement respectively. The electric displacement is defined as $\vec{D} = \epsilon_0 \vec{E} + \vec{P}$, with $\vec{P}$ as the macroscopic polarisation. Typically (2.35) is expressed in the Fourier domain as [51]:

$$\vec{K}(\vec{K} \cdot \vec{E}) - K^2 \vec{E} = -\epsilon(\vec{K}, \omega) \frac{\omega^2}{c^2} \vec{E}, \tag{2.36}$$

with $c = \frac{1}{\sqrt{\epsilon_0 \mu_0}}$ as the speed of light in vacuum.

Expression (2.36) yields two solutions, which depend on the polarisation of the electric field vector $\vec{E}$. First, there is the transverse case, for which:

$$\vec{K} \cdot \vec{E} = 0, \tag{2.37}$$

this leads to the general expression for the dispersion relation:

$$K^2 = \epsilon(\vec{K}, \omega) \frac{\omega^2}{c^2}. \tag{2.38}$$

Second, there is the longitudinal case:

$$\epsilon(\vec{K}, \omega) = 0, \tag{2.39}$$

from which it can be seen that longitudinal waves can only be observed for frequencies at which the material-dependent dielectric constant $\epsilon(\omega) = 0$.

2.2.2 Volume plasmons

A description of the free electron sea is required to fully understand what makes metals *metallic*. Typically, the free electron sea is approximately described with the *free electron model* [52]. In the free electron model, the electron oscillations are driven by an external electromagnetic field. The oscillation is dampened by electron-electron collisions with a characteristic rate $\gamma = \frac{1}{\tau}$, with τ representing the relaxation time of the free electron sea. The displacement $\vec{x}$ of the oscillating electrons contributes to the macroscopic polarisation $\vec{P} = -en_e\vec{x}$, with e being the electric charge and n_e as the number density of the free electrons. The macroscopic polarisation can also be expressed as [51]:

$$\vec{P} = -\frac{n_e e^2}{m_{\text{eff}}(\omega^2 + \mathrm{i}\gamma\omega)}\vec{E}, \tag{2.40}$$

with m_{eff} representing the effective mass of the electron. The expression of the macroscopic polarisation can be substituted into Maxwell's equations to give:

$$\vec{D} = \epsilon_0 \left(1 - \frac{\omega_p^2}{\omega^2 + \mathrm{i}\gamma\omega}\right)\vec{E}, \tag{2.41}$$

where the term ω_p has been introduced to represent the characteristic frequency of the plasma oscillation, such that $\omega_{\text{p}} = 2\pi f_{\text{c}}$ and is defined such that $\omega_p^2 = \frac{ne^2}{\epsilon_0 m_{\text{eff}}}$. So, an explicit expression for the complex permittivity of the free electron sea can be presented as:

$$\epsilon(\omega) = 1 - \frac{\omega_p^2}{\omega^2 + \mathrm{i}\gamma\omega}, \tag{2.42}$$

and from equation (2.33a), both terms of the complex permittivity can be re-written as:

$$\epsilon_1(\omega) = 1 - \frac{\omega_p^2\tau^2}{1 + \omega^2\tau^2}, \tag{2.43a}$$

$$\epsilon_2(\omega) = \frac{\omega_p^2\tau}{\omega(1 + \omega^2\tau^2)}. \tag{2.43b}$$

Here, ϵ_1 is associated with the refractive index and linked to the phase velocity inside the medium and ϵ_2 is associated with the extinction coefficient (see equation (2.23)) – therefore representing the attenuation of the lightwave inside the medium. From equation (2.42) the reflecting behaviour of metals can be explained mathematically: for very low frequencies for which $\omega << \omega_p$ leads to $\omega\tau << 1$ and equation (2.42) becomes completely imaginary. For frequencies $\omega \approx \omega_p$, the term

$\omega\tau >> 1$, which is causing negligible damping of the lightwave and a rapid fall of the metal's reflectivity and its transition into transparency. The dielectric function of the electron sea in this regime can be simplified to:

$$\epsilon(\omega) = 1 - \frac{\omega_p^2}{\omega^2}. \tag{2.44}$$

This expression allows the prediction of certain characteristics. At low frequencies for which $\omega << \tau^{-1}$, and since $\epsilon(\omega) = \epsilon_1(\omega) + \mathrm{i}\epsilon_2(\omega)$ it can be found that $\epsilon_2 >> \epsilon_1$, leading to a mainly absorptive character, which is formalised in the absorption coefficient [51]:

$$\alpha = \left(\frac{2\omega_p^2\tau\omega}{c^2}\right)^{\frac{1}{2}}. \tag{2.45}$$

The material's skin depth (depth into which the light can penetrate into the medium) can be determined with Beer's Law, which implies that for low frequencies, the amplitude reduces with $e^{-\frac{z}{\delta}}$, with δ representing the skin depth [51]:

$$\delta = \sqrt{\frac{2}{\sigma_0\omega\mu_0}}, \tag{2.46}$$

where σ_0 represents the DC-conductivity, defined as $\sigma_0 = ne^2\tau/m_{\text{eff}} = w_p^2\tau\epsilon_0$. It is important to note, that this description is only valid for non-noble metals, since noble metals yield electronic interband transitions in the visible spectrum of light; and as long as the mean free path of the electrons $l = v_F\tau << \delta$, where v_F is the Fermi velocity – typically, it can be found that $l \approx 10$ nm and $\delta \approx 100$ nm [53]. Here, the Fermi velocity is associated with the kinetic energy of the electrons of the highest occupied state.

Thus, to conclude this analysis, in the transparency regime $\omega >> \omega_p$, the dispersion relation of the travelling wave is [51]:

$$\omega^2 = \omega_p^2 + K^2c^2. \tag{2.47}$$

In this regime, the wave propagates with a group velocity $v_g = \frac{\partial\omega}{\partial K} < c$ and at the plasma frequency ω_p, the damping of the plasma oscillations is minimised. Consequently, this will cause a collective displacement of the free electron sea, which will contribute to the macroscopic polarisation and thus induce an electric field inside the metal. The discretised energy, or *quantum*, associated with these oscillations is what is typically referred to as a *plasmon* [54]. This type of plasmon, also called *volume or bulk plasmon*, only takes the form of longitudinal waves, which cannot couple to transverse electromagnetic waves and decays via Landau Damping [51]. Also, since there is no coupling to the electromagnetic waves, bulk plasmons can only be excited by charged particle collisions.

2.2.3 Surface plasmons

2.2.3.1 Propagating surface plasmons

The surface plasmon polariton (SPP), in contrast to the bulk plasmon, is an electromagnetically excited plasmon that propagates along the interface of a dielectric and a conducting material. In this case, the oscillations of the electron plasma in the metal couple to the external electromagnetic wave and are highly dependent on the difference in the index of refraction of the two media.

If the wave equation (2.35) is again taken as a starting point and if the assumption holds that the permittivity $\epsilon = \epsilon(r)$ is constant over the distance of one optical wavelength along the interface, this leads to:

$$\nabla^2 \vec{E} - \frac{\epsilon}{c^2} \frac{\partial^2 \vec{E}}{\partial t^2} = 0. \tag{2.48}$$

This differential equation can be solved in both media, by assuming a constant ϵ and by applying suitable boundary conditions which depend on the geometry of the system. Furthermore, if it is assumed that the system yields a harmonic time dependence, such that $\vec{E}(\vec{r}, t) = \vec{E}(\vec{r})e^{-\mathrm{i}\omega t}$, the expression becomes the well-known *Helmholtz equation* [55]:

$$\nabla^2 \vec{E} + k_0^2 \epsilon \vec{E} = 0, \tag{2.49}$$

where $k_0 = \frac{\omega}{c}$ is the wavenumber.

If the system is further simplified by studying the case of a wave propagating in the x-direction along the metal-dielectric interface (see Figure 2.4a), in a material for which the permittivity does not change in the y-direction, the permittivity becomes $\epsilon = \epsilon(z)$. If a Cartesian coordinate system is situated such that the z-axis is normal to the interface and $z = 0$ coincides with the dielectric-metal interface, the problem can be simplified mathematically. The propagation of this wave is then described by $\vec{E}(x, y, z) = \vec{E}(z)e^{i\beta x}$, with $\beta = k_x$ representing the complex propagation constant.

If the Helmholtz equation (2.49) is combined with this equation of the propagating wave, the resulting expression describes the propagation of a wave confined to the surface of the conducting material. The electric component of this wave takes the form:

$$\frac{\partial^2 \vec{E}(z)}{\partial z^2} + \left(k_0^2 \epsilon - \beta^2\right) \vec{E} = 0. \tag{2.50}$$

While equation (2.50) describes how the electric field changes as the wave propagates, explicit solutions for E and H can only be found by solving a set of coupled equations arising from Maxwell's third and fourth equations. Due to the direction of propagation $\frac{\partial}{\partial x} = \mathrm{i}\beta$; and for the y-direction, $\frac{\partial}{\partial y} = 0$, the following set of coupled

equations can be found [51]:

$$\frac{\partial E_y}{\partial z} = -\mathrm{i}\omega\mu_0 H_x, \tag{2.51a}$$

$$\frac{\partial E_x}{\partial z} - \mathrm{i}\beta E_z = \mathrm{i}\omega\mu_0 H_y, \tag{2.51b}$$

$$\mathrm{i}\beta E_y = \mathrm{i}\omega\mu_0 H_z, \tag{2.51c}$$

$$\frac{\partial H_y}{\partial z} = \mathrm{i}\omega\epsilon_0\epsilon E_x, \tag{2.51d}$$

$$\frac{\partial H_x}{\partial z} - \mathrm{i}\beta H_z = -\mathrm{i}\omega\epsilon_0\epsilon E_y, \tag{2.51e}$$

$$\mathrm{i}\beta H_y = -\mathrm{i}\omega\epsilon_0\epsilon E_z. \tag{2.51f}$$

These equations split into two sets of solutions that depend on the polarisation of the incident electromagnetic wave. If the magnetic wave component is perpendicular to the plane of incidence it is known as the transverse magnetic (TM) mode, or P-polarised (E-component is parallel). In contrast, if the electric component is perpendicular to the plane of incidence it is referred to as transverse electric (TE) mode, or S-polarised (E-component is 'senkrecht'– from the German word for perpendicular).

For TM modes, only E_x, E_z and H_y are non-zero. Similarly, for TE modes this is the case for H_x, H_y and E_y components, which leaves a simplified and reduced set of equations to describe SPPs. For TM modes, the resulting equations are:

$$E_x = -\mathrm{i}\frac{1}{\omega\epsilon_0\epsilon}\frac{\partial H_y}{\partial z}, \tag{2.52a}$$

$$E_z = -\frac{\beta}{\omega\epsilon_0\epsilon}H_y, \tag{2.52b}$$

and the TM wave equation:

$$\frac{\partial^2 H_y}{\partial z^2} + \left(k_0^2\epsilon - \beta^2\right) H_y = 0. \tag{2.53}$$

For the TE modes, the set of equations therefore become:

$$H_x = \mathrm{i}\frac{1}{\omega\mu_0}\frac{\partial E_y}{\partial z}, \tag{2.54a}$$

$$H_z = \frac{\beta}{\omega\mu_0}E_y, \tag{2.54b}$$

and the TE wave equation:

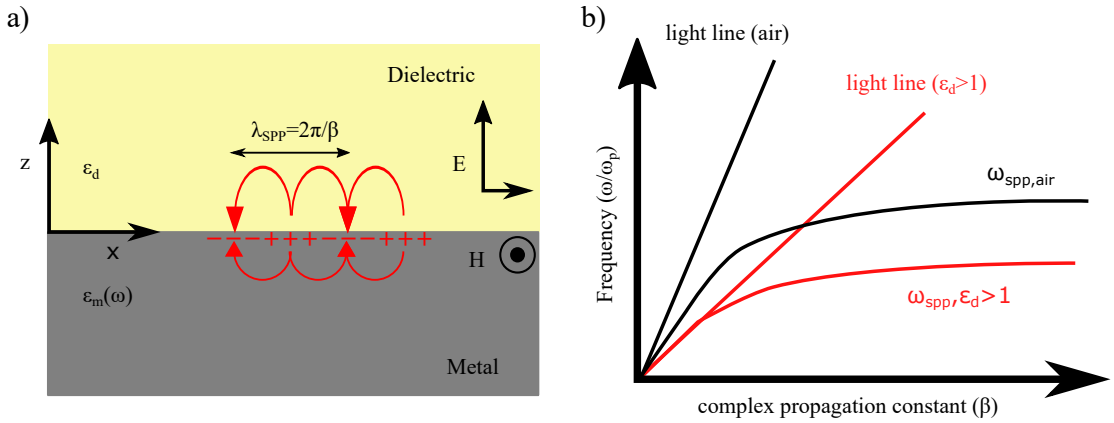

Figure 2.4: a) Schematic showing a surface plasmon polariton (SPP) at a dielectric-metal interface. b) Dispersion relation of Drude metal with negligible damping with air (black) and a dielectric with a permittivity $\epsilon_d > 1$ (red). Since there is no intersection of surface plasmon and light lines $\omega = c/k$, phase-matching is required to excite SPPs. One example is momentum-matching of light travelling through silica to allow the generation of a SPP at the air-metal interface (see intersection of black and red lines)

$$\frac{\partial^2 E_y}{\partial z^2} + \left(k_0^2 \epsilon - \beta^2\right) E_y = 0. \tag{2.55}$$

In the most basic example of SPPs, the interface would be between a dielectric and a flat metal surface. Here, as before, the system is separated into two parts – the lower part $z < 0$, occupied by a metal with $\Re\left(\epsilon_m(\omega)\right) < 0$, and the upper part $z > 0$, occupied by a dielectric with $\epsilon_d > 0$. This system is schematically shown in Figure 2.4a. The spatial confinement of the wave at such an interface (travelling in the $+x$-direction), also called the evanescent field, can be studied by solving the previously presented equations (2.52)-(2.55) in both the lower and upper part, respectively. For each part of the system, a medium-specific field amplitude A_1 and A_2, as well as associated wave numbers perpendicular to the interface k_1 and k_2 are introduced to define the fields on each side of the interface.

The TM mode solutions in the dielectric $z > 0$ become:

$$H_y(z) = A_2 e^{\mathrm{i}\beta x} e^{-k_2 z}, \tag{2.56a}$$

$$E_x(z) = \mathrm{i} A_2 \frac{1}{\omega \epsilon_0 \epsilon_2} k_2 e^{\mathrm{i}\beta x} e^{-k_2 z}, \tag{2.56b}$$

$$E_z(z) = -A_1 \frac{\beta}{\omega \epsilon_0 \epsilon_2} e^{\mathrm{i}\beta x} e^{-k_2 z}, \tag{2.56c}$$

and for $z < 0$:

$$H_y(z) = A_1 e^{\mathrm{i}\beta x} e^{k_1 z}, \tag{2.57a}$$

$$E_x(z) = -A_1 \frac{1}{\omega \epsilon_0 \epsilon_1} k_1 e^{\mathrm{i}\beta x} e^{k_1 z}, \tag{2.57b}$$

$$E_z(z) = -A_1 \frac{\beta}{\omega \epsilon_0 \epsilon_1} e^{\mathrm{i}\beta x} e^{k_1 z}, \tag{2.57c}$$

Now, by using the continuity principle [56]:

$$D_{1,z} = D_{2,z}, \qquad B_{1,z} = B_{2,z}, \tag{2.58a}$$

$$E_{1,x/z} = E_{2,x/z}, \qquad H_{1,x/y} = H_{2,x/y}, \tag{2.58b}$$

where the indices 1 and 2 denote the dielectric and the metal respectively, at the interface and by applying the wave equation for TM modes from (2.53), the resulting expression can be shown to be:

$$\beta = k_0 \sqrt{\frac{\epsilon_1 \epsilon_2}{\epsilon_1 + \epsilon_2}}. \tag{2.59}$$

Here, β provides the dispersion relation of the propagating SPPs along the interface.

A similar analysis can be carried out for the TE mode solutions, starting again in the upper part $z > 0$:

$$E_y(z) = A_2 e^{\mathrm{i}\beta x} e^{-k_2 z}, \tag{2.60a}$$

$$H_x(z) = -\mathrm{i} A_2 \frac{1}{\omega \mu_0} k_2 e^{\mathrm{i}\beta x} e^{-k_2 z}, \tag{2.60b}$$

$$H_z(z) = A_2 \frac{\beta}{\omega \mu_0} e^{\mathrm{i}\beta x} e^{-k_2 z}, \tag{2.60c}$$

and the lower part $z < 0$:

$$E_y(z) = A_1 e^{\mathrm{i}\beta x} e^{k_1 z}, \tag{2.61a}$$

$$H_x(z) = \mathrm{i} A_1 \frac{1}{\omega \mu_0} k_1 e^{\mathrm{i}\beta x} e^{k_1 z}, \tag{2.61b}$$

$$H_z(z) = A_1 \frac{\beta}{\omega \mu_0} e^{\mathrm{i}\beta x} e^{k_1 z}, \tag{2.61c}$$

Interestingly, if the continuity principle (boundary conditions at the interface)

is applied to these equations, it is found that no waves are confined to the interface for TE solutions. Therefore, TM modes are the only way to excite SPPs. Studying the dispersion of SPPs further as demonstrated in Figure 2.4b, it can be seen that lightwaves incident on a medium from air cannot excite SPPs directly (no intercept with ω_{sp} curves). Instead, the *phase-matching* of the electromagnetic wave to the SPPs is required – examples of such are momentum, grating or prism coupling. An example of momentum-matching is shown in Figure 2.4b. When a lightwave is guided through silica glass (prism) and is subsequently incident on an air-metal interface (see the intersection of black and red curves), the wave's phase is now sufficient to generate SPPs. A detailed description of grating and prism coupling can be found in reference [25].

It can be shown, that a certain characteristic frequency exists at which the damping of the electron oscillations is negligible. Without damping, the wavevector β goes to infinity and the group velocity approaches zero. This frequency is called the *surface plasmon frequency* and is defined as:

$$\omega_{sp} = \frac{\omega_p}{\sqrt{1+\epsilon_2}}. \tag{2.62}$$

The SPPs experiences energy dissipation due to absorption while propagating along the surface. The energy dissipation is measured with respect to the loss in intensity (square of the electric field). The factor by which the intensity has decreased at a point, x is given by $e^{-2\Im[\beta]x}$. The propagation length is defined as the distance by which the intensity has decayed by a factor of $\frac{1}{e}$ and is defined as [51]:

$$L = \left(2\Im\left[\beta\right]\right)^{-1}, \tag{2.63}$$

where the complex character of β stems from the fact that there is some degree of damping of the electron oscillations by the aforementioned free electron collisions and the interband transitions.

2.2.3.2 Non-propagating surface plasmons

The non-propagating type of surface plasmons, also called *localised surface plasmons* (LSP), in contrast to SPPs is directly coupled to the external electromagnetic wave. This coupling is possible for nanoparticles with dimensions much smaller than the wavelength, i.e. $d << \lambda$ [26]. In this regime, the electromagnetic wave can be assumed to have constant phase over the volume of the nanoparticles. This approximation is known as the *quasi-static approximation*. The problem is represented by a scattering phenomenon from a curved surface, for example in a spherical nanoparticle. The oscillating electrons experience a restoring force arising from their displacement, which directly links the electron oscillation to the external field. No

additional phase-matching is required, as is the case for SPPs [51].

The advantage of the quasi-static approximation in explaining localised surface plasmons, can best be described for the simplified case of an isotropic and homogeneous sphere with radius a and complex dielectric function $\epsilon(\omega)$. This sphere is placed in a dielectric, non-absorbing environment with constant dielectric function ϵ_d and is subject to a static electric field of $\vec{E} = E_0\hat{\vec{z}}$, this is schematically presented in Figure 2.5a. By applying the *Laplace equation*, $\nabla^2\Phi = 0$, the electric potential Φ can be found. The electric potential can subsequently be used to calculate the electric field, since $\vec{E} = -\vec{\nabla}\Phi$. Furthermore, using Legendre Polynomials and appropriate boundary conditions it has been shown that the electric potential inside Φ_{in} and outside Φ_{out} the homogeneous sphere can be described by the following equations [51]:

$$\Phi_{\text{in}} = \frac{3\epsilon_m}{\epsilon + 2\epsilon_m} E_0 r\cos\theta, \tag{2.64a}$$

$$\Phi_{\text{out}} = -E_0 r\cos\theta + \frac{\epsilon - \epsilon_m}{\epsilon + 2\epsilon_m} E_0 a^3 \frac{\cos\theta}{r^2}. \tag{2.64b}$$

The second expression Φ_{out} can be interpreted as the superposition of the applied field and a dipole situated in the centre of the sphere. Therefore, a dipole moment $\vec{p}$ can be substituted into the expression to become:

$$\Phi_{\text{out}} = -E_0 r\cos\theta + \frac{\vec{p}\cdot\vec{r}}{4\pi\epsilon_0\epsilon_m r^3}, \tag{2.65}$$

with:

$$\vec{p} = 4\pi\epsilon_0\epsilon_m a^3 \frac{\epsilon - \epsilon_m}{\epsilon + 2\epsilon_m}\vec{E_0}. \tag{2.66}$$

This induced dipole moment is proportional to the magnitude of the applied electric field via the polarisability α_p, since $\vec{p} = \epsilon_0\epsilon_m\alpha_p\vec{E_0}$. An expression for the polarisability of the nanoparticle with sub-wavelength dimensions is therefore given by:

$$\alpha_p = 4\pi a^3 \frac{\epsilon - \epsilon_m}{\epsilon + 2\epsilon_m}. \tag{2.67}$$

It can readily be seen, that the polarisability is at maximum when the denominator is minimised. The denominator is minimised around the resonance frequency (negligible damping):

$$\Re\left[\epsilon(\omega)\right] = -2\epsilon_m, \tag{2.68}$$

which is the case if the sign of the real part of the permittivity ϵ changes across

the dielectric-metal interface. The expression above is called the *Fröhlich condition*. The Fröhlich condition is met in Drude metals at a frequency of $\omega_0 = \frac{\omega_p}{\sqrt{3}}$. This resonance frequency is strongly dependent on the environment – as the real part of the dielectric function ϵ_m increases, it causes the resonance to red-shift [57].

It can further be seen that the resonant enhancement of the electron oscillations affects both the absorption and the scattering. Since the extinction cross section is:

$$C_{\text{extinction}} = C_{\text{absorption}} + C_{\text{scattering}}, \tag{2.69}$$

it can be found that for nanoparticles smaller than 100 nm illuminated with visible or near-infrared light [1]:

$$C_{\text{extinction}} = 9\frac{\omega}{c}\epsilon_m^{\frac{3}{2}} V \frac{\epsilon_2}{\left(\epsilon_1 + 2\epsilon_m\right)^2 + \epsilon_2^2}, \tag{2.70}$$

where V is the volume of the nanoparticle. While being useful, this equation loses its validity for larger nanoparticles, i.e. $d \approx \lambda$, for which the phase of the external field is not constant over its volume. In order to account for this phase change, a rigorous theory of their scattering and absorption based on electrodynamics was proposed by Mie in 1908. This approach successfully describes the resonant behaviour of larger structures and is known as *Mie Theory* [58]. For sizes below 100 nm, Mie Theory simplifies to an expression equivalent to (2.70).

In the case of a single nanoparticle as shown in Figure 2.5b, it can be found that an increase in particle size causes a red-shift in the resonant frequency [26]. Physically, such an increase in size causes the distance between charges at the opposite interfaces to increase, causing a reduction in the restoring force. With increasing size another effect, negligible for smaller sizes, becomes dominant – *radiation damping*. Radiation damping is the direct conversion of electron oscillation into photons. This conversion will cause a broadening of the plasmon resonance as the plasma oscillations in large nanoparticles cause a dephasing between oscillation and incident field [59].

A red-shift of the plasmon resonance can also be observed for nanoparticles with a shape differing from the perfect sphere, such as nanorods or -wires. If the length of such a nanowire is sufficiently large, multiple resonances can be observed corresponding to higher-order oscillation modes along the length of the nanowire [60].

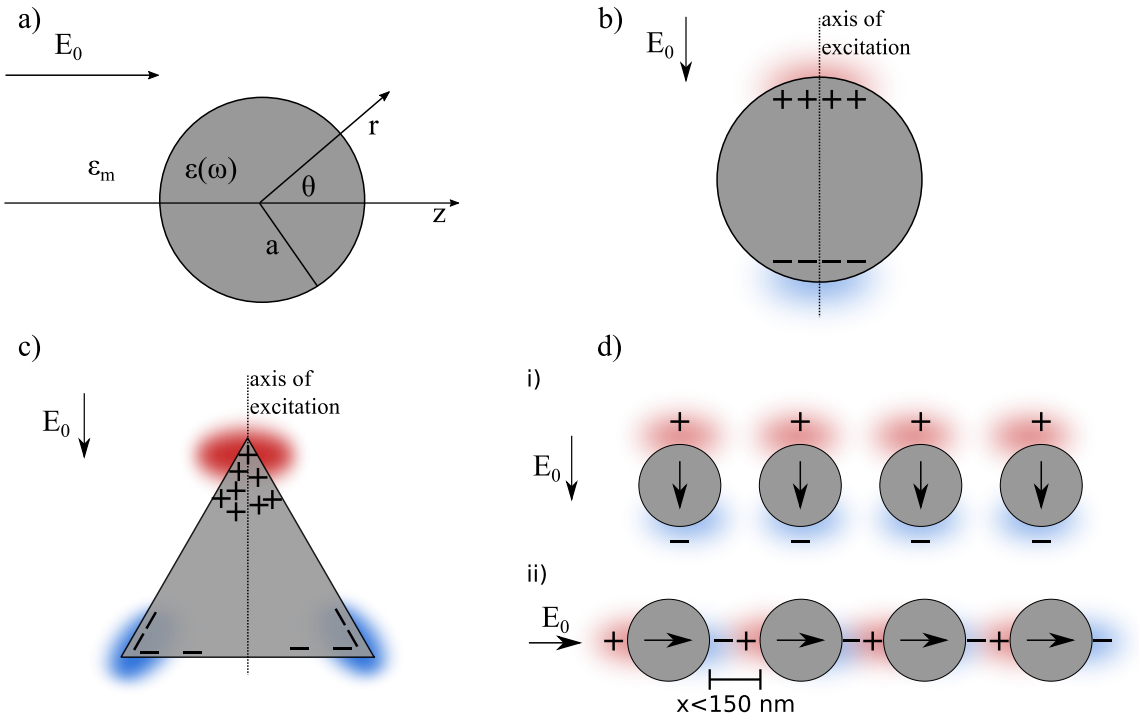

Figure 2.5: a) Nanosphere in an electrostatic field E_0 parallel to the z-axis. The nanosphere of radius a and complex dielectric function $\epsilon(\omega)$ is situated in an environment with a constant dielectric function ϵ_m. $\vec{r}$ and θ are used to describe the direction and angle of the electron oscillation relative to the z-axis. b) Electromagnetic field confinement of localised surface plasmon along the axis of excitation. c) Lightning-rod-effect schematically demonstrated as charge accumulation in sharp geometrical features. d) Chain of nanospheres with a separation below 150 nm for two types of excitation – i) transverse modes and ii) longitudinal modes.

Generally, the excitation of electron oscillations in metallic sub-wavelength nanoparticles creates a confinement of the electromagnetic field. This confinement depends strongly on the nanoparticle material, geometry and the surrounding refractive index [16,61]. In the beginning of this section, Laplace's equation was applied to determine the potential difference across the dielectric-metal-interface for a spherical nanoparticle. In that example, due to the curvature of the sphere's surface, the electrons were confined at the surface along the axis of incident polarisation – causing a strong potential difference at the interface. Introducing sharp geometrical features, such as tips and corners, can increase the potential difference as they lead to a confinement of the oscillating charges. This charge accumulation can therefore lead to extremely enhanced field confinement and is known as the *lightning-rod-effect* [16, 61, 62], and an example is shown in Figure 2.5c.

Another interesting phenomenon arises when two or more nanoparticles are in close proximity to each other. Typically close proximity refers to separations below 150 nm. For higher separations, the individual nanoparticles regain their isolated behaviour [59]. For separations below 150 nm, the concentrated surface plasmons

of the nanoparticles can couple to each other. Depending on the polarisation of the external field, with respect to the nanoparticle arrangement, *transverse* or *longitudinal* modes can be excited. This is schematically shown in Figure 2.5d. If the near-fields are coupled orthogonally to the chain orientation, a blue-shift of the plasmon resonance frequency compared to that of a single nanoparticle occurs [51], and is referred to as the excitation of transverse modes. Similarly, if the polarisation of the external field is parallel to the axis of nanoparticle alignment, a red-shift occurs and is known as longitudinal mode excitation.

2.3 Diffractive optics

2.3.1 Introduction into diffractive optics

The emergence of high-precision fabrication techniques has fueled new developments in the field of diffractive optics [63–65]. Since optical elements with sizes comparable to and even smaller than the wavelength of light can now be fabricated, this allows access to a useful set of diffractive optical elements that can be used to replace thick optical elements in use today.

In diffractive optics, instead of the word 'beam', the term 'wavefront' is commonly used to describe the lightwave resulting from the transmission or reflection by a diffractive element. A wavefront is defined as a continuous surface perpendicular to the direction of light rays in which the electric field has the same phase and in most cases the same amplitude as well [66].

In the context of wavefronts, it is beneficial to briefly introduce the *Huygens-Fresnel Principle*. The Huygens-Fresnel Principle states that a wavefront can be represented as a series of smaller point sources. The representation of the wavefront in this way addresses the issue of lightwaves propagating through a narrow slit. Applying the Huygens-Fresnel Principle, a wavefront in a narrow slit can be treated as a series of point sources [67]. A point source emits radiation in all directions and the radiation takes the form of spherical wavefronts centered about the point source. This principle is schematically shown in Figure 2.6. The original wavefront is evenly populated with a series of point sources Figure 2.6a. All the point sources emit spherical wavefronts, which are in phase with each other (Figure 2.6b). An envelope function can be found, which describes the spatial coordinates at some time t, for which the radiation from all point sources are in phase with each other. This envelope function mathematically represents the propagating wavefront, as shown in Figure 2.6c and 2.6d.

Interestingly, a consequence of the Huygens-Fresnel Principle is that the propagating wavefront extends beyond the width of the aperture – a direct result of the

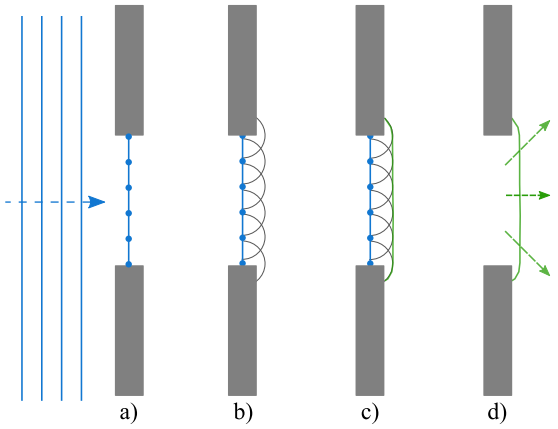

Figure 2.6: Huygens-Fresnel Principle applied to a narrow slit. a) A wavefront incident on an aperture can be represented by a series of point sources (blue dots). b) Each point source is generating a spherical wave (grey semi-circles) and all waves are in phase. c) The overlay of these waves forms the envelope function (green line) for the spreading wave from the aperture. d) The transmitted wave now spreads wider than the initial aperture as a result of the envelope function. Adapted from [66].

diffraction, i.e. the obstruction causes the light to spread into the geometric shade.

As early as 1801, Thomas Young demonstrated in his seminal double-slit experiments the wave-like nature of light and introduced the concept of light *interference* [68]. Interference refers to the phenomenon of combining two or more wavefronts depending on their phase. If the wavefronts are in phase with each other, the wavefronts are said to interfere *constructively* and similarly, if the wavefronts are out of phase *destructively*. For interference to occur, two conditions must be met – the wavefront sources need to be *coherent*, i.e. the waves are identical with a constant phase difference; and the waves need to be *monochromatic*, i.e. of a single wavelength. If two sources are imagined, which fulfill the requirement of coherence and are monochromatic, then the type of interference at a point P away from the sources is governed by the following expressions:

$$\delta = m\lambda \qquad \text{or} \qquad \delta = (m + \frac{1}{2})\lambda, \tag{2.71}$$

where δ is the difference in optical path length between the two sources and point P, m is an integer number and λ is the wavelength of the electromagnetic wave. If the difference in path length is an integer multiple of the wavelength constructive interference occurs, while any half-integer multiple results in destructive interference. Whereas interference refers to the behaviour of coinciding wavefronts, the concept of *diffraction* is used to describe the behaviour of a wavefront that propagates through a slit or obstacle with dimensions comparable to its wavelength. For the case of Young's double-slit experiment, resulting in two identical wavefronts formed at the

slits and subsequently interfering with each other. The result of this interference can be observed as multiple beams moving in different directions away from the slit. The importance of that integer multiple of the wavelength in this context gives rise to what is referred to as the *diffraction order*, which depending on whether the wavefronts are 'advanced' ($m = +1, +2, +3$, etc.) or 'retarded' ($m = -1, -2, -3$, etc.) can be positive or negative [68]. In diffractive optics, the aim is to optimise the surface profile of a diffractive element such that for a certain wavelength λ_1 the diffracted light is coupled into a specific diffraction order m_1. Additionally, it is possible to optimise the diffractive element for a second wavelength λ_2 to be coupled into a different diffraction order m_2. Furthermore, diffractive elements can generate more than one diffraction order. The most intense of these diffraction orders is called the *fundamental diffraction order*. Hence, the power distribution in the diffraction pattern can be exploited if the highest possible intensity is not the focus of the application [68].

For the scope of this thesis, the definitions of free-space digital optics proposed by Kress et al. [68], shall be briefly introduced. Depending on the structure and functionality, a differentiation of five different types of optics has been suggested: Holographic optical elements (HOEs), diffractive optical elements (DOEs), computer-generated holograms (CGHs), sub-wavelength digital elements (SWEs) and dynamic digital optics (DDOs). In this context, *digital* means that the surface profile of an element has been calculated by a computer and was fabricated by lithography as planar structures (see section 2.3.5). HOEs refer to the traditional optical holographic recording of volume-phase or surface-relief holograms, depending on the material used. DOEs, or *analytic* diffractives, are those elements that can be designed by analytic methods (ray tracing) or by solving analytical equations. In contrast, the design of CGHs, or *numeric* diffractives, requires iterative optimisation and algorithms. SWEs are elements with feature sizes smaller than that of the target wavelength. DDOs are defined as elements which incorporate technologies to allow them to change their optical properties and can be any of the four other types. For the scope of this thesis the focus will be on DOEs, CGHs and SWEs.

2.3.2 Fourier and Fresnel elements

In the previous section, the different types of free-space digital optics have been introduced. Here, it will be shown that for DOEs and CGHs a further distinction is useful – between *Fourier* and *Fresnel elements*. Both of these encompass a different diffraction regime, namely far- and near-field diffraction respectively [68].

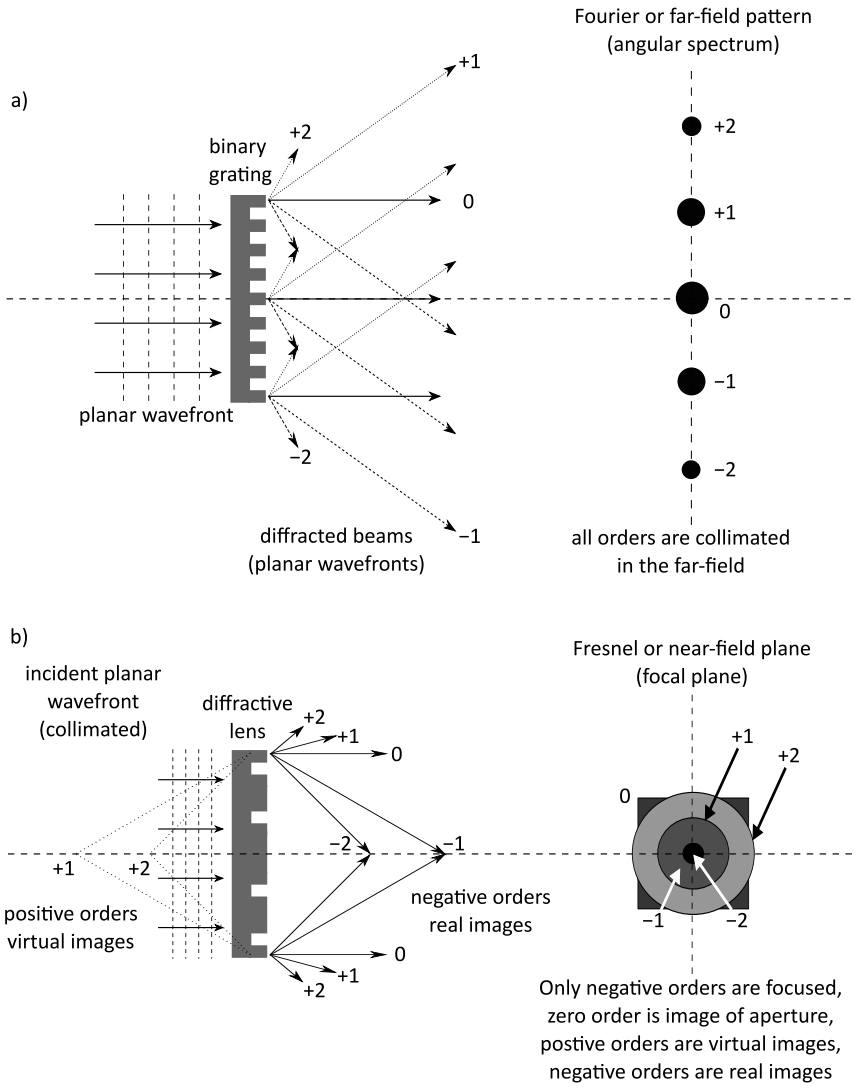

Figure 2.7: Diffraction orders from generic Fourier and Fresnel elements. In a), the diffraction orders are schematically shown for a Fourier element in the far-field. Similarly, in b) this is shown for the near-field of a Fresnel element. Adapted from [68].

A Fourier diffractive element usually consists of a periodic element (Figure 2.7a) which leaves all incoming wavefront characteristics (convergence, divergence or collimation) unchanged, while manipulating the direction of the diffracted wavefront – either in a single or multiple diffraction orders. Thus, the diffraction orders will be collimated if the incoming wavefront is collimated, leading to a distinctive diffraction pattern in the far-field. While the surface profile in Figure 2.7a is rather simple, more elaborate profiles are possible and have been used in this thesis, as will be discussed in section 2.3.5. A Fourier diffractive element is usually referred to as a grating. For a simple one-dimensional grating it is straightforward to calculate the spatial period for a given diffraction angle from the well-known grating equation:

$$m\lambda = \Lambda(n_1 \sin\alpha + n_2 \sin\beta), \tag{2.72}$$

where m is the diffraction order, λ is the wavelength of light and Λ is the spatial period. n_1 and α are the refractive index of the surrounding medium and incident angle respectively, while n_2 and β accordingly, are the refractive index in the grating material and the diffracted angle. For experiments at normal incidence ($\alpha = 90°$) with reflective gratings in air ($n_1 = n_2 = 1$), equation (2.72) reduces to the simplified version of the grating equation:

$$m\lambda = \Lambda \sin \beta. \tag{2.73}$$

In contrast, a Fresnel diffractive element will affect both the direction of the diffracted wavefront(s) as well as change its (their) characteristics (Figure 2.7b). A Fresnel element consists of non-periodic structures and is referred to as a diffractive lens. The binary-phase element shown in the example here demonstrates a unique feature of Fresnel elements (compared to refractive optics) – they are converging and diverging lenses simultaneously.

2.3.3 Diffraction grating

Diffraction gratings can be differentiated as binary or multilevel gratings. A binary grating consists of two height-levels: ground level and barrier height. Such a grating can either be a binary amplitude grating – consisting of alternating layers of transparent and opaque regions (very low efficiency). On the other hand, the binary grating could also be a phase grating, which is made of a single material with grooves. The groove depth can be varied to optimise the diffraction efficiency and is maximised if it induces a phase shift of π for which a theoretical efficiency of 40.5% in the fundamental diffracted order is possible; the conjugated fundamental order has the same efficiency, while the efficiency falls off over the higher-order beams [68]. The π-phase shift is the most efficient as the grating does not produce a zero-order beam due to destructive interference.

A generic binary grating is schematically shown in Figure 2.8. In addition to the groove depth d, another important parameter to design a grating is the *duty cycle*. The duty cycle of a grating is given by the ratio of the spatial period and the groove width, i.e. Λ/a. Knowledge of the groove depth and duty cycle allow the design of any binary grating [69]. So, if both fundamental diffraction orders are used a theoretical efficiency of 81% can be achieved. However, the perfect fabrication of such gratings is not possible and limited by the fabrication technique and equipment used. Often seen fabrication defects include surface roughness and slanted barrier walls.

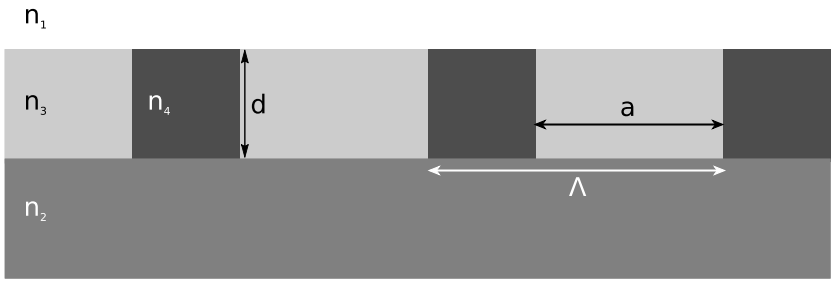

Figure 2.8: Depiction of a binary grating: n_1-n_4 are indices of refraction for the given material layer. The groove depth is represented as d, the spatial period is Λ and the duty cycle. Adapted from [69].

In order to increase the diffraction efficiency beyond the limit of binary gratings, multilevel gratings can be used. Multilevel gratings consist of staircase-type barriers, which attempt to approach an analogous surface profile such as in the blazed grating. A blazed grating can be thought of as an array of microprisms, which are optimised such that the maximum height induces a 2π-phase shift for the desired wavelength. Theoretically, it is possible to reach an efficiency of 100% in the fundamental order since all light is coupled into it, however, due to the already mentioned fabrication defects, the efficiency is usually limited to 90-95% [68].

The discussion of how the light interacts with an arbitrary aperture has been solely relying on the spatial dimensions of said aperture. Hence, it can be appreciated that depending on the shape of an aperture, the far-field behaviour of the lightwave can be manipulated. This has been mathematically formalised in the well-known *Fourier Transform*:

$$P(X,Y,Z) = \int_{aperture} u(x,y,0)\exp\left\{\mathrm{i}\phi_0(x,y)\exp\left[-\mathrm{i}k\frac{xX}{R}\right]\exp\left[-\mathrm{i}k\frac{yY}{R}\right]\right\}dx\,dy, \tag{2.74}$$

where $u(x,y,0)$ is the complex amplitude in the aperture plane, the term $\exp[\mathrm{i}\phi_0(x,y)]$ accounts for the phase variations over the aperture, x and y are coordinates in the aperture plane and X and Y are coordinates in the evaluation plane. k is representing the wavenumber and R is the distance between the origin and a point on the evaluation plane. This expression is sometimes also given in its compact form $P(X,Y,Z) = \mathcal{F}\left[u(x,y,0)exp\left\{\mathrm{i}\phi_0(x,y)\right\}\right]$, which demonstrates that the far-field diffraction pattern is the Fourier transform of the aperture function [66] – a detailed derivation proving this can be found in Appendix A.

While the derivation of the Fourier transform allows to appreciate the link between aperture and resulting diffraction pattern, real diffractive optics are sometimes violating the assumptions about a mediums homogeneity, linearity and whether it is isotropic or not (see Appendix A). This is especially true for the regime of nanograt-

ings, which will be discussed in the next section.

2.3.4 Nanogratings

Depending on the spatial period Λ of the grating, different diffraction realms can be accessed. Generally, for spatial periods down to $\Lambda \simeq 5\lambda$, the scalar regime can be applied and is often referred to as macro-optics. For $\Lambda \simeq \lambda$ is the extended scalar regime; $\Lambda \simeq \lambda/5$ enters the regime of sub-wavelength gratings (nano-optics) and $\Lambda \simeq \lambda/20$ opens the regime of photonic crystals [68]. Importantly, for SWEs, the spatial period only allows a zero-order diffracted beam, which is why SWEs are sometimes also referred to as zero-order gratings.

However, while this definition relies purely on the spatial period, it has recently been shown that the regime of nano-optics can also be accessed for spatial periods in the scalar regime, if the feature sizes of the barriers inside the spatial period are subwavelength [70]. If the feature sizes are approaching the subwavelength-regime, the term *metasurface* is often used to describe the resulting structure. Such metasurfaces can lead to behaviour that cannot be predicted in the macro-optics regime. For example, it is well-known that the *Fresnel equations* and *Snell's law* can be used to predict the behaviour of an electromagnetic wave incident on a boundary between two homogeneous media with different indices of refraction: The incident beam will split into a reflected and a refracted beam. Fresnel equations are used to determine the transmission and reflection coefficients, while Snell's law is used to calculate the directions of the beams.

When an electromagnetic wave is incident on a metasurface however, the conditions at the boundary change dramatically. The first study demonstrating such a behaviour was reported by Capasso's group in 2011 [71]. They investigated a metasurface consisting of a gold array on a silicon wafer. The gold array unit cell was comprised of eight kinds of V-shaped antennas with a thickness of about 50 nm. Each antenna was about 220 nm wide and the unit cell size in the x-direction varied from 11 μm to 21 μm, while the y-direction was kept constant at 1.5 μm (see Figure 2.9**A**). For an incident electromagnetic wave with a wavelength of 8 μm (y-polarised), the reflected and refracted beams, or *ordinary beams*, as calculated by Snell's law were not observed. The actual beams observed were bend in unexpected angles and are therefore called *anomalous beams*.

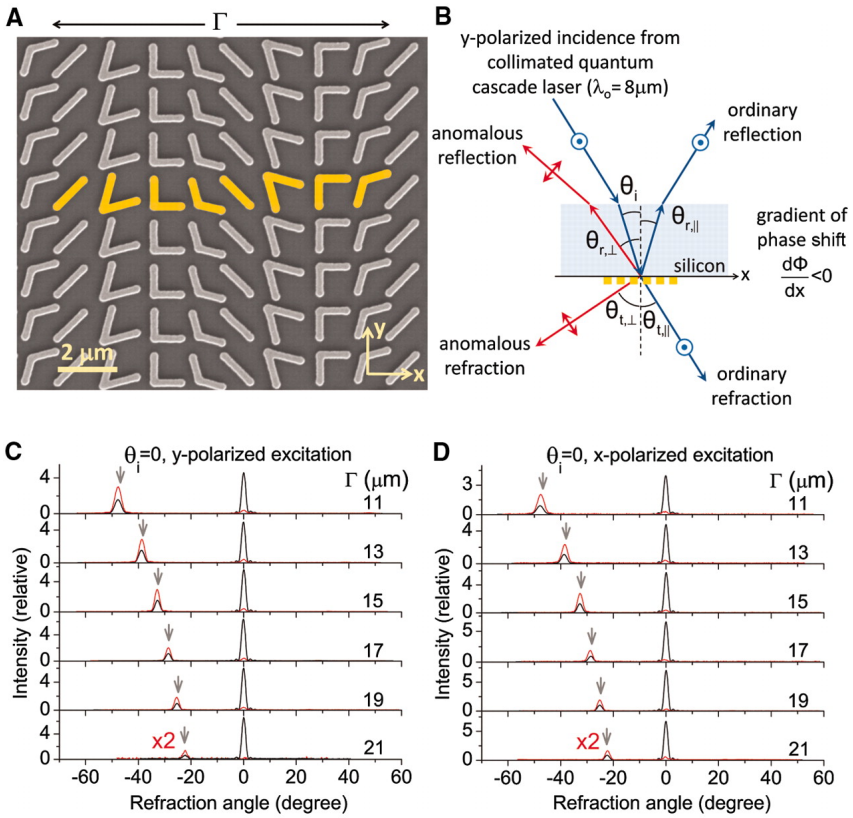

Figure 2.9: (**A**) Scanning electron microscope (SEM) image of a representative antenna array fabricated on a silicon wafer. The unit cell of the plasmonic interface (yellow) comprises eight kinds of gold V-antennas of width ≈220 nm and thickness ≈50 nm, and it repeats with a periodicity of $\Gamma = 11$ μm in the x-direction and 1.5 μm in the y-direction. (**B**) Schematic experimental setup for y-polarised excitation (electric field normal to the plane of incidence). (**C** and **D**) Measured far-field intensity profiles of the refracted beams for y- and x-polarised excitations, respectively. The refraction angle is counted from the normal to the surface. The red and black curves are measured with and without a polariser, respectively, for six samples with different Γ. The polariser is used to select the anomalously refracted beams that are cross-polarised with respect to the excitation. The amplitude of the red curves is magnified by a factor of two for clarity. The gray arrows indicate the calculated angles of anomalous refraction. Reprinted from [71] with permission from AAAS (appendix D).

The boundary and beams are schematically shown in Figure 2.9**B**. In order to account for the anomalous beams, a generalised version of Snell's law was proposed. The authors showed that the gold antennas could be treated as sub-wavelength resonators, which induced an effective current within the metasurface. This effective current can be associated with an effective phase change Φ that can be controlled by the unit cell design of the metasurface. The magnitude and direction of the phase gradient along the interface $d\Phi/dx$ in combination with the refractive index of the surrounding medium can be used to bend the anomalous beams in an arbitrary direction [71]. The authors demonstrated that a generalised Snell's law can be

derived by considering *Fermat's principle of least action*, which *'can be stated as the principle of stationary phase; that is, the derivative of the phase accumulated along the actual light path will be zero with respect to infinitesimal variations of the path'* [71]. If this principle of stationary phase is applied to the interface given in Figure 2.9**B**, the authors showed that the total phase shift of the optical path of the light to the point of constructive interference is still zero in the presence of rapid phase jumps induced by the metasurface.

Physically, this generalised Snell's law explains the anomalous refraction observed for the normal incidence measurements reported by Yu et al. [71]. The authors showed that with decreasing unit cell size in the x-direction, i.e. bringing the gold antennas closer together, leads to an increase in angle of refraction (Figure 2.9 **C** and **D**). Anomalous bending of light perfectly illustrates the need for careful attention when interpreting optical phenomena occurring at length scales comparable to and especially lower than the wavelength of the light.

2.3.5 Fabrication of plasmonic nanogratings

This section aims to describe the nanofabrication process of gold nanogratings used in this thesis by means of electron beam lithography (EBL), which is briefly introduced as one of the techniques used for nanofabrication [72]. However, other fabrication techniques do exist, which are comprehensively described in this review and recommended to the reader [73].

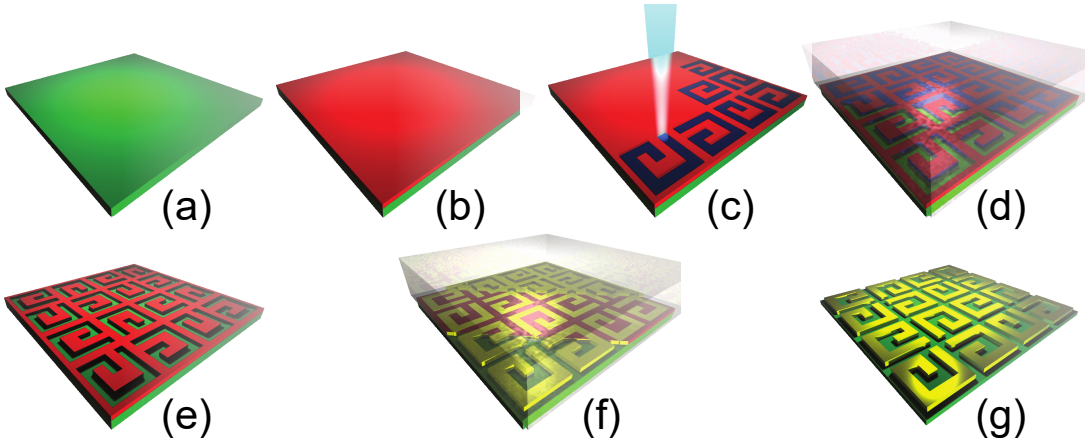

Figure 2.10: Fabrication process of nanostructured plasmonic diffractive optical element. a) An appropriate silicon wafer forms the base of the optical element (green layer). b) A double resist layer, typically consisting of a thin polymer film, is spin-coated on the wafer (red layer). c) Exposure: the nanostructures' pattern is drawn on the resist with a focused electron beam. d) Development: a solvent removes the resist within the pattern. e) Drying of the resist produces a resist pattern. f) Following the metal evaporation (gold layer) follows the lift-off: all of the resist is removed in a solvent bath. g) The sample is ready for measurements. Adapted from [74].

The grating fabrication process of the gold nanogratings is shown in Figure 2.10. Depending on the application a suitable wafer has to be chosen. A wafer consisting of silicon and silica glass is widely used for experiments in reflection (Figure 2.10a). For transmission based experiments, the silicon layer can be omitted. A thin polymer film, also called the *resist*, is coated onto the wafer (Figure 2.10b). The resist can now be patterned by a focused beam of highly energetic electrons scanned in a chosen pattern, in Figure 2.10c a G-shape pattern is used as an example. The exposed area of the polymer can now be further processed in the *development* phase. The resist can be developed in two ways: Depending on the tone of the resist – positive or negative – the exposed regions are either removed (positive) or remain (negative) during development [72]. In Figure 2.10d a positive resist was chosen as an example. After the development, depending on the tone of the resist, the result will either be a continuous polymer film with holes (as in Figure 2.10e) or 'islands' of the resist. The result of the development phase is what is referred to as a *resist pattern*, in this case a binary grating (see Section 2.3.3), which is controlled by the resist layer [75].

The photomask functions as the template for the subsequent deposition process. Various alternative deposition processes exist. Examples include ion implantation and electroplating, however more commonly, a concentrated ion beam is used to transfer the pattern of the resist into the chosen substrate. Alternatively, physical vapor deposition (in most plasmonic applications the vapor would be either gold or silver) is used to deposit material both atop the remaining resist and exposed parts

of the resist (i.e. atop the substrate). In the final step, the remaining resist layer is removed in the *lift-off* phase and as a consequence the unwanted layer (here gold) deposited atop, is also removed (Figure 2.10f). The result is the final binary pattern as shown in Figure 2.10g.

In traditional optical lithography, the photomask has to be produced prior to the lithographic process. The advantage of EBL is that no pattern generator is required, since the electron beam is taking that role directly [75]. Furthermore, while optical lithography is diffraction limited by the optical wavelength such that the best resolution cannot be better than $\frac{\lambda}{2}$, in EBL it is the electron de Broglie wavelength which is important. If the wavelength of a photon is calculated at 2 eV with the formula $\lambda = \frac{hc}{E_{ph}}$ [76], where h is Planck's constant and c the speed of light in vacuum, the corresponding wavelength is found to be 621 nm. Meanwhile, the kinetic energy of an electron is determined with respect to its momentum as $E_e = \frac{p^2}{2m_e}$, where m_e is the electron rest mass, i.e. $9.109 \cdot 10^{-31}$ kg. For a given kinetic energy of 2 eV, the corresponding momentum is 7.63×10^{-25} kgm/s. The de Broglie wavelength of the electron is defined as [76]:

$$\lambda = \frac{h}{p}, \tag{2.75}$$

which results in a wavelength of 0.87 nm for the given values – approaching a three orders of magnitude improvement in resolution. However, technical limitations exist such as the ability to focus the electron beam. Focus resolution down to the sub-nanometre regime has been reported [66]. However, depending on the energy of the electrons used, secondary processes such as scattering inside the resist can occur, which lead to a trade-off between small feature sizes and shape quality; typically allowing feature sizes of about 10 nm [75].

For the nanogratings studied in this thesis, the following procedure was followed in the sample fabrication: 10 mm x 10 mm x 525 μm single-side polished Si(p-doped)-SiO2(300 nm) samples are sonicated in successive baths of acetone and IPA (isopropyl alcohol) for 10 minutes, blow dried with compressed ultra-high purity (UHP) N_2 and dehydrated on a hotplate (200 °C, 20 minutes). UV1116-0.5 (Dow Chemical Company) chemically amplified positive-tone photoresist is spin-coated (5,500 rpm, 45 s) and soft-baked on a hotplate (130 °C, 2 mins), resulting in a final thickness of ≈350 nm. 80 kV electron beam lithography (Nanobeam, nB^{-1}) is used for the high-resolution patterning, with exposure conditions: pattern optimised area dose between 40–100 μC cm^{-2}, 1.8 nA operating current and a 38 μm main field [72]. A post-exposure bake on a hotplate is performed at 130 °C, 90 s. The samples are developed in MF-CD-26 for 10 s, followed by a deionised (DI)-water rinse for 3 mins and N_2. Physical vapour deposition of Cr/Au (3/30 nm) is performed using a thermal evaporator (Edwards E306) at a base pressure ≈ 10^{-6} mbar, at

an evaporation rate ≈0.1 nm s^{-1}. Resist lift-off is carried out in NMP (N-Methyl-2-pyrrolidone) at an elevated temperature of 60 °C for 4 hours, followed by fresh NMP sonication for 2 mins, acetone, IPA rinse and UHP N_2 blow dry. For nanoscale surface quality inspection, a Zeiss LEO 1530 VP Scanning Electron Microscope (SEM) operating at 5 keV was used and the SEM micrographs are shown in Figure 5.1.

2.3.6 Far-field response of plasmonic nanogratings

For such optical diffraction gratings the grating equation can be used to determine the spatial distribution of the diffracted light:

$$I = I_0 \frac{\sin^2\left(N\frac{\phi}{2}\right)}{\sin^2\left(\frac{\phi}{2}\right)}, \tag{2.76}$$

where I is the intensity, I_0 is the zeroth-order intensity, N represents the number of slits and ϕ is the phase angle [77]. For more complex gratings, the intensity of each diffracted beam is governed by the shape and nature of each unit cell. This complexity leads to introducing additional design parameters that can be exploited to create a variety of possible power distributions in the diffracted beams, such as the duty cycle, which is the ratio of the feature dimensions to the periodicity of the grating (see Section 2.3.3) [78]. This factor alone can cause extreme changes in the envelope function of the intensity distribution and has spurred interest in its design [66, 79, 80]. The grating equation assumes regular periodic point sources interfering in the far-field. For nanogratings as described in the previous section, the periodic near-field hotspots themselves are large compared to the wavelength of light. Because of this, they do not behave as point sources, and thus the far-field diffraction pattern depends on both the array's periodicity, and the nontrivial near-field response of individual structures. Klimov et al. [81] recently proposed an intuitive method to cope with such structures theoretically. Here, the authors describe the far-field of such nanostructures as:

$$E_{\mathrm{far-field}} = \sum_{n=-\infty}^{\infty} \sum_{m=-\infty}^{\infty} C_{nm} \exp\left(-ik_{x,n}x\right) \exp\left(-ik_{y,m}y\right) \exp\left(-ik_{z,nm}z\right), \tag{2.77}$$

where, $k_{x,n} = 2\pi n/W$, $k_{y,m} = 2\pi m/W$ and $k_{z,nm} = -\sqrt{k^2 - k_{x,n}^2 - k_{y,m}^2}$ are the components of the wavevector associated with the n,m diffraction order, k is the absolute value of the wavevector, W is the periodicity of the grating and x, y, z are Cartesian coordinates for a coordinate system located at the source of the incident light and the z-axis pointing away from the structure. The Fourier coefficients C_{nm}

can be calculated from the near-field, i.e.:

$$C_{nm} = \frac{1}{W^2} \int_0^W \int_0^W E_{near-field} \exp\left(\mathrm{i}\left(k_{x,n}x + k_{y,m}y\right)\right) dxdy. \tag{2.78}$$

These equations are general and, for simple gratings, they result in equation (2.76). For all but the simplest cases, $E_{near-field}$ needs to be obtained numerically. The two main methods used for numerical studies of nanogratings are discussed in the next section.

2.3.7 Modelling diffractive optics

Solving the time-harmonic Maxwell's equations at the boundary of the grating structure will provide the correct result of the diffraction problem. However, it is very difficult to derive an analytical expression for a given diffracting element. Hence, numerical methods have been proposed in the past, to solve more elaborate systems. Since there is a variety of these methods, only the main numerical methods are briefly introduced – the finite-difference-time-domain (FDTD) and the rigorous coupled wave analysis (RCWA) method.

RCWA aims to determine the coupling effects between the various diffraction orders to solve the diffraction problem [68]. By using the wave equation (2.35) and linking it to the spatial harmonics of a given diffraction problem, a set of relations is obtained. This set of relations can be expressed in a matrix form and can be solved by determining the eigenvectors and eigenvalues of the resulting matrix. However, since the complete set of relations will be extremely large, only the lower diffraction orders are considered and all others ignored. Such a matrix truncation of an eigenvalue problem can cause high fluctuations between the 'real' and the simplified eigenvalue of the matrix. Other sources of error exist, such as Wood's abberation leading to highly energetic diffraction near the evanescent limit (i.e. diffraction along the element boundary). However, RCWA is very useful when the grating element can be approximated as a perfect dielectric or an absorbing medium, since the real permittivity for such materials is generally known. Thus, RCWA is mostly used to model dielectric homogeneous diffraction problems with a low number of diffraction orders [68].

FDTD methods on the other hand aim to solve Maxwell's equations directly for

a chosen surface profile. Given Faraday's law of induction and Ampére's circuit law:

$$\vec{\nabla} \times \vec{E} = -\mu \frac{\partial \vec{H}}{\partial t}, \tag{2.79a}$$

$$\vec{\nabla} \times \vec{H} = \sigma \vec{E} + \epsilon \frac{\partial \vec{E}}{\partial t}. \tag{2.79b}$$

In 2D, these expressions can be used to describe a TE polarised lightwave with a set of partial differential equations [68]:

$$\frac{\partial E_z}{\partial t} = -\frac{1}{\epsilon}\left(\frac{\partial H_y}{\partial x} - \frac{\partial H_x}{\partial y}\right), \tag{2.80a}$$

$$\frac{\partial H_y}{\partial t} = -\frac{1}{\mu}\frac{\partial E_z}{\partial x}, \tag{2.80b}$$

$$\frac{\partial H_x}{\partial t} = -\frac{1}{\mu}\frac{\partial E_z}{\partial y}. \tag{2.80c}$$

In order to solve this set of partial differential equations, the well-known finite difference method can be applied [68]:

$$\frac{\partial f(M)}{\partial x} = \lim_{\Delta x \to 0}\left(\frac{f(B) - f(A)}{\Delta x}\right) \approx \frac{f(B) - f(A)}{\Delta x}. \tag{2.81}$$

In order to solve the set of equations (2.80a)-(2.80c), with the finite difference method, while also reducing the necessary computational resources, a special sampling technique is applied – *interleaved* sampling. Here, both the space and time dimension are sampled and the results combined. To illustrate this point, a small simulation area, or cell, can be imagined. Along the boundary of such a cell, the electric field components need to be obtained, while the magnetic field components are directed orthogonally through the centre of the cell, this is schematically shown in Figure 2.11a i). The great advantage of FDTD methods lies in the fact that the set of partial differential equations does not strictly need to be solved simultaneously. Instead, at a time t, the electric field components are updated by obtaining the spatial derivative of the magnetic field within the cell. Subsequently, at a later time $t + \Delta t$, the electric field derivative is obtained and used to update the magnetic field – this concept is illustrated in Figure 2.11a i)-ii).

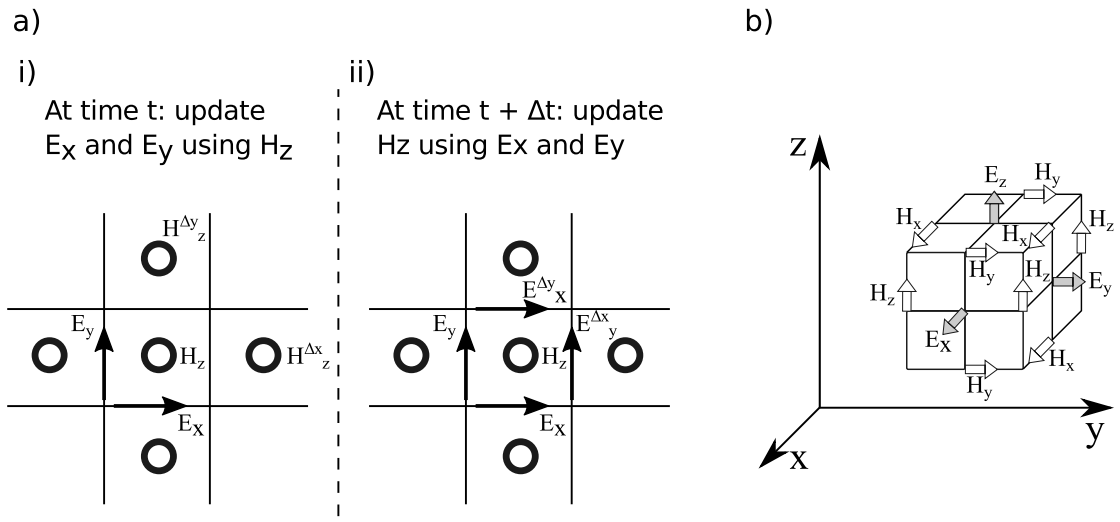

Figure 2.11: Principle of finite difference time domain (FDTD) modelling. In a), a 2D simulation mesh grid is simulated. In FDTD, a single cell is simulated by determining the values of the electric field components by calculating the change in H_z for neighbouring cells at a time t i). Similarly, at a later time $t + \Delta t$, the magnetic field component in the z-direction is updated by calculating the change in the electric field components at that time ii). The resulting E-H fields can then be interleaved in space and time to converge on a solution for the electromagnetic field. In b), a three-dimensional space sampling is schematically shown. Such a cell is referred to as the *Yee cell*. Adapted from [68].

For a 3D simulation, the grid mesh of the previous example evolves into a space lattice known as a *Yee cell* (Figure 2.11 b). The Yee cell is used to locate the E and H fields in space while the sampling is time-stepped. In summary, for the FDTD method, the computation takes the following form: Update the E fields everywhere using H. At a later time, update H everywhere using E. After every cell has been updated, the boundary condition $\hat{E}_y^{i,j+1/2} = 0$ is applied for all nodes in the simulation region, where i and j are integers associated with the nodes along the x- and y-axis respectively [68]. Additionally, the diffractive element needs to be placed within an absorbing boundary to account for the scattered light. Such a system is schematically shown in Figure 2.12.

This generic FDTD algorithm allows the convergence towards a solution of the numerical method. The main advantages of the FDTD method are the broad applicability, including inhomogeneous, anisotropic media as well as periodic and non-periodic structures. A disadvantage of FDTD lies in the fact that each mesh cell is typically as small as $\lambda/20$ to ensure accuracy and FDTD solvers therefore heavily rely on strong CPU processing [68]. Furthermore, the implementation of nonorthogonal grids is difficult and not supported by many solvers, which sometimes requires even finer meshes. However, not including such systems and taking into account material properties, it is possible to accurately model a broad range of diffraction

problems. Today, FDTD is a widely used modelling method in the field and has been chosen for this thesis. A more detailed description of FDTD methods can be found in the literature [66].

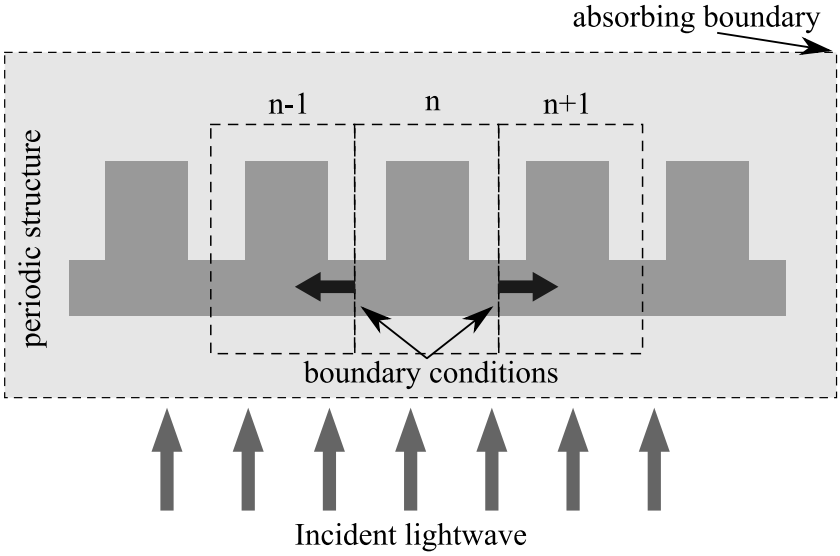

Figure 2.12: Example of the use of fictitious boundaries to minimise computational time and improve simulation convergence. A periodic structure is placed within an absorbing boundary to determine the amount of scattered light. The spatial period is exploited by a secondary boundary placed around the unit cell n, with periodic boundary conditions applied to account for neighbouring unit cells ($n-1$, $n+1$, etc). Adapted from [68].

2.4 Summary and conclusion

In this chapter, the theoretical foundation for the work presented in this thesis has been presented. Chirality as a symmetry property of nature has been discussed. Stationary objects are referred to as chiral if they lack mirror symmetry, which can drastically change their properties. The mathematical framework to understand the origin of chirality as well as its effect on the interaction of light and matter has been elaborated. The change of light-matter interaction as a means to detect chirality in media is elaborated. As part of this discussion, the main mathematical methods to describe chiral media have been introduced and their relationship as well as advantages and limitations shown.

Following the section on chirality, the phenomenon of plasmonics was introduced. As was shown, when light of a characteristic (material and shape dependent) frequency is incident on a metal surface (from a dielectric environment), it can cause the free valence electrons to oscillate. This oscillation of electrons can lead to highly concentrated electromagnetic fields in the proximity of the metal. The Quanta associated with the electron oscillation is called a plasmon. Different types of plasmons

(volume and surface plasmons) have been introduced and the ways in which their properties depend on the shape and type of metal as well as the surrounding dielectric discussed.

The final section embodies a brief introduction into the field of diffractive optics. First, the physics of light interference as well as diffraction are briefly presented. This is followed by a discussion of diffractive elements with a special focus on diffraction gratings. The various design parameters that can be explored to manipulate light are demonstrated and the accompanying mathematical formulas communicated. Consequently, it is shown how the physics of diffraction changes when the feature sizes approach (or are even smaller than) the wavelength of light. Electron beam lithography as a means to fabricate such nanogratings is presented as the chosen method for this thesis. Subsequently, the numerical methods used to model such nanogratings are given with a special focus on the RCWA and the FDTD methods.

The concepts of chirality, plasmonics and diffractive optics are the foundation of the research presented in the following chapters. The development of an experimental apparatus to study chiral plasmonic nanogratings will be outlined and both RCWA and FDTD used to explain the measured chiroptical response.

Chapter 3

Experimental Methodology

Circular dichroism (CD) spectrometers are in widespread use in both pharmacology and chemistry today [82–84]. Since this work aims to measure both molecular CD as well as CD from solid nanostructures, this section will start by outlining the setup and workings of a commercially available CD spectrometer. Subsequently, I developed a CD spectrometer to measure the CD of liquid isotropic samples and consequently adapted it for reflecting nanogratings. Limitations and the consequent evolution of the developed CD spectrometer are outlined and the final experimental apparatus presented.

3.1 Photoelastic modulator versus quarter-waveplate

3.1.1 Commercial CD spectrometer

A commercial CD spectrometer (Chirascan, Applied Photophysics) has been used as a reference unit for this thesis [85]. The optical setup of the Chirascan is shown schematically in Figure 3.1. A 150 W xenon lamp is used as the light source and individual wavelengths are generated in the monochromator unit. In the monochromator unit, a set of prisms is used to control the wavelength of the light incident on a photoelastic modulator (PEM). A PEM contains a transparent crystal which is birefringent. A birefringent material changes its optical properties under mechanical stress. If such a birefringent material is subjected to compression and stretching, the linear component of a lightwave parallel to the modulator axis is travelling slightly faster or slower through the crystal with respect to the perpendicular wave component. This change of velocity induces a phase shift in the lightwave which depends on the material thickness and in this setup is set to cause a quarter-wave retardation and quickly oscillates between right- and left-circularly polarised (RCP and LCP) light (typically at 50 kHz); see Section 2.1.4 for a detailed explanation of chiral

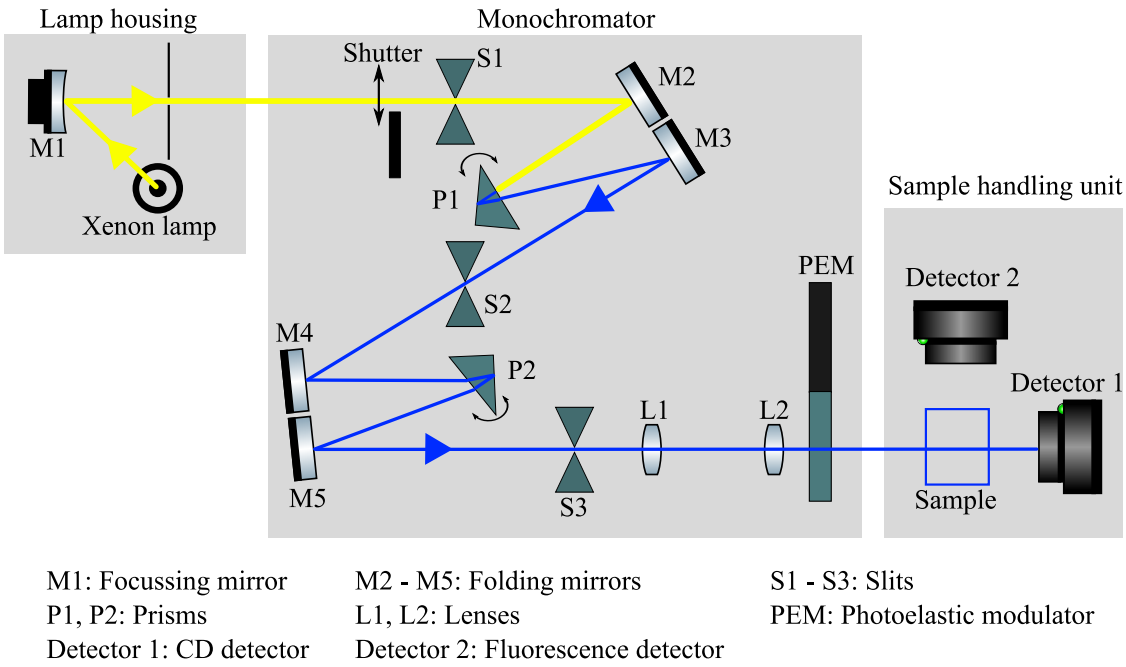

Figure 3.1: Schematic of the optical path in the commercial Chirascan CD spectrometer. The light from a xenon lamp is directed through a pinhole by a focussing mirror and into the monochromator unit. In the monochromator unit the wavelength is changed via a pair of prisms and mirrors and the converted into circularly polarised light be a PEM. The circularly polarised light is then incident on a sample contained in a glass cuvette and the scattered and transmitted light measured in two photodetectors. Adapted from user manual [86]. Component drawings were adapted from the component library by Alexander Franzen [87].

light. The sample to be analysed is contained within a glass cuvette and situated in the sample handling unit. The transmitted beam is incident on two detectors to measure CD and fluorescence respectively. The CD detector is an avalanche photodiode consisting of a semiconductor (typically silicon for the visible and infrared spectrum of light) to which a reverse bias voltage is applied. If light is incident on the detector array an avalanche effect is triggered due to the photovoltaic effect. The avalanche effect leads to a gain in the produced photocurrent which is proportional to the power of the incident light and is a widely used light detection device. The fluorescence detector is used to measure the scattered light with a photomultiplier tube which exploits the photoelectric effect to measure low intensity light. During a measurement, the prisms are rotated automatically, to adjust the wavelength of the light incident on the sample. The output power as a function of wavelength is measured and the results are converted into ellipticity or CD.

Typically, the chiral molecules measured are dissolved in a solvent, such as water or chloroform. In order to isolate the chiroptical response of the chiral molecules, the response from the solvent is measured first. Subsequently, the response from the dissolved chiral molecules is measured and the ratio (or difference) of the two

results is used to acquire a normalised chiroptical response [86].

3.1.2 Experimental apparatus

The initial setup is shown in Figure 3.2. The CD spectrometer uses a femtosecond (fs) laser (Mai-Tai, Spectra-Physics) as the pump (tuning wavelength 690-1040 nm and average power at 800 nm is 2.5 W) to operate a highly-tunable optical parametric oscillator (OPO) (Inspire, Spectra-Physics). An OPO can be employed to convert an input signal into two beams of lower frequencies via second-order nonlinear optical interactions [88]. This second-order nonlinear conversion is achieved by means of nonlinear optical crystals (for example lithium niobate) which are birefringent and have changing phase-matching conditions depending on their orientation. The pump lightwave is split into two beams known as signal and idler. The interaction between the pump and these two resulting beams leads to a de-amplification of the pump beam and consequently either the signal or the idler (or both) are amplified. The wavelengths of the signal and idler beams depend on the phase-matching conditions of the crystal. An optical resonator consisting of a suitable gain medium and mirrors is then used to amplify the desired beam (depending on the target wavelength) further. This system provides a spectral tuning range of 345-2500 nm and an average output power between 350-1100 mW, depending on the mode of operation and the wavelength [89]. Two uncoated Glan-Laser polarisers are used to control the power and polarisation of the generated beam. The second polariser is fixed to an orientation of 45° relative to the plane of incidence. The reason behind the 45° orientation of the linear polariser is discussed in detail in Section 3.1.2.1 but essentially enables the generation of fully circularly polarised light by the PEM. The PEM then modulates the polarisation to produce equal amounts of LCP and RCP light at a frequency of 50 kHz. The modulated beam is transmitted through the cuvette containing the sample and detected by a silicon avalanche photodiode (Thorlabs). The photodiode is connected to a Lock-in amplifier (Stanford Research) and triggered at the modulation frequency of the PEM.

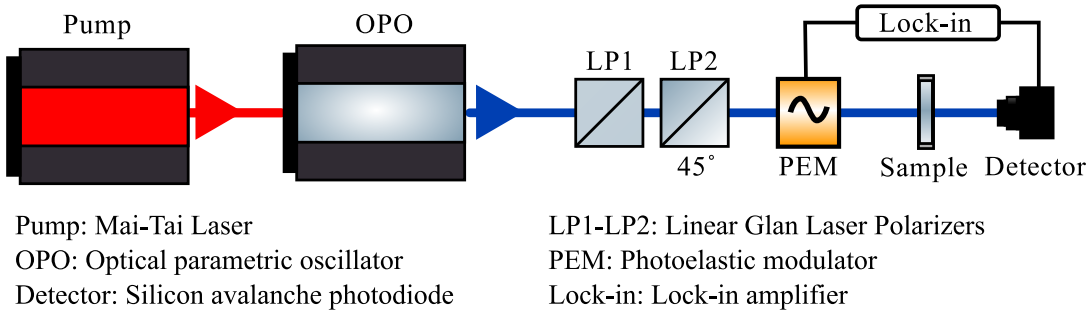

Figure 3.2: Schematic of initial apparatus with a Mai-Tai laser used to pump an OPO. The output beam was tunable between 345-2500 nm. The linear polariser LP2 is oriented at 45° degrees to the optical axis of the PEM so as to produce circular polarisation. The preceding linear polariser LP1 can be rotated with respect to LP2, to provide control over the power transmitted through LP2. The light transmitted by the sample was detected with an avalanche photodiode and used in combination with a lock-in amplifier and modulated at the PEM-modulation frequency.

The conversion of the measured voltage into a CD response can be achieved via *Stokes Analysis* – presented for the case of this setup in Section 3.1.2.2.

3.1.2.1 Application of Jones calculus to the developed apparatus

The commercial CD spectrometer and the developed apparatus are both based on the use of PEMs, therefore it is crucial to understand how a PEM operates. The operation of a PEM in combination with a linear polariser, orientated at 45° to the plane of incidence, can be understood by means of Jones calculus [90]. The Jones vector associated with a light beam can generally be expressed as [90]:

$$\begin{pmatrix} E_x \\ E_y \end{pmatrix}, \tag{3.1}$$

with E_x and E_y representing the x- and y-components of a lightwave. The Jones matrix for a linear polariser is given by [90]:

$$P_L = \begin{pmatrix} \cos^2\alpha & \sin\alpha\cos\alpha \\ \sin\alpha\cos\alpha & \sin^2\alpha \end{pmatrix}, \tag{3.2}$$

where α is used as the angle of polarisation with respect to the vertical plane, normal to the direction of propagation.

The effect of different linear polariser orientations on the light transmitted by the PEM can be understood by examining three different cases: $\alpha = 0, \frac{\pi}{4}, \frac{\pi}{2}$. The polarisation of the beam incident on the PEM can be studied by means of calculating the product of equations (3.1) and (3.2) for these different values of α. The resulting

linear polarisation states are:

$$L_0 = \begin{pmatrix} E_x \\ 0 \end{pmatrix} \tag{3.3a}$$

$$L_{\frac{\pi}{2}} = \begin{pmatrix} 0 \\ E_y \end{pmatrix} \tag{3.3b}$$

$$L_{\frac{\pi}{4}} = \frac{1}{2}\left(E_x + E_y\right)\begin{pmatrix} 1 \\ 1 \end{pmatrix}. \tag{3.3c}$$

The Jones matrix of a PEM is given by:

$$J_{\mathrm{PEM}} = \begin{pmatrix} 1 & 0 \\ 0 & e^{\mathrm{i}A(t')} \end{pmatrix}, \tag{3.4}$$

with the amplitude of modulation given by $A(t') = \cos(\omega t')$, where ω represents the angular frequency of the modulation. Multiplying the three cases (3.3) with the PEM Jones matrix, results in the three transmitted polarisation states with respect to the orientation of the linear polariser:

$$L_{0,\mathrm{PEM}} = \begin{pmatrix} E_x \\ 0 \end{pmatrix} \tag{3.5a}$$

$$L_{\frac{\pi}{2},\mathrm{PEM}} = \begin{pmatrix} 0 \\ E_y e^{\mathrm{i}A(t')} \end{pmatrix} \tag{3.5b}$$

$$L_{\frac{\pi}{4},\mathrm{PEM}} = \frac{1}{2}\left(E_x + E_y\right)\begin{pmatrix} 1 \\ e^{\mathrm{i}A(t')} \end{pmatrix}. \tag{3.5c}$$

Studying this result, it can be seen that only in the last equation, i.e. for a polariser orientation of $\alpha = \frac{\pi}{4}$, yields a wave oscillating between a fully RCP and LCP polarisation state.

3.1.2.2 Stokes analysis to obtain CD from the experimental setup

The aim of *Stokes analysis* is to describe the behaviour of light polarisation and can be used to link measurable quantities, such as the intensity, to chiroptical responses. The state of polarisation is described by the Stokes' parameters, which are often presented in vector form:

$$\vec{S} = \begin{bmatrix} I \\ Q \\ U \\ V \end{bmatrix}, \tag{3.6}$$

where I is the total intensity, the fractional degree of polarisation Q and the shape parameters of the polarisation ellipse U and V [24]. Similar to the previously used Jones calculus, each component in the optical beam path can be represented by a matrix, known as a *Mueller-Matrix* [90]. Multiplying the Mueller-Matrices of all components in the beam path by the Stokes vector of the initial lightwave for the experimental apparatus will result in a Stokes vector for that setup:

$$\vec{S}_{\text{final}} = M_{\text{Sample}} M_{\text{PEM}} M_{\text{Polariser}} \vec{S}_{\text{unpolarised}}, \tag{3.7}$$

with the Mueller-Matrices and the Stokes vector for the unpolarised light given by [90]:

$$M_{\text{Sample}} = \begin{bmatrix} m_{00} & m_{01} & m_{02} & m_{03} \\ m_{10} & m_{11} & m_{12} & m_{13} \\ m_{20} & m_{21} & m_{22} & m_{23} \\ m_{30} & m_{31} & m_{32} & m_{33} \end{bmatrix} \tag{3.8a}$$

$$M_{\text{PEM}} = \begin{bmatrix} 1 & 0 & 0 & 0 \\ 0 & 1 & 0 & 0 \\ 0 & 0 & \cos\delta & \sin\delta \\ 0 & 0 & -\sin\delta & \cos\delta \end{bmatrix} \tag{3.8b}$$

$$M_{\text{Polariser}} = \frac{1}{2} \begin{bmatrix} 1 & 0 & \pm 1 & 0 \\ 0 & 0 & 0 & 0 \\ \pm 1 & 0 & 1 & 0 \\ 0 & 0 & 0 & 0 \end{bmatrix} \tag{3.8c}$$

$$\vec{S}_{\text{unpolarised}} = \begin{bmatrix} 1 \\ 0 \\ 0 \\ 0 \end{bmatrix}, \tag{3.8d}$$

where $\pm$ in the expression (3.8c) represents the polariser in $\pm 45°$ configuration, however for clarity this will be ignored for the derivation. The wave retardation induced by the PEM is represented by δ.

If the matrices are multiplied according to equation 3.7, the resulting matrix is:

$$vecS_{\text{final}} = \frac{1}{2}\begin{bmatrix} m_{00} + m_{02}\cos\delta - m_{03}\sin\delta \\ m_{10} + m_{12}\cos\delta - m_{13}\sin\delta \\ m_{20} + m_{22}\cos\delta - m_{23}\sin\delta \\ m_{30} + m_{32}\cos\delta - m_{33}\sin\delta \end{bmatrix}. \tag{3.9}$$

In order to solve equation (3.9), further simplifications to substitute expressions for the matrix components from M_{Sample} are necessary. As in Sections 2.1.4.1 and 2.3, it is assumed that the material is homogeneous and that chiroptical effects (both linear and circular effects) are small enough to allow the following matrix simplification used in the literature [40].

$$M_{\text{Sample}} \approx I_0 \begin{bmatrix} 1+\frac{1}{2}(LD'^2+LD^2) & -LD & -LD' & CD+\frac{1}{2}(LBLD'-LB'LD) \\ -LD & 1+\frac{1}{2}(LD^2-LB'^2) & CB+\frac{1}{2}(LBLB'+LDLD') & LB' \\ -LD' & -CB+\frac{1}{2}(LBLB'+LDLD') & 1+\frac{1}{2}(LD'^2-LB^2) & -LB \\ CD-\frac{1}{2}(LBLD'-LB'LD) & -LB' & LB & 1+\frac{1}{2}(LB^2-LB'^2) \end{bmatrix}, \tag{3.10}$$

where LD and LB are representing linear dichroism and birefringence respectively, while CD and CB are their circular counterparts. LD' and LB' are the linear dichroism and birefringence measured exactly at 45° and 135° relative to the x-axis. $I_0 = e^{-2k}$, where k is defined as the isotropic amplitude absorption, such that $k = \frac{2\pi\kappa_{\text{ext}}l}{\lambda_0}$, with l as the path length through the medium, κ_{ext} represents the extinction coefficient (see Equation 2.23) and λ_0 the vacuum wavelength. In addition to the previous assumptions, anisotropic effects are considered negligible which will result in $(m_{03} + m_{30})/2 = CD$ and $(m_{12} + m_{21})/2 = CB$ [40]. Furthermore, the linear effects will be small compared to the circular components, such that $LD = LD' = LB = LB' \approx 0$ [40]. Finally it should be noted that since SI units are used, the final ellipticity will be given in radians. As the chiroptical effects are weak, for most cases the small angle approximation is appropriate and shall be applied here as well. The small angle approximation is applied to make the derivation clearer but will be taken into account for the final expression. Hence, the Mueller matrix components can be directly associated with optical effects under specific conditions. So, the Mueller matrix of the sample M_{Sample}, can be approximated by:

$$M_{\text{Sample}} \approx I_0 \begin{bmatrix} 1 & 0 & 0 & CD \\ 0 & 1 & CB & 0 \\ 0 & -CB & 1 & 0 \\ CD & 0 & 0 & 1 \end{bmatrix}, \tag{3.11}$$

which applied to equation (3.9) gives:

$$\vec{S}_{\text{final}} = \frac{I_0}{2}\begin{bmatrix} 1 - CD\sin\delta \\ CB\cos\delta \\ \cos\delta \\ CD - \sin\delta \end{bmatrix}. \tag{3.12}$$

The advantage of Stokes' matrix analysis is apparent when presented in the form shown in equation (3.12) as the first component represents the total measured intensity in the Stokes vector. However, if the more general expression from equation (3.9) is used for the further analysis, i.e.:

$$I = \frac{I_0}{2}\left(m_{00} + m_{02}\cos\delta - m_{03}\sin\delta\right), \tag{3.13}$$

and the sample matrix elements rewritten in terms of linear components for convenience:

$$I = \frac{I_0}{2}\left(a + b\cos\delta - c\sin\delta\right). \tag{3.14}$$

Then, for the given polariser-PEM configuration, the retardation is defined as [24]:

$$\delta(\lambda) = A(\lambda)\sin(\omega t) + \delta_0(A), \tag{3.15}$$

where $A(\lambda)$ is the amplitude of oscillations of the PEM and $\delta_0(A)$ is representing the static strain on the birefringent crystal inside the PEM. Ideally, this static strain is negligible at the chosen modulating frequency. Substituting into equation (3.14):

$$I = \frac{I_0}{2}(a + b\cos\left[a\sin(\omega t)\right] - c\sin\left[a\sin(\omega t)\right]). \tag{3.16}$$

For the general case, i.e. when $\delta_0 \neq 0$, the following trigonometric identities can be used:

$$\cos(x+y) = \cos x\cos y - \sin x\sin y \tag{3.17a}$$

$$\sin(x+y) = \sin x\cos y + \cos x\sin y. \tag{3.17b}$$

Applying these identities to the previous expression and using the infinite integer

Bessel series, yields the following substitutions [90]:

$$\cos\left[A\sin(\omega t)\right] = J_0(A) + 2\sum_{j=1} J_{2j}(A)\sin\left[2j\omega t\right] \tag{3.18a}$$

$$\sin\left[A\sin(\omega t)\right] = 2\sum_{j=1} J_{2j-1}(A)\sin\left[(2j-1)\omega t\right], \tag{3.18b}$$

where J is the Bessel function associated with the amplitude of modulation [24]. Typically, the amplitude is given as $A = 2.4048$, for which it is known that $J_0 = 0$ and $\delta_0 \neq 0$. Substituting these back into the expression for the intensity (3.16):

$$\begin{aligned} I = \frac{I_0}{2}\Bigg(a + \left[b\cos\delta_0 - c\sin\delta_0\right] 2\sum_{j=1} J_{2j}(A)\sin\left[2j\omega t\right] \\ - \left[b\sin\delta_0 + c\cos\delta_0\right] 2\sum_{j=1} J_{2j-1}(A)\sin\left[(2j-1)\omega t\right]\Bigg). \end{aligned} \tag{3.19}$$

From which it can be seen that the intensity can be expressed as the sum of three different terms:

$$I = I_{\mathrm{DC}} + I_\omega + I_{2\omega}, \tag{3.20}$$

with I_{DC} as the DC-component, I_ω the first harmonic and $I_{2\omega}$ the second-harmonic of the modulation frequency, where:

$$I_{DC} = \frac{I_0}{2}a \tag{3.21a}$$

$$I_\omega = -\frac{I_0}{2}\left[b\sin\delta_0 + c\cos\delta_0\right] 2J_1(A) \tag{3.21b}$$

$$I_{2\omega} = \frac{I_0}{2}\left[b\cos\delta_0 - c\sin\delta_0\right] 2J_2(A). \tag{3.21c}$$

If I_0 is expressed in terms of I_{DC}, it can be seen that $I_0 = \frac{2I_{\mathrm{DC}}}{a}$, so that:

$$I_\omega = -\frac{I_{\mathrm{DC}}}{a}\left[b\sin\delta_0 + c\cos\delta_0\right] 2J_1(A) \tag{3.22a}$$

$$I_{2\omega} = \frac{I_{\mathrm{DC}}}{a}\left[b\cos\delta_0 - c\sin\delta_0\right] 2J_2(A). \tag{3.22b}$$

Substituting the values of the linear components from the approximation of the sample's Mueller matrix in equation (3.11), i.e. $a = 1$, $b = 0$ and $c = CD$, and

re-arranging, gives:

$$CD(\omega) = -\frac{1}{\cos\delta_0 2J_1(A)}\frac{I_\omega}{I_{\mathrm{DC}}} \tag{3.23a}$$

$$CD(2\omega) = -\frac{1}{\sin\delta_0 2J_2(A)}\frac{I_{2\omega}}{I_{\mathrm{DC}}}. \tag{3.23b}$$

For a static strain of $\delta_0 = 0$, equation (3.23b) is unphysical (division by zero) and the CD is proportional to I_ω. The numerical values for the Bessel function for typical amplitudes of oscillation can be found in the literature [24], so that the expression for CD becomes:

$$CD(\omega) = -0.963\frac{I_\omega}{I_{\mathrm{DC}}}. \tag{3.24}$$

Conventionally, the CD is measured in degrees and the above expression is in radians, so taking this and the small angle approximation into account, the final expression for the CD becomes:

$$CD(\omega) = arctan\left(-0.963\frac{I_\omega}{I_{\mathrm{DC}}}\right)[^\circ], \tag{3.25}$$

Expression (3.25) allows the direct and meaningful conversion of the measured intensity into CD and hence is the key result of this section.

3.1.3 Comparison of commercial and developed CD spectrometer

Equation (3.25) relates the measured intensity to the actual CD, and thus makes it possible to directly compare the performance of the Chirascan and the developed CD spectrometer. The choice of the appropriate chiral molecule is an important one, since most naturally occurring chiral molecules have their absorption peak in the UV spectral region [91]. The present apparatus cannot address the deep-UV ($\lambda < 350$ nm), for which special optics are required as well as an extended source and detection range. Therefore, the amino acid derivative naphthalenediimide (NDI) was chosen for this performance test and was synthesised by Pantoş' group (Department of Chemistry, University of Bath). NDI typically has its absorption peak at 383 nm [92], which is within the spectral range of the laser system used and thus a prime candidate for this test.

For the performance test, NDI was measured in the commercial CD spectrometer and in the developed apparatus. A 1-cm path length cuvette was chosen, following the standard procedure for CD spectroscopy [93–95]. The result is shown in Figure

3.3 and shows a very good agreement between the Chirascan measurement (black line) and the developed system (red diamonds). The CD peak in both cases agrees with the expected absorption peak.

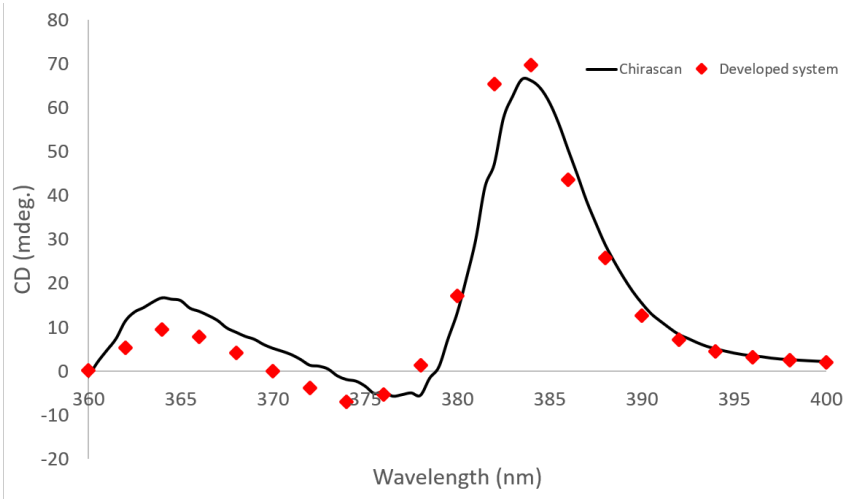

Figure 3.3: CD spectrum for naphthalenediimide as measured in the commercial CD spectrometer (black line) and the developed CD spectrometer (red diamonds). The commercial CD spectrometer data has been averaged over 6 scans.

While the results are promising and crucial to demonstrate the understanding of CD spectroscopy techniques, both spectrometers are based on various assumptions (see Section 3.1.2.2) which are only true for a subset of potentially interesting samples. Specifically, it is only true for isotropic solutions with the chiral molecule dissolved in it. However, this limits the applicability of the spectrometer, since chiral materials have widely different properties when associated with their dissolved and solid state – even more pronounced for reflective and diffractive samples.

The difficulty lies in the determination of the Mueller matrix for the sample in the anisotropic solid state.

3.1.4 Experimental setup for nanogratings

Determining the Mueller matrix of anisotropic solid samples is a well-known issue and has sparked a variety of studies. To determine the Mueller matrix for a wide range of different sample states and materials, both numerical models and experimental approaches based on ellipsometers have been suggested [96–99]. Nonetheless, the necessity for the Mueller matrix can be a disadvantage. Although slower, a conventional quarter-waveplate can generate LCP and RCP light without requiring the Mueller matrix to interpret the measured signals. The variety of approaches has led to differing units used in the literature, including the historical millidegrees [100,101], percentages [80, 102–104] dissymmetry factor [4, 105], and $\frac{1}{\mathrm{Mcm}}$, linking the absorption and the concentration of the sample [6,106,107]. Furthermore, the term *circular*

intensity difference (CID) is sometimes used to refer to chiroptical effects in scattered light, since CD is conventionally being measured in the non-scattered light. Since the purpose of this work is to measure differential scattering, CID shall be used throughout this work.

CID spectroscopy requires the knowledge of the explicit values for the intensities scattered by the sample under LCP and RCP illumination, therefore a modulation between the two is impractical. The adapted apparatus measures the intensities for both polarisations sequentially and the recorded values are subsequently used to calculate the normalised CID value, following:

$$CID = \frac{I_{\mathrm{LCP}} - I_{\mathrm{RCP}}}{I_{\mathrm{LCP}} + I_{\mathrm{RCP}}}, \tag{3.26}$$

where I_{LCP} and I_{RCP} refer to the measured intensities for LCP and RCP illumination.

Using a quarter-waveplate significantly simplifies the detection scheme as well, since the lock-in amplifier is no longer needed and exchanged with an Ocean Optics QE Pro spectrometer. In addition, the fs pulsed laser source is exchanged with a supercontinuum laser to access a broad wavelength range simultaneously. The supercontinuum laser consists of a Fianium SC400-2 2 W laser source with a 1064 nm output wavelength, 20 MHz repetition rate and a 5 ps pulse spliced to an in-house fabricated supercontinuum fiber, described in [108], providing a spectrum between 450 and 2400 nm. The light from the sample is focused with a 20x microscope objective and collected via a 200 μm diameter subminiature assembly (SMA) fibre mounted on the edge of a rotating breadboard at a distance of 25 cm. The polarisation control consists of a superachromatic quarter-waveplate to replace the PEM. The QWP converts the linearly polarised light from the Glan-Laser polarisers into circularly polarised light depending on the orientation of the QWP; 45° for LCP and $-45°$ for RCP light. The detection scheme and optical equipment being used limit the effective spectral range to 450-1000 nm.

Multiple important factors have been considered in the apparatus which shall be discussed briefly. Generally achromatic waveplates are fabricated such that multiple (typically three) birefringent crystals are shaped into wedges and connected to each other. This process allows the simultaneous retardation of a broad wavelength spectrum, however the connected wedges may induce a large beam deviation. The beam deviation is either due to parallelism of the front- and end-face or the contacting method between the individual wedges. Therefore, the QWP chosen for the apparatus had to yield an extremely small beam deviation since the large (30 cm diameter) rotating breadboard used, naturally leads to long optical path lengths. The QWP in the apparatus yields an extremely small beam deviation of < 1 arcsec and its performance was tested as shown in Figure 3.4. By placing an additional

linear polariser between the detection fibre and the QWP, the effect of the beam deviation on the coupling efficiency can be investigated. As can be seen in the figure, the QWP yields a periodic pattern as would be expected.

The light detection by means of microscope objective and SMA fibre has been improved by using 1 inch posts and a fibre launching stage (Thorlabs). The optomechanical stability of the sample has been assured using an x-y-translation stage which is mounted on a 1 inch post as well. The mounting of the system can be seen in Figure 3.5. Typically, an experimental run consists of the light beam incident on a reflective and diffractive sample placed in the centre of the motorised rotation stage. The diffracted light is measured by rotating the breadboard in half-degree-steps. For each angle the polarisation of the incident light is switched from LCP to RCP by rotating the QWP. At each chosen polarisation and angle, a spectrum is recorded and used to calculate the CID. To ensure accuracy and repeatability, the data-acquisition has been automated using an in-house designed Python-based script created by Dr. J. Stirling [109] and adapted by J. T. Collins [110] supported by myself.

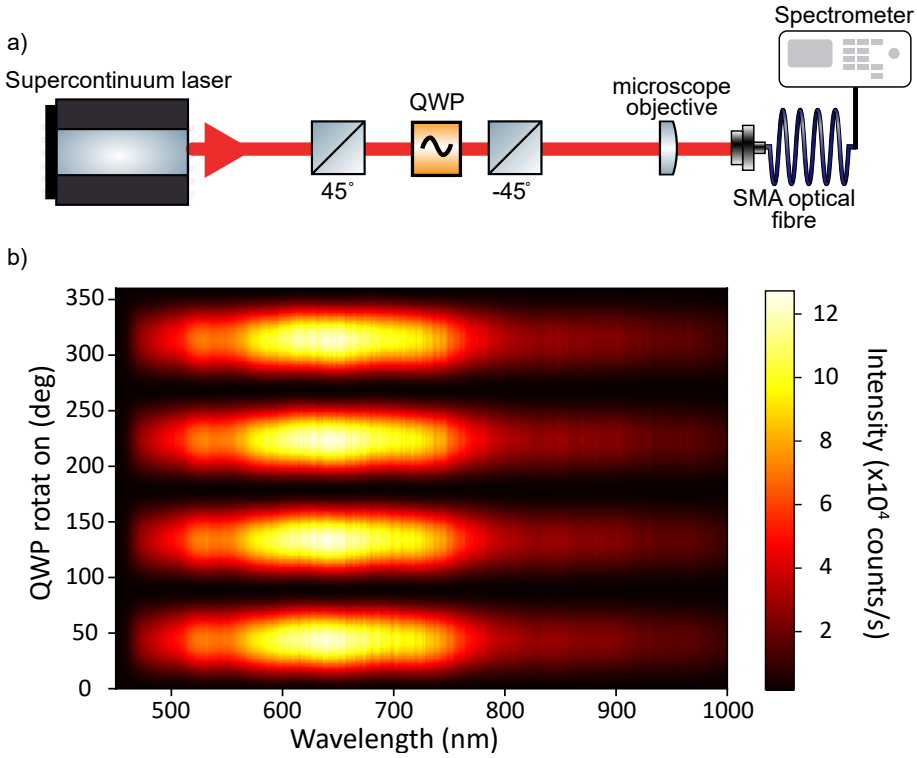

Figure 3.4: Quarter-waveplate performance test. In a), the setup used is schematically shown. The supercontinuum generates coherent white light which is linearly polarised at 45° relative to the optical axis of the QWP, which is automatically rotated. A second linear polariser is placed in the optical path following the QWP in a at −45° relative to the QWP's optical axis, i.e. the QWP is sandwiched between two polarisers. The transmitted light is detected by a microscope objective coupling the light into an optical fibre (200 μm diameter) which is connected to a spectrometer, recording the spectrum for a given QWP orientation. The QWP is fully rotated in steps of 5° and the collected spectra plotted as a heatmap with the QWP rotation against the wavelength in b); the colour-code corresponds to the intensity measured. A maximum transmission is expected when the light is fully circularly polarised. Hence, four peaks (with 90° separation) are expected. The spectrum also shows, that the spectral range chosen lies within the operational range of both the QWP and the microscope objective.

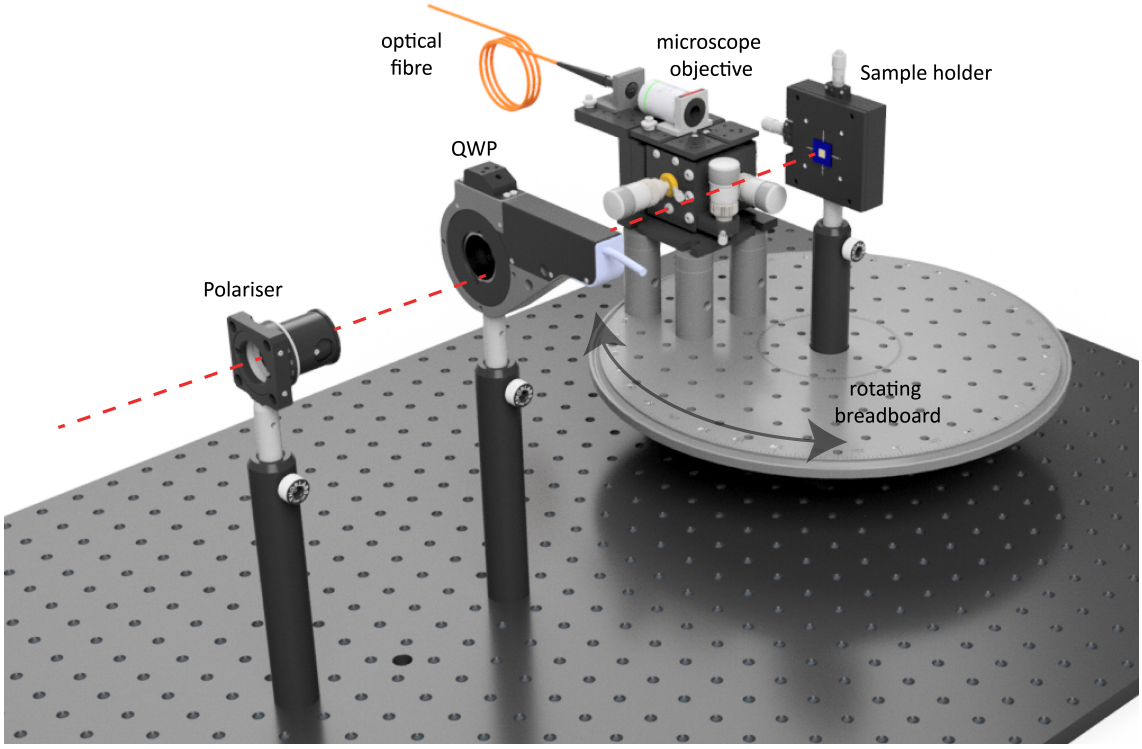

Figure 3.5: Experimental setup schematic of the circular intensity difference spectrometer. The polarisation is controlled with a linear polariser and a superachromatic QWP mounted in a motorised rotation stage. The light is incident on a nanograting mounted on an alignment disk which has been fitted with clamps to hold the nanograting in place. The alignment disk is fitted into an x-y-translation stage to fine-adjust the in-plane position. The alignment disk can be rotated in the thread to the necessary angle and fixed with a support-ring from the back. The diffracted light is focussed into an optical fibre with an 20x microscope objective mounted on a fibre launching stage. The fibre stage is itself mounted atop a motorised rotating breadboard which rotates around the central sample holder. The red dashed line indicates the path of the incident beam.

3.2 Summary and conclusion

In this chapter, the development of the experimental apparatus has been outlined. An initial design of the apparatus was aimed to mimic currently available commercial CD spectrometers (the Chirascan unit as been used as a reference) and presented measurements show good agreement. Both Jones calculus and Stokes analysis are used to describe the underlying physics involved and consequently, highlight the fundamental limitations of such a design.

In order to address the presented limiting factors, an improved version of the experimental apparatus is presented. The final version of the apparatus uses a supercontinuum fibre laser system and is fully automated, to achieve a broad spectral range and good repeatability. The optical equipment used in the apparatus is

presented and the broad detection range is demonstrated.

The experimental apparatus presented in this chapter has been used to study all nanogratings fabricated and the results of these studies will be presented in the following chapters.

Chapter 4

Circular intensity difference in higher-order diffraction beams from chiral quasiplanar nanostructures

The content of this chapter has been adapted from the published research article *"Circular Dichroism in higher-order diffraction beams from chiral quasiplanar nanostructures"*, C. Kuppe et al. [7]. The sample fabrication was done by Dr. C. Williams and Dr. T.D. Wilkinson. The sample characterisation with atomic force microscopy was performed by Dr. S.N. Gordeev and myself. J.T. Collins developed the automation for the diffraction spectroscopy. The numerical simulations were provided by Dr. J. You and Dr. N.C. Panoiu. The experiments were carried out by myself and supervised by Dr. V.K. Valev.

4.1 Introduction

Here, chiral metal nanostructures that exhibit large CID in the diffracted beams are investigated. For the chosen structures, the third-order diffraction beam gives the strongest CID response. This CID changes sign depending on wavelength. The results are validated by a good agreement between numerical and experimental data. Moreover, the robustness of the findings are validated by making use of Babinet's principle. In order to identify the origin of the effect, numerical simulations of the near-field are provided. These simulations show that for LCP and RCP beams, a difference in the electromagnetic response at the surface can be linked to the far-field CID.

The samples measured in this study were fabricated using electron-beam lithography (EBL) — a detailed description can be found in Section 2.3.5. In Figure 4.1a

the dimensions and depth profile are schematically shown. The gold U-shaped structures are 1 μm in length, have a separation of 200 nm and a highly sub-wavelength thickness. Each square unit cell consists of 4 U-shaped gold structures rotated by 90° with respect to each other. The dimensions of the actual fabricated nanostructures were established using atomic force microscopy (AFM) (Figure 4.1b) and scanning electron microscopy (SEM)(Figure 4.1c). The experimental setup for higher-order diffraction CID spectrometry is illustrated in Figure 4.1d. Here, a supercontinuum fibre laser source was used to provide 450-750 nm illumination. The polarisation state of the incident beam was controlled by a linear polariser and a quarter-waveplate. The sample was mounted normal to the plane of incidence and a collection optical fibre leading to a spectrometer was placed on a rotation stage, centred on the sample. Within this setup design only the horizontal-plane diffraction beams were measured, as indicated in the figure. The study encompassed up to 4 diffraction order beams (not including the zeroth-order beam), see Figure 4.1e. For the chosen samples, the fourth-order diffraction beam had the strongest intensity, as demonstrated both numerically and experimentally. The spatial distribution of the diffraction order beams followed the grating equation for diffraction, i.e. $\Lambda \sin\theta = n\lambda$, where Λ is the spatial period (equal to unit cell size 2.4 μm), θ represents the angle of diffraction, n is an integer number that defines the diffraction order and λ is the wavelength (see Section 2.3.2).

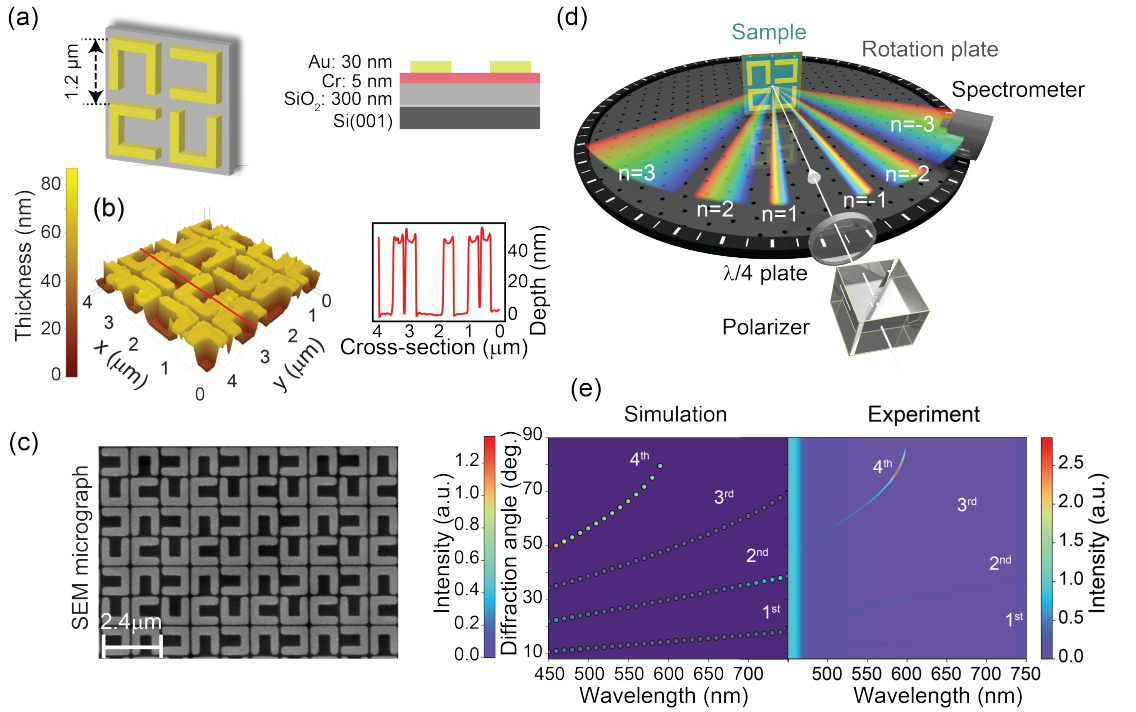

Figure 4.1: Panel (a) gives the schematic dimensions and depth of the U-shaped gold arrays and panel (b) shows the AFM image (left) and depth profile for the cross-section indicated by the red line across the AFM image. The SEM microscopic image of the array on a larger scale is shown in panel (c). In panel (d), the experimental setup of CID spectrometer is given. A supercontinuum fiber source with a range of 450-1050 nm is used. A quarter-waveplate selectively provides LCP and RCP light. As the detection is limited to the visible region, a short-pass filter (<750 nm) is used. The sample is positioned orthogonally to the angle of incidence and the detector is located on a rotation stage measuring the in-plane diffraction orders. In panel (e), the resulting intensities for RCP light are shown both numerically and from experiment, which are in very good agreement showing the diffraction order beams $n = 1 - 3$ as weak and a significantly stronger fourth-order beam. Adapted from [7].

Here, the normalised CID is defined as the difference over sum ratio, i.e. $CID = (I_{LCP} - I_{RCP}) / (I_{LCP} + I_{RCP})$, where I_{LCP} and I_{RCP} are the intensities measured for LCP and RCP, respectively [43, 111–113].

For consistency, both enantiomorphs are investigated, i.e. U-shaped and mirrored U-shaped structures, both numerically and experimentally, see Figure 4.2a to Figure 4.2d. For the simulations, the rigorous coupled-wave analysis (RCWA) method (see Section 2.3.7), implemented in Synopsis' RSoft DiffractMOD, a commercially available software was used. In this method, both the distribution of the dielectric constant and electromagnetic field are decomposed in Fourier series, the corresponding Fourier coefficients being computed using the boundary conditions at the top and bottom of the structure. These coefficients are subsequently used to calculate the optical near-field and the intensities of the diffracted beams. The

frequency dispersion of the permittivity of Au, Cr, and SiO2 have been fully incorporated in the presented simulations. Moreover, N=20 harmonics were used for each transverse dimension, which amounts to a total of $(2N + 1)^2 = 1681$ harmonics.

4.2 Results and discussion

Figure 4.2a shows a map of the numerical data, with the angle of each beam along the y-axis and the wavelength along the x-axis. The CID is visible as colour-coded values (red-blue) [103]. It is immediately obvious that the CID in the third-order diffracted beam dominates, with the first-, second- and fourth-orders exhibiting nearly no CID in comparison. Moreover, in the third-order, a characteristic bisignate (i.e. of two signs) CID is clearly apparent (see Section 2.1.5.3). A similar bisignate CID is also displayed in the experimental maps (Figure 4.2b). The difference is that in the experimental maps, the zero-CID crossing of the bisignate effect is blue-shifted. This difference can be attributed to fabrication imperfections, as compared to the idealized geometries in the numerical simulations [114–117]. Such imperfections can be seen in the AFM image and corresponding depth profile (Figure 4.1b). The imperfections are typically due to electron beam dosage during the EBL processes, or could occur during the lift-off procedure, for instance because resist remains attached to the corners of nanostructures.

Upon simulating and measuring the mirrored U-shaped nanostructures, similar results of opposite sign are obtained. Figure 4.2c shows the numerical data for the mirrored U-shaped nanostructures, where the bisignate CID is opposite (i.e. blue-red transition). This trend is confirmed by the experimental results presented in Figure 4.2d.

Moreover, in order to firmly establish the robustness of the results, Babinet's principle was investigated for the chosen geometries [118–121]. Figures 4.2e to 4.2h present numerical simulation data and experimental results from the complementary inverse U-shaped samples, i.e. U-shaped trenches within a continuous gold film. The data from these complementary structures unambiguously match those from the U-shaped nanostructures; bearing in mind that those are two sets of samples, with respective intrinsic imperfections. The difference in CID for the solid structures and their complementary trenches is also attributable to the thickness of the nanostructures. Indeed, Babinet's principle is only strictly valid for infinitely thin, ideal surfaces. Previous studies have established that the principle holds for samples of small finite thickness [122].

The maximum absolute values of the CID are as high as 80% for the simulations and 20% for the experiment. The difference in theoretical and measured yield is is extremely large and requires further examination. The numerical method used for

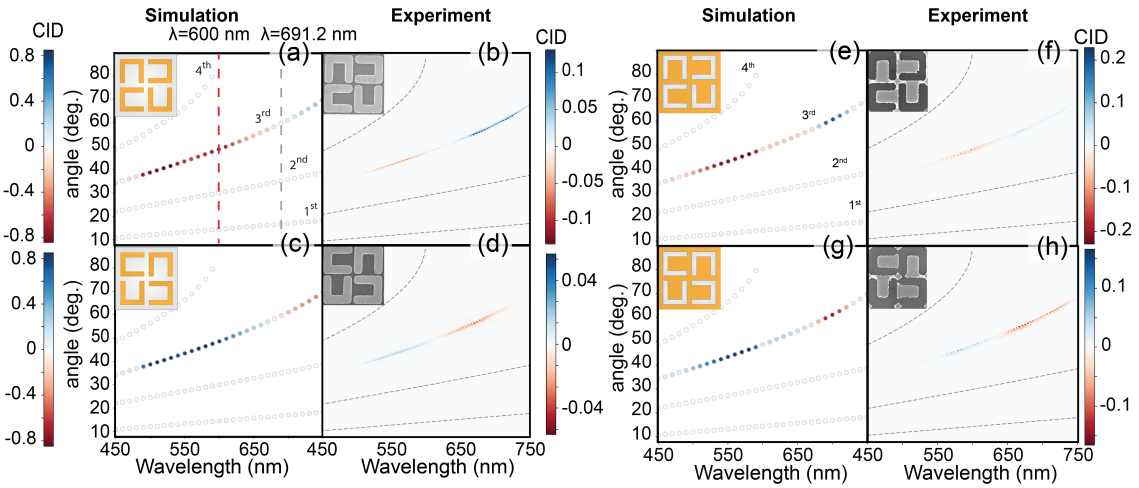

Figure 4.2: Comparison of experimental and numerical CID response for the third diffraction order beams for the U-shaped chiral arrays. Panels (a) and (b) show the numerical and experimental results for the U-shaped structures, respectively. The red dashed line in panel (a) represents the wavelength of maximum CID, while the gray dashed line marks the position of vanishing CID. In contrast, panels (c) and (d) show this effect for the opposite handedness. The insets show the schematic presentation used for the simulations and the SEMs for the experiments. The same analysis has been carried out for the complementary trenches, given in panels (e–h). The simulations clearly show that the third-order diffraction beam is the most dominant. Therefore, only the third-order diffraction beam is shown in the experimental graph, while the gray dashed lines indicate the position of the other diffraction beams. Further, upon inversing the structures, the results show that CID is invariant and validates the applicability of Babinet's principle. Numerical and experimental data are in good agreement. Adapted from [7].

the presented results is the rigorous coupled wave analysis (RCWA), which relies on solving a large matrix representing the wave equation of a given diffraction problem. To save computational resources, RCWA truncates the matrix, which can result in large inaccuracies. For this reason RCWA is mostly used for grating yielding a single diffraction order and might explain the large values calculated (see Section 2.3.7). In order to test this hypothesis, the numerical simulation was repeated with Lumerical [123], which uses the finite-difference-time-domain (FDTD) method. This method divides the simulation region into a fine mesh and solves Maxwell's equations at the mesh boundaries and nodes (see Section 2.3.7). The resulting CID response in all four diffraction orders are presented in Figure 4.3. As can be seen, the maximum value for the predicted CID is strongly reduced to 50% and much closer to the previously measured value.

The experimental results shown in Figure 4.2 were recorded before the setup was improved with respect to its optomechanics. Thicker rods to minimize the effect of vibrations, the new quarter-waveplate to reduce beam deviation and a change of the fibre used (as described in section 3.1.4) lead to major improvements in the sensitivity of the apparatus. As a consequence, all four diffraction orders could be measured and the CID response is also shown in Figure 4.3. The response in all four diffraction orders flips in sign upon reversing the nanograting pattern in the experiment as well as in the simulations. Experimental and numerical results are in very good agreement for both the sign in each order as well as the maximum value compared to the previous measurements.

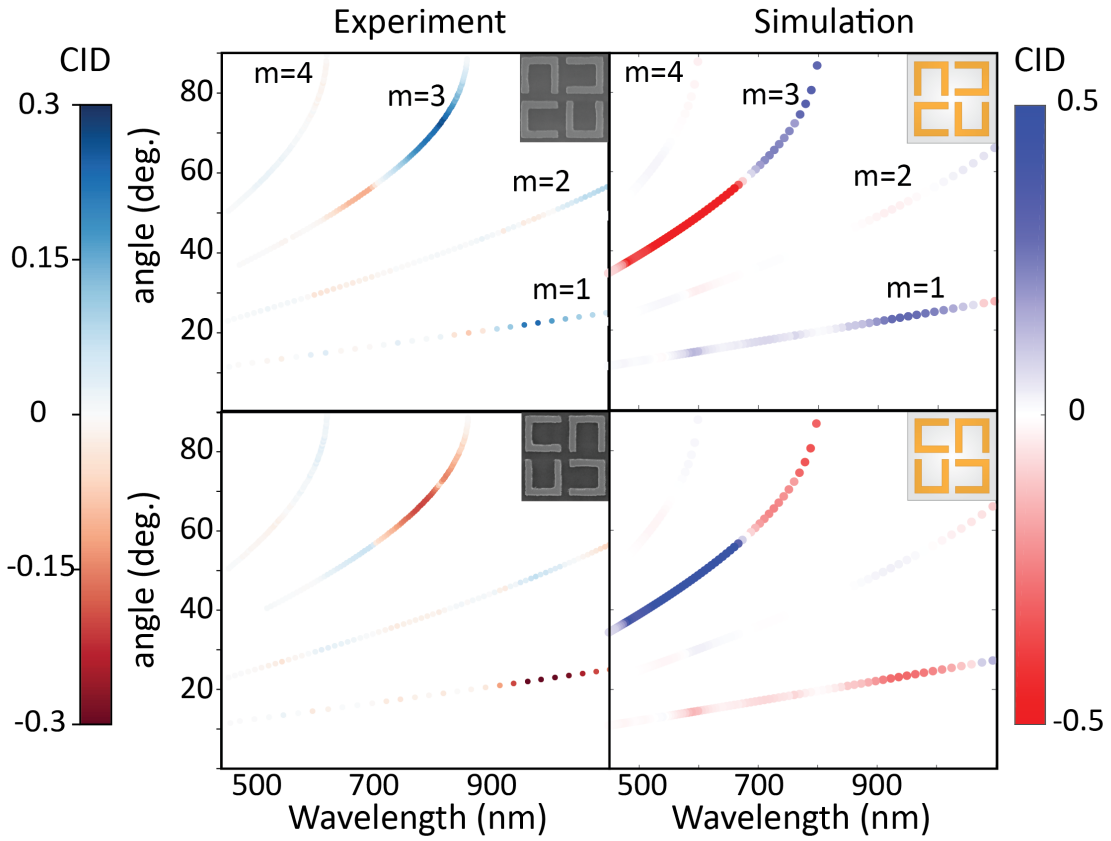

Figure 4.3: Data for U-shaped nanogratings after improving the optomechanical stability of the apparatus as outlined in section 3.1.4 and using the FDTD method for the simulations. The experimental results yield a higher maximum CID value as well as near-zero CID for the second and fourth order diffracted beam. Compared to the previous measurement a strong CID is observable for the first order diffracted beam as well. The numerical simulations based on FDTD yield very good agreement with the experimental results in all diffracted beams. The predicted absolute values are as high as 50% and much closer to the measured response.

A direct comparison between Figure 4.3 and Figure 4.1e demonstrates a difference between absolute intensity and CID of the diffracted light: while the diffracted intensity for circularly polarised light is strongest in the fourth-order, the CID is strongest in the third-order. A high absolute intensity for LCP and RCP light does not necessarily lead to a high normalised CID, following $CID = (I_{LCP} - I_{RCP})/(I_{LCP} + I_{RCP})$. Indeed, for a given absolute difference in intensity $\delta I = I_{LCP} - I_{RCP}$, CID would be larger if I_{LCP} and I_{RCP} are small.

The counter-intuitive intensity distribution that is shown in Figure 4.1e, does not follow the expectation from a common diffraction grating consisting of identical, regular and periodic point sources. As was discussed in Section 2.3.6, for feature sizes comparable to (or even smaller than) the wavelength of light the plasmonic hotspots are large compared to the wavelength. In this regime, the diffraction is governed by the shape and nature of a given unit cell. In order to describe the far-field

response Klimov's approach was discussed, which divides the unit cell into smaller units for which the electric near-field is calculated and subsequently propagated into the far-field. The numerical far-field results shown in Figure 4.2 therefore are a direct consequence of the near-field electric field distribution. Thus, to explore the origin of the chiroptical response measured,a rigorous Maxwell's equations solver in the frequency-domain was used. The results for the U-shaped nanostructures are displayed in Figure 4.4. The figure shows the colour-coded electric field intensity, at the surface of the nanostructures, upon illumination at 600 nm (Figure 4.4a) and 691.2 nm (Figure 4.4b). While the former corresponds to the maximum CID, the latter corresponds to the wavelength at which the CID vanishes. For both Figure 4.4a and 4.4b, the left and right panels show data for LCP and RCP illumination, respectively. It can immediately be seen that there is no single point source visible that could be assumed to dominate in the far-field projection, however the periodic field profile offers some insights. At 600 nm illumination, the heat maps show a clear change in the intensity pattern. This is most prominent in the central region of the unit cells, which have been magnified (top panels). The central region is also where chiral coupling occurs between the four achiral U-shaped nanostructures. Whereas the near-field intensity pattern in Figure 4.4a is chiral, that in Figure 4.4b is not. This behaviour translates directly into the far-field effects reported in Figure 4.2 when equations (2.77) and (2.78) are applied.

Using numerical simulations, the origin of the effects reported here have been identified. The solution is in agreement with other studies [36, 111, 124], both numerical and experimental, showing that chiral currents, and associated near-fields at the surface of both chiral and achiral structures play a major role for the chiroptical response.

4.3 Summary and conclusion

CID in higher-order diffraction beams has been demonstrated, enabling the clear differentiation between both enantiomorphs of quasiplanar, U-shaped nanostructures. Whereas previous studies limited themselves to the zeroth- or first-order diffraction [23, 125–130], it was here shown that, for the chosen samples, the third-order diffraction beam is the most dominant with respect to its chiroptical response. The CID was found to follow Babinet's principle. Furthermore, the advantages of the FDTD method compared with the RCWA to study the behaviour of the chosen nanogratings have been shown. In addition, chiral surface electric fields have been identified as the origin of the far-field chiroptical response. The chosen geometry allows a high degree of control over the polarisation conversion and spatial properties of light and it is spectrally tuneable. Further control will be allowed through

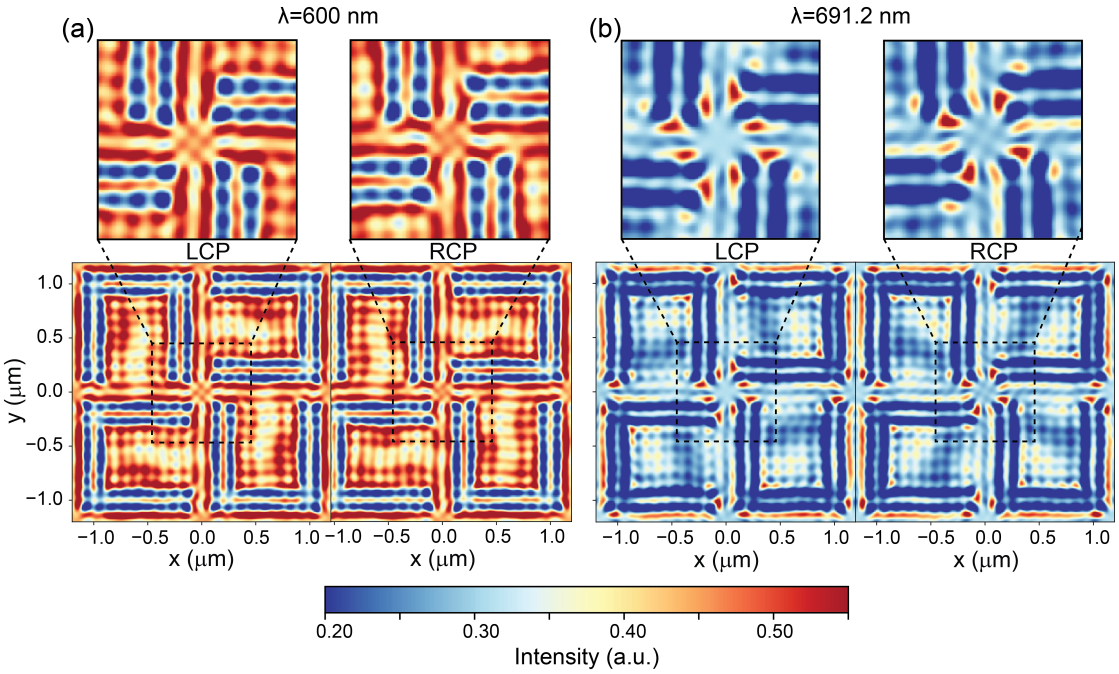

Figure 4.4: Near-field simulations at the surface of the samples illuminated with a) 600 nm giving maximum CID and b) 691.2 nm where the CID vanishes. The magnified central area is shown on top for each case, when illuminated with LCP (left) and RCP (right), respectively. We see a clear change in the normalised electric field intensity pattern in the central region, indicating that the source of the CID in the far-field originates from near-field sources. In particular, the optical near-field is strongly chiral in the case of maximum CID, whereas in the case when CID vanishes the profile of the optical near-field does not exhibit chirality. Adapted from [7].

manipulating the diffraction form factor of such systems. This can be achieved specifically by adjusting the lattice parameters, unit geometry and refractive indices of the metasurfaces. This study calls for future research focusing on the nature of near-field sources and how they can be designed to control the far-field response in diffraction experiments. It can also be envisioned that diffracted beams could be used for enhanced CID spectroscopy of molecules as well as other devices used for optical sensing.

Chapter 5

Measuring chirality in the far-field from a racemic nanomaterial: diffraction spectroscopy from plasmonic nanogratings

The content of this chapter has been adapted from the submitted research article *"Measuring chirality in the far-field from a racemic nanomaterial: diffraction spectroscopy from plasmonic nanogratings"*, by C. Kuppe et al. Dr. V.K. Valev and myself designed the research. Dr. C. Williams fabricated the nanograting samples and performed the SEM measurements. Dr. X. Zheng and Prof. G.A.E. Vandenbosch developed the theoretical model. Prof. S.N. Gordeev performed the AFM measurements. Dr. J.T. Collins developed the automation for the diffraction spectroscopy. I performed the diffraction spectroscopy. Dr. V.K. Valev and myself analysed the results. The reference to 'Supplementary notes' in the following section links to the supplementary information of the manuscript covering the mathematical derivation from Dr. X. Zheng and can be provided upon request if needed prior to the publication of the manuscript.

5.1 Introduction

Since the discovery of molecular chirality, optical activity (OA, see Section 2.1.5) has been used to measure the ratio of enantiomers (or enantiomeric excess). OA results from the difference in interaction between enantiomers with left- or right-hand circularly polarised light (CPL). Although OA is widely used in chemistry, the effect is typically very weak; this is because the chiral pitch of CPL is orders of magnitude larger than the chiral pitch in molecules [3]. Metal nanostructures bridge this gap. These nanostructures benefit from surface plasmon resonances (see

Section 2.2); whereby coherent oscillations of the surface electrons can be excited by visible light [131]. These oscillations occur at the same frequency, but with much shorter wavelength, which effectively confines light at the nanoscale and therefore enhances the interaction with molecules [37,128,132]. As a consequence, chiral plasmonic nanomaterials exhibit pronounced chiroptical effects, which can unfortunately overshadow the molecular response [91,126,133–135].

Although achiral plasmonic nanoparticles have been demonstrated to successfully enhance the chiroptical response of some molecules, such as cysteine and riboflavin [91,95], this effect is not optimal as it does not benefit from the chirality of the plasmonic fields. By contrast, a racemic mixture of chiral plasmonic nanostructures has no net OA, but strong local chirality in the plasmonic near-field, that chiral molecules can couple to. The response from such racemic nanomaterials can be highly sensitive to the enantiomeric excess of molecules [136]. However, the lack of chiroptical response in the far-field makes it difficult to tailor the material to molecules [137–139].

Here, for the first time, a detection scheme that allows the measurement of the chiroptical response of a racemic nanograting in the far-field is presented. It will be shown that racemic nanogratings can yield extremely large chiroptical responses of up to 15%, comparable to previously reported OA for chiral nanogratings [111,130, 134,140,141]. Previous work has focused on circular intensity difference spectroscopy from individual diffraction beams [7,111,130,134,140,141]. Here, a comprehensive analysis of up to four orders of diffraction is presented and the physical origin of the measured far-field response is explored by full-wave electromagnetic simulations. The measured far-field response is studied in the framework of a Green's function -– group-theory-based approach.

In Figure 5.1a, left- and right-circularly polarised (LCP and RCP) light is used to illuminate gold nanogratings. The spatial period of the nanogratings was chosen to produce multiple diffraction order beams in the visible spectrum. Those diffracted beams are analysed using circular intensity difference (CID) spectroscopy. The gold nanogratings studied in this work were fabricated using electron beam lithography on a silicon-silicon dioxide wafer (dioxide layer thickness of 300 nm). The gold layer (30 nm thickness) was stabilised using a chromium adhesion layer (3 nm thick). The thickness profile is presented schematically in Figure 5.1b and the fabrication details are given in the Methods section. The period of the gratings was set to 2.4 μm to generate multiple diffraction order beams in the visible region of the electromagnetic spectrum. Laterally, each square unit cell consists of an arrangement of gold elements and each element is 1 μm large. The nanograting width, and the nearest neighbour separation is 200 nm. Furthermore, each element is rotated by 90° with respect to its neighbour, in the clockwise direction. The individual nanoelements assemble

into three different chiral states – chiral (S-shaped elements), achiral (square-rings) and racemic (L's). Each enantiomorph of the S-shaped nanograting was fabricated twice (4 samples in total), for the square-shaped nanogratings three samples were made and for the L-shaped nanogratings another three samples were produced. The different gratings were characterised with scanning electron microscopy (SEM) and are shown in Figure 5.1c. The L-shaped elements naturally result in unit cells with opposite handedness (highlighted with cyan and yellow dashed lines, in Figure 5.1c) and are therefore macroscopically racemic. The racemic nanogratings were further characterised via atomic force microscopy (AFM) and the associated micrograph is presented in Figure 5.1d. On a larger scale, the good homogeneity of the total nanograting array (area 4 mm^2) is demonstrated by the good homogeneity in the photograph image shown in Figure 5.1e.

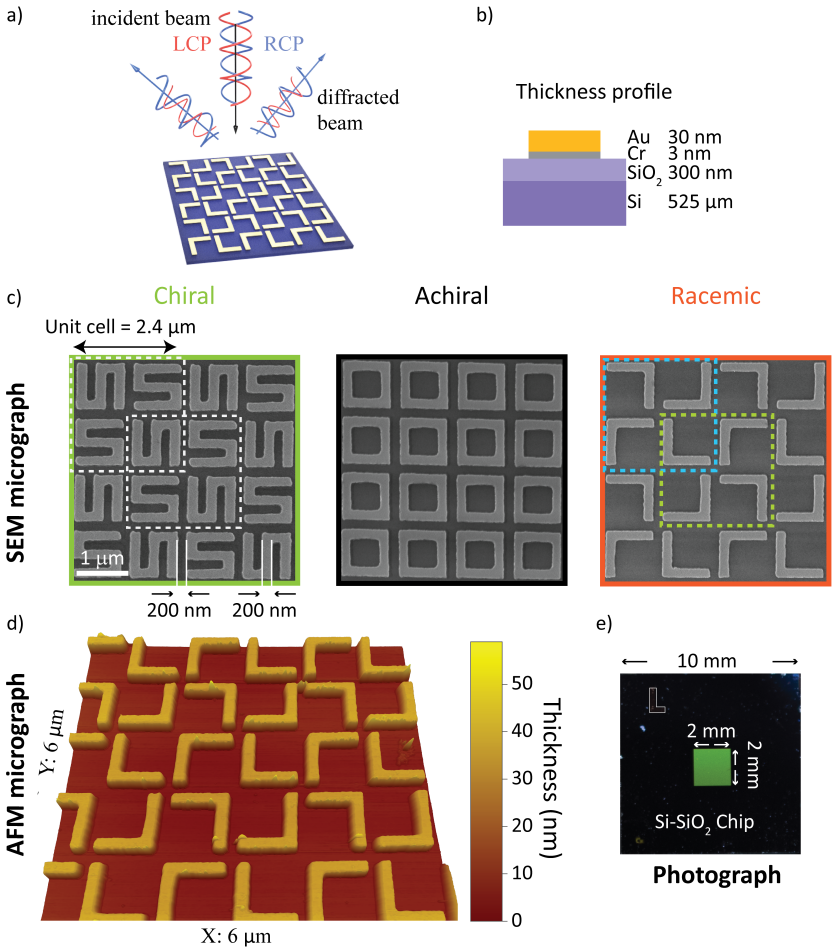

Figure 5.1: Nanomaterials can be chiral, achiral or racemic; here S-shaped, square-rings, and L-shaped, respectively. In a), the concept of circular intensity difference spectroscopy for individual diffraction order beams is presented schematically. Left- and right circularly polarised light beams (red and blue spirals respectively) are normally incident on a gold nanograting. The resulting diffraction orders are subsequently probed for differences in their intensity. The thickness profile of the nanogratings is shown in b). The central panel c), shows the scanning electron microscopy (SEM) micrographs of the resulting samples. The S-shaped chiral sample is shown in the green box. A unit cell consists of a 2x2 element matrix, where each element is rotated by 90° relative to its neighbour. The unit cell size is 2.4 μm and each element is 1 μm long, with an arm width of 200 nm and spacing of 200 nm. The achiral chip design (black box) is made of square-rings and the racemic chip (orange box) consists of L-shaped structures – the dimensions are the same as for the chiral nanograting. The cyan and green dashed lines in the racemic case indicate the two enantiomeric unit cells. In d), the results of a topographical study of the racemic nanograting via atomic force microscopy (AFM) are presented and its homogeneity over a large area (4 mm^2) is shown with a photograph in e).

The apparatus used to study the nanogratings is shown schematically in Figure 5.2a, with a detailed description in Section 3.1.4. A supercontinuum light source was used to generate coherent white light, with a linear polariser and an achromatic waveplate to control its polarisation state. Since all used nanogratings exhibit C4

symmetry (unchanged when rotated by 90° about its normal axis), the investigation was limited to the in-plane horizontal diffraction orders. Since these are the same on both sides of the incident beam, attention was focused on the positive diffracted order beams (m=1, 2 etc.), as indicated in Figure 5.2a. The diffracted light was measured with a light detection (LD) scheme, consisting of a microscope objective and an optical fibre connected to a spectrometer for analysis. For the individual nanogratings, the resulting diffraction patterns are shown in Figure 5.2b, 5.2c and 5.2d; presented as intensity heatmaps. The spatial distribution of the diffracted beams is in good agreement with the predicted spatial distribution from the grating equation (white lines) [7]. The effective period of the S- and square-ring-shaped nanogratings is halved to 1.2 μm as a consequence of the unit cell design shown in Figure 5.1c. While the normalised intensity for the L-shaped gratings produces four distinct diffraction orders (m=1 to 4), the first and third order beams are approximately 50 times less intense than the second and fourth order beams; barely visible in the intensity heatmaps.

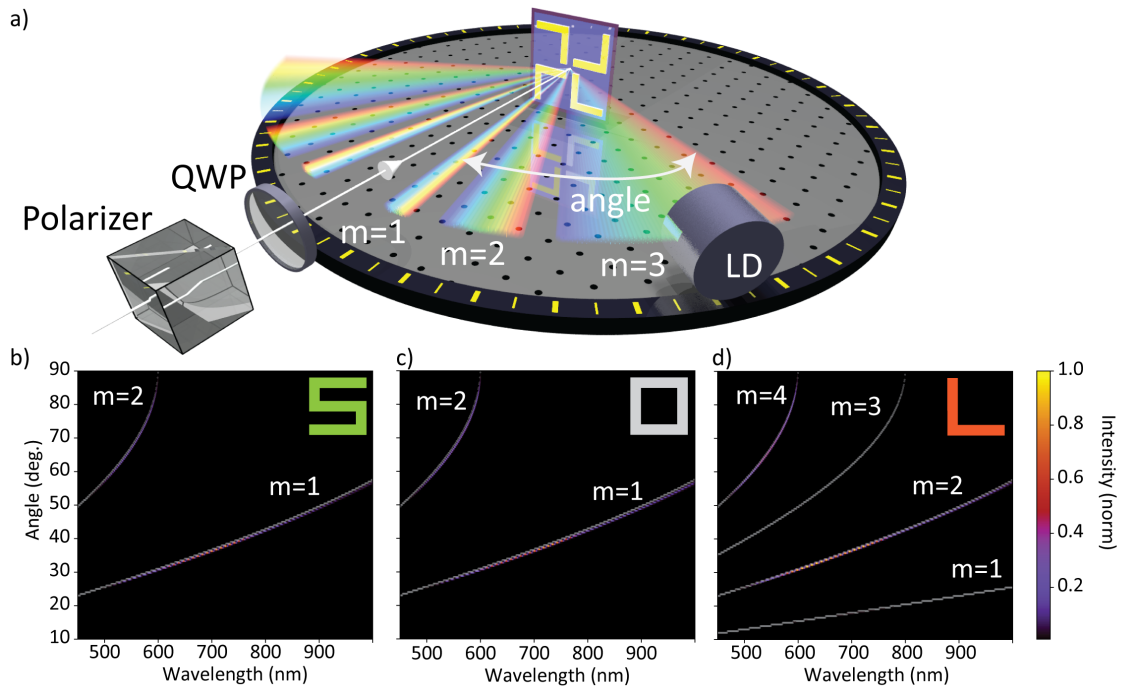

Figure 5.2: The nanogratings of chiral, achiral and racemic nanomaterials exhibit multiple diffraction beams in the visible part of the spectrum. The apparatus used to study the circular intensity difference (CID) in diffraction, and intensity pattern for each nanograting, is schematically shown in a). The polarisation state of the incident coherent white light was controlled by a linear polariser and a quarter-waveplate (QWP), the beam was directed at normal incidence with respect to the nanograting. The diffraction pattern in reflection was measured in the horizontal plane using a fibre-based light detection (LD) system rotated around the sample. Since the nanogratings exhibit C4 symmetry only the positive diffraction orders between 10–90° were measured. The resulting intensities for left-circularly polarised (LCP) light are shown on the right. The intensities for the samples, shown in Figure 5.1c, are represented by normalised heatmaps with the wavelength on the x- and the diffraction angle on the y-axis. The white lines show the predicted position of the diffracted order beams for periods of 1.2 μm (for S- and square-ring shaped samples) and 2.4 μm (for L-shaped samples) are given and agree with the experimental results.

The optical activity of the nanogratings was determined by measuring the CID in each diffraction order beam. CID is defined as

$$CID = \frac{I_{RCP} - I_{LCP}}{I_{RCP} + I_{LCP}}, \tag{5.1}$$

with I_{RCP} and I_{LCP} representing the measured intensities for RCP and LCP illumination, respectively.

Additionally, to corroborate the experimental results and further explain the physical origins of the observed effects, FDTD simulations were carried out using Lumerical [123]. In the simulations, the incident LCP and RCP plane waves are

generated by superposing two 90° phased plane waves which are linearly polarised along the x- and y-directions. All layers in the sample have been take into account. In detail, the Au layer is modelled by the material data from Johnson and Christy [142], the Cr layer and the Si layer is modelled by the material data from Palik [143] and the refractive index of the SiO2 layer is assumed to be 1.5 (small variations in this value had no effect on the results). It should be noted that instead of using the nominal thickness, the Au layer is assumed to be 50 nm. Two simulation regions are used. On the one hand, the FDTD simulation region is assumed to have periodic boundary conditions along the x- and y-directions and perfect matching layers (48 layers) along the z-direction. On the other hand, a mesh refinement region including both the Au and Cr layers is imposed to the S-shape structures, the L-shape structures, and the square-rings. The mesh steps along the x-, y- and z-directions are 10 nm, 10 nm and 1.5 nm, respectively.

5.2 Results and discussion

The measured and simulated far-field response of the nanogratings are presented in Figure 5.3. The results from the experimental and numerical analysis are in excellent agreement for both the spatial distribution as well as the CID response for each nanograting. The chiral S-shaped nanogratings (Figure 5.3a) exhibit a large CID of up to 20% and a change of sign between the first and second diffracted order beams. For the associated mirrored S-shaped nanogratings, the response is opposite in sign, as expected from chirality (see Figure 5.4 in appendix B.1). The results are in good agreement with the numerical simulations.

The achiral square-ring-shaped nanogratings (Figure 5.3b) should exhibit no CID and therefore, the measured response indicates the noise level in both the experiments and the numerical simulations. Experimentally, the maximum CID is just below 5%, which is significantly lower than the response obtained for the chiral nanogratings. For the simulations, the numerical noise level is as low as 10^{-7}. Sources for the experimental error are thought to be fabrication imperfections, detection uncertainties and small differences in the fibre coupling efficiency.

Unlike their microscopic counterparts, the racemic L-shaped nanogratings do exhibit CID. The experimental results (Figure 5.3c) demonstrate a large response of up to 15%, comparable to the S-shaped nanogratings with up to 20%. This counter-intuitive result is in good agreement with the numerical simulations, especially the strong responses in the first- and third-order diffracted beams. A slight spectral shift (red-shift) between the experimental and numerical results can be observed, due to the difference between the nominal sample geometry (ideally realised in a simulation) and the nanofabricated samples, prone to defects, see AFM micrograph

in Figure 5.1d. The robustness of the far-field response from the racemic L-shaped nanogratings was further investigated by measuring the effect of sample rotation with respect to the input beam. This investigation shows no significant net-effect on the observed results (see Figure 2 in appendix B.1).

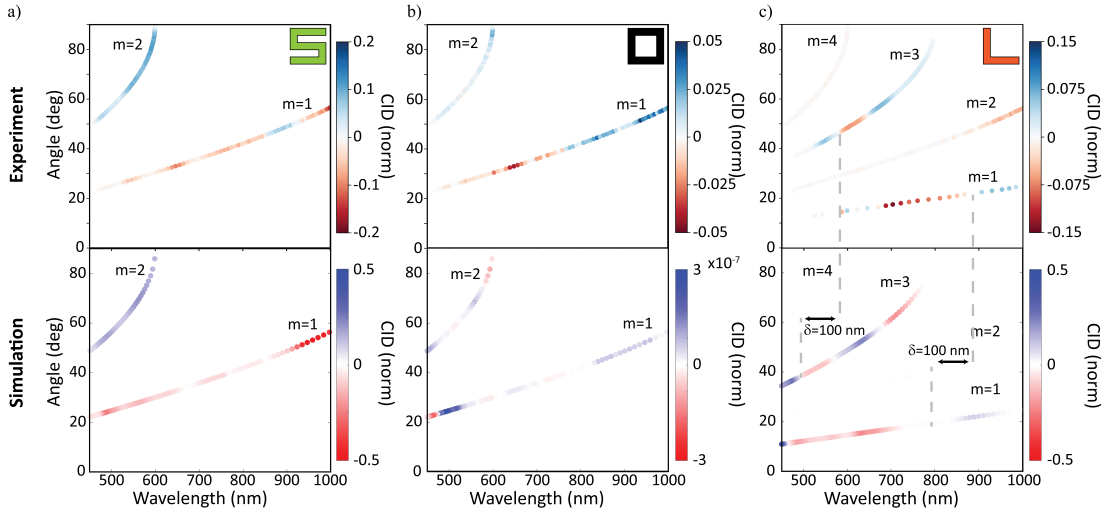

Figure 5.3: In diffraction, the response of the chosen racemic nanomaterials is similar to that of the chiral nanomaterials. The results for the circular intensity difference (CID) spectroscopy measurements for the three chiral cases – with chiral (green 'S'), achiral (black 'square-ring') and racemic (orange 'L'). The measured wavelength is shown on the x- and the diffraction angle on the y-axis. The diffracted order beams are numbered, and the colour represents the strength and sign of the measured CID signals. The experimental results (top row) are compared with numerical simulations (bottom row) and are in very good agreement. While the chiral and achiral cases agree with expectations, the racemic case, surprisingly, exhibits a CID comparable to the chiral case.

The robustness of the results from the S-shaped nanogratings was investigated by means of using the opposite enantiomorph. As expected the CID measured in the far-field should perfectly flip in sign and does so both experimentally and numerically (see Figure 5.4).

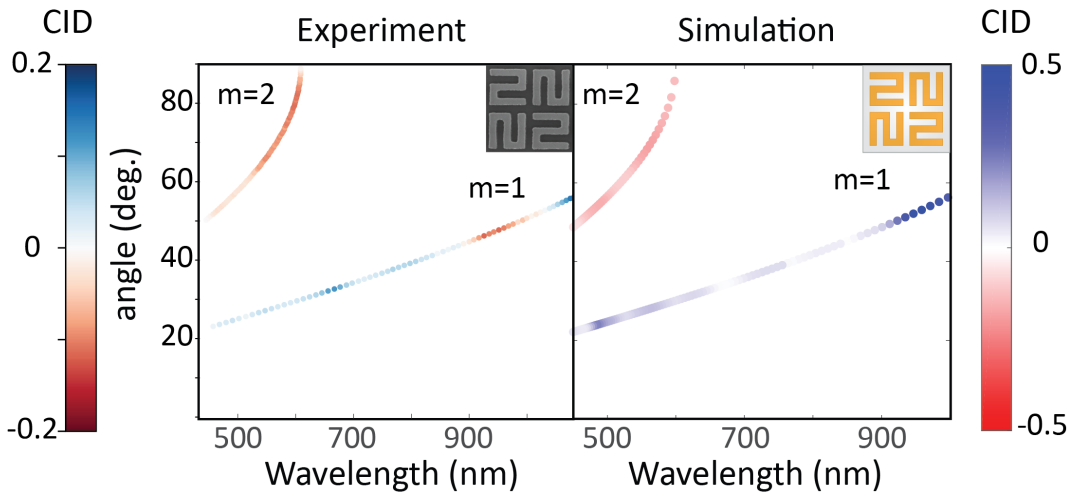

Figure 5.4: Diffraction data for mirrored S-shaped nanograting perfectly flips in sign in both experiment and simulation when compared to Figure 5.3a.

In order to explain the CID effects from the racemic L-shaped nanostructures, a near-field to far-field transformation procedure (see Supplementary Note 1) is employed. In the implementation, the near-field is first decomposed into propagating and non-propagating spatial Fourier modes with their Fourier coefficients being calculated. Then, all the modes are propagated and projected onto an observation plane so that physical quantities of interest, e.g. electromagnetic fields, power, etc., can be obtained. The reflectance spectrum from the racemic sample is identical under LCP and RCP illumination (see Figure 5.5a). This might seem surprising, given that the sample unit cells lack mirror symmetry. However, a careful examination of the sample reveals two additional axes of reflection that do not pass through the rotation centres of the unit cells (see Figure 5.5b). Mathematically, these mirroring symmetries together with the four-fold rotational symmetries form a D_4 point group. By further considering translational symmetries in the square lattice, the sample actually has *p4g* (wallpaper) symmetry [144]. Especially, due to the axes of reflection, the optical response due to the LCP and RCP illumination in the experiment can always be transformed into each other by a mirroring operation with respect to the axes of reflection (see Figure 5.5d). This transformation leads to a phase difference and results in an identical reflectance spectrum for the LCP and RCP excitation. The above statements have also been rigorously proven by using an integral equation representation [145–147] in combination with the group representation theory [148] (see Supplementary Notes 1 and 2). Additional numerical results for the effect of the gold and chromium layer thicknesses on the reflectance spectrum can be found in Figures 4 and 5 in appendix B.2.

In contrast to the reflectance spectrum which describes the effect of all the (propagating) Fourier modes, diffraction spectroscopy enables the precise examination of

the behaviour of each Fourier mode. Thus revealing the symmetry of the structure. As shown in Figure 5.5c, the calculated CID agrees well with the experimental data (Figure 5.3c).

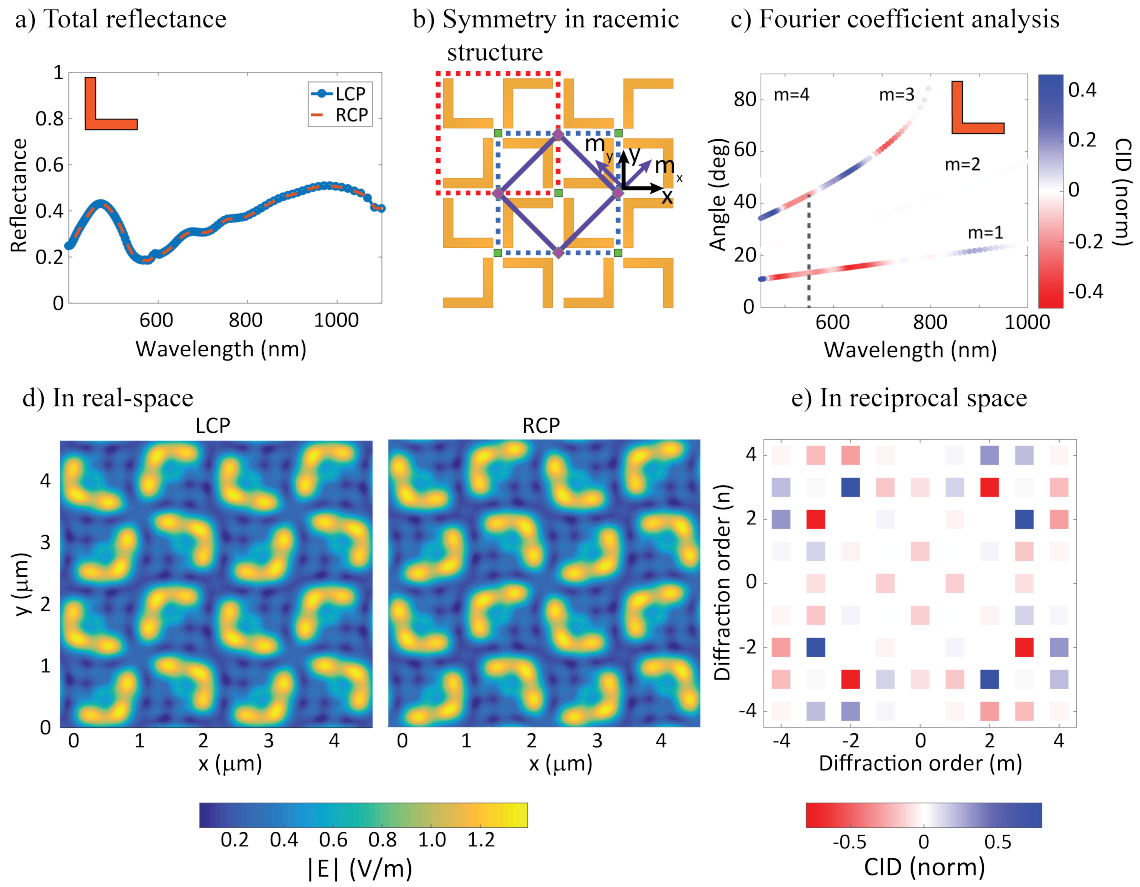

Figure 5.5: Fourier modal analysis reveals the effects of chirality on the measured response from the racemic nanomaterials. The total reflectance measured for the racemic sample is shown in a) for LCP (blue line) and RCP (orange line) – the two cases are identical and thus there is no CID. In b) the symmetry for the racemic nanostructure is schematically presented. The green squares represent the centres of rotation of the fourth order, while the purple diamonds represent the centres of rotation of the second order. Further, the solid purple lines represent two axes of reflection. The red and green dashed lines delineate the "normal" and "mirror" 4L unit cells, respectively. Lastly, two possible coordinate frames, that is, the x-y coordinate system and the m_x-m_y coordinate system, are marked by the black and purple colors. In c) the results of the Fourier coefficient analysis are shown and show that there is strong CID in individual diffraction orders, with the first and third diffraction orders showing the strongest CID. The dashed grey line at 554.2 nm indicates the wavelength studied further. In d) the total electric field magnitude measured using FDTD simulations at 3 μm above the surface at the indicated wavelength is shown. The result shows the summation of all propagating modes under LCP and RCP illumination respectively. The field maps can be projected into reciprocal space using a Fourier Transform, e). Each point corresponds to the diffraction order beams for the racemic structure for the same wavelength studied in d). The colour-code corresponds to the strength of the normalised CID response. The symmetry is preserved in the diffraction orders and the chiroptical response cancels if summed over all points.

Lastly, it should be pointed out that the square lattice supports only three wallpaper groups [144]: the *p4* group, which is generated by the C_4 point group and is exactly the case of the S-shape sample; the p4m group, which is generated by the D_4 point group, whose axes of reflection coincide with the rotational centres of the unit cells and which is exactly the case of the square-ring sample; and the p4g group which is the case of the L-shape sample. By following the same analysis for the L-shape structure, the CID features for the other two cases can be readily derived and are summarised in the Table 5.1. It is readily seen that reflectance and diffraction circular intensity difference spectroscopy in combination provide us with the powerful capability of identifying the symmetries of a unit cell in the square lattice, without having to analyse the intricate near-field.

	S-shape	L-shape	Square-ring-shape
Reflectance	✓	✗	✗
Diffraction	✓	✓	✗

Table 5.1: Summary of the CID features in the S-shape, L-shape and Square-ring-shape samples

5.3 Summary and conclusion

In summary, it was demonstrated that diffraction circular intensity spectroscopy can be used to measure a strong chiroptical response for racemic nanogratings. Chiroptical CID values of up to 15% have been achieved. The experimental findings are supported by a rigorous Fourier modal analysis. The analysis can identify the chiroptical response of each individual diffracted order beam. The observed chiroptical behaviour in the diffracted beams can be seen as a reciprocal to the extrinsic 2D chirality effect. Furthermore, the results enable the distinction of different unit cells (chiral, achiral and racemic) in a square lattice. The presented findings allow the tailoring of far-field features of racemic nanostructures to that of molecules, which is key for developing hyper-sensitive chiral molecular characterisation.

Chapter 6

Plasmonic nanogratings as a platform for enhanced molecular CID spectroscopy

The content of this chapter represents a summary of a proof-of-principle study to investigate the potential of racemic plasmonic nanogratings for enhanced molecular CID spectroscopy. Dr. V. K. Valev and myself designed the research. Dr. C. Williams fabricated the nanogratings. The chiral molecules were synthesised and provided by Dr. G. D. Pantoş and D. M. Răsădean. The deposition of the chiral molecules onto the nanogratings, the diffraction spectroscopy, the cleaning of the nanogratings and the data analysis were carried out by A. Murphy and myself.

6.1 Introduction

Faced with need for hyper-sensitive chiral sensing, as described in Section 2.1.1 for the case of pharmaceutical drugs, plasmonic nanostructures have shown great potential to act as a suitable platform [57, 149]. Recently, it was shown that especially achiral near-fields yield orders of magnitude more enhancement of the molecular CD than chiral near-fields [150]. The reason for this at first sight counter-intuitive finding has been attributed to an overshadowing of the molecular CD by that of the chiral structures. This overshadowing by chiral structures has subsequently led to an increased interest in racemic materials as a candidate combining advantages of both the achiral and chiral regimes (Chapter 5). A study published in 2018 [136], focused on the transmission of such racemic materials and showed enantioselective CD for both the *S*- and *R*-enantiomer of chiral molecules of up to 200 mdeg. The racemic structure in the study consisted of gold gammadion (also known as Swastika) arrays, with each gammadion being 275 nm in size. Three different gammadion arrays were compared – left-handed, right-handed and racemic. The results demonstrate that

the racemic array leads to a doubling of the enhancement of the molecular CD when compared to their chiral counterparts.

In this proof-of-principle study, the experimental apparatus and gold nanogratings presented in Chapter 5 were used to investigate the potential to detect chiral molecules. The achiral and racemic nanogratings (see Figure 5.1c) were covered with chiral molecules and their CID spectra measured.

The chiral molecule used for this study was the phthalocyanine derivative Si-Pc-(S/R)-(Naproxene)$_2$ (Pc-S and Pc-R respectively) – details on the synthesis and characterisation of Pc-S have been published by Răsădean et al. [151]. These phthalocyanines consist of a intrinsically achiral planar core disubstituted with the relevant naproxene enantiomer (either R or S). The ligands transfer their chiral information to the Pc core, giving chiral molecules with two (identical) chiral centres. The molecular structures of both enantiomers are schematically shown in Figure 6.1 a) and b). The corresponding CD spectra measured with the Chirascan are presented in Figure 6.1 c). Since this study focuses on the visible part of the electromagnetic spectrum, especially the CD peak at 683 nm is of interest.

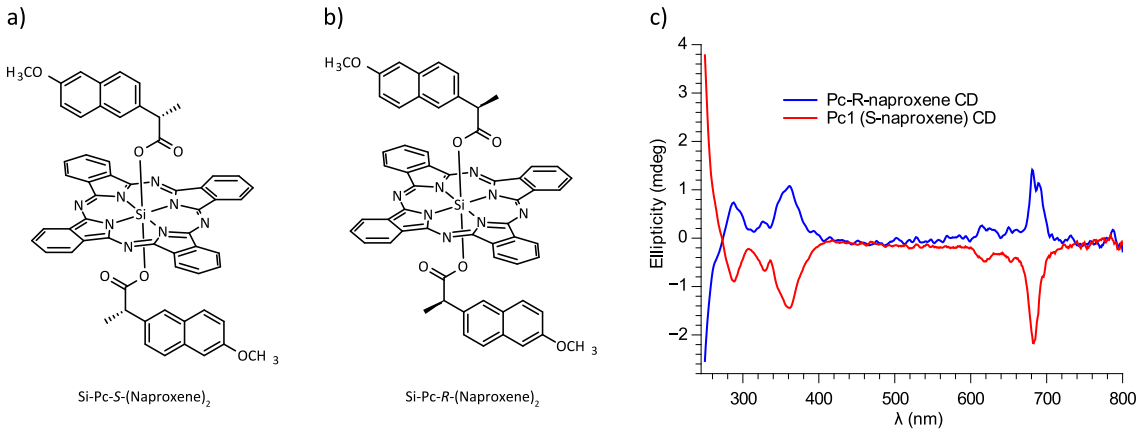

Figure 6.1: Chiral molecule used for the proof-of-principle study. In a), the molecular structure of the S-enantiomer is shown. The molecule consists of two symmetric chiral centres. The dashed and the solid wedges indicate structures coming forward out of the plane and going backwards into the plane respectively. The structure of the corresponding R-enantiomer is shown in b). The CD spectra recorded for both enantiomers dissolved in chloroform for a path length of 1 cm, recorded with Chirascan CD spectrometer for a molar concentration of 10^{-6} M is presented in c). Adapted from [151].

The Pc molecules were dissolved in Tetrachloroethane (TCE). TCE is a widely-used solvent in chemical studies and was chosen as a suitable solvent since it has similar properties as chloroform (which was previously used) but is less volatile and therefore is more promising candidate to produce homogeneous layers when spin-coated. For this work a molar concentration of 10^{-4} M was used.

The deposition onto the gratings was done by spin-coating (WS-400B-6NPP/

LITE, Laurell Technologies Corporation). The spin was set to 2000 rpm for 1 minute and the molecules were injected after the target spin-velocity was reached. For the molecule injection, a 50 μl syringe with a target volume of 10 μl was used. An example of the produced layers (photograph and microscope image) can be found in Figure 6.2. The diffraction spectroscopy setup was the same as described in Section 3.1.4. After each measurement the nanogratings were cleaned using three successive baths in chloroform for 1 minute each and a sonicator (Ultrasonic bath XUBA1, Grant).

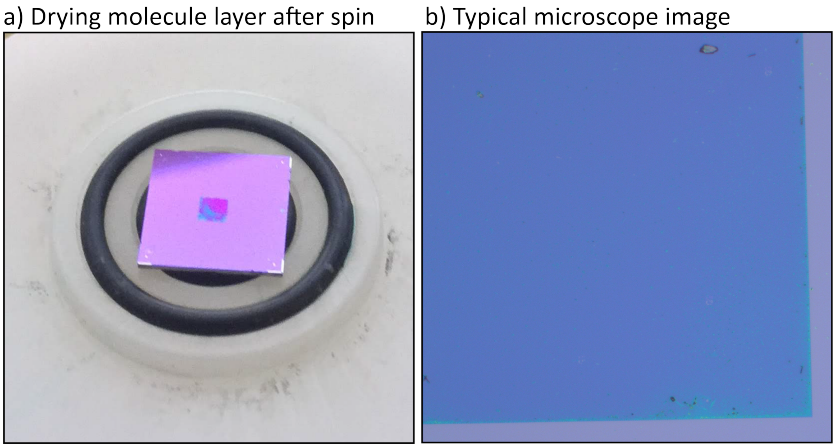

Figure 6.2: In a), a photograph image of the nanograting after the spin-coating deposition of Pc molecules is shown. Some residual solvent is still drying, causing the blue tinge at the bottom-left corner of the gold array. In b), a microscope image of the Pc layer on the grating recorded with a Zeiss microscope with a 5x microscope objective is shown. The dark blue tinge shows the coverage of the nanograting area. An accumulation of the molecule can be observed in the bottom-right corner observable as a lighter colouring. Close examination shows that small clusters with the same colour are distributed over the grating area.

6.2 Results

The results from the achiral (square-ring) nanogratings are shown in Figure 6.3. The CID of the uncovered nanograting is compared to the two enantiomers' CID in the first-order diffracted beam. The first-order beam was chosen for this study since it is the only one covering the spectral range of interest (see Chapter 5 for a detailed description of the diffraction pattern). The magnitude of the CID is very small with a maximum of 3%. This low magnitude agrees with the expectation, since the achiral nanograting should not yield a measurable CID. The responses of the chiral molecules mostly follow that of the nanograting.

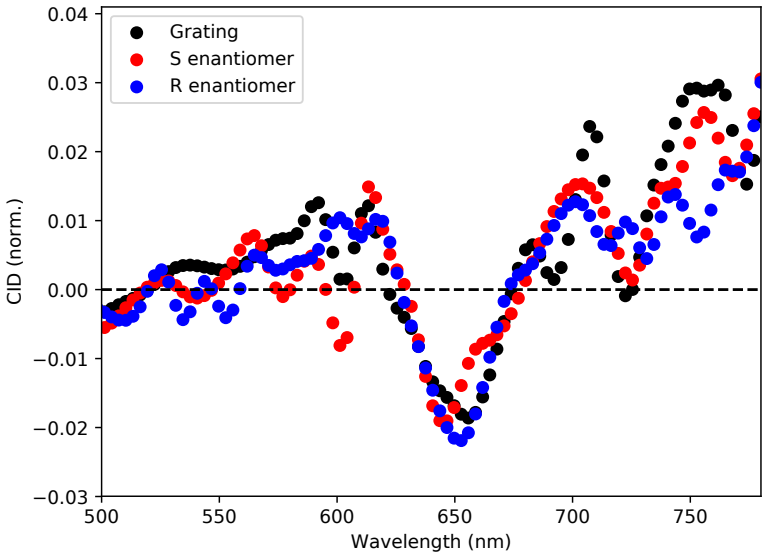

Figure 6.3: Achiral nanograting for enantiomeric sensing in the first diffracted order beam. The CID is plotted against the wavelength for the uncovered nanograting (black); and the nanograting covered with the *S*-enantiomer (red) and the *R*-enantiomer (blue) respectively.

In Figure 6.4, the results for the racemic nanograting are presented. The response of the uncovered racemic nanograting was used as a reference – the third-order diffracted beam was used for this study, since it showed the strongest sensitivity to the presence of the Pc molecules. The reproducibility was investigated by repeating the following procedure three times for each enantiomer: deposit molecule (spin-coat), measure with apparatus and clean. The averaged responses with their associated standard error are shown in Figure 6.4a. In contrast to the spectra of the achiral nanograting, a clear difference in the CID spectrum can be observed which is directly attributed to the enantiomer used. The maximum CID value for the uncovered nanograting is similar the achiral nanograting's CID with 5%. However, the covered nanogratings reach maximum values twice as high. The standard error is mainly due to the different molecule layer thicknesses in each measurement. This enantioselective behaviour is even more apparent when the normalised responses are considered (Figure 6.4bi). The maximum value is approximately 22 times higher than the nanograting's maximum value at 640 nm.

The difference plot in Figure 6.4bii shows a strong reversal of the sign in the CID depending on the enantiomer with near-identical magnitudes. Interestingly, in this case there is a smaller secondary peak at 683 nm which is at the same wavelength as the peak measured, using the Chirascan, for the dissolved molecules at a lower concentration as seen in Figure 6.1.

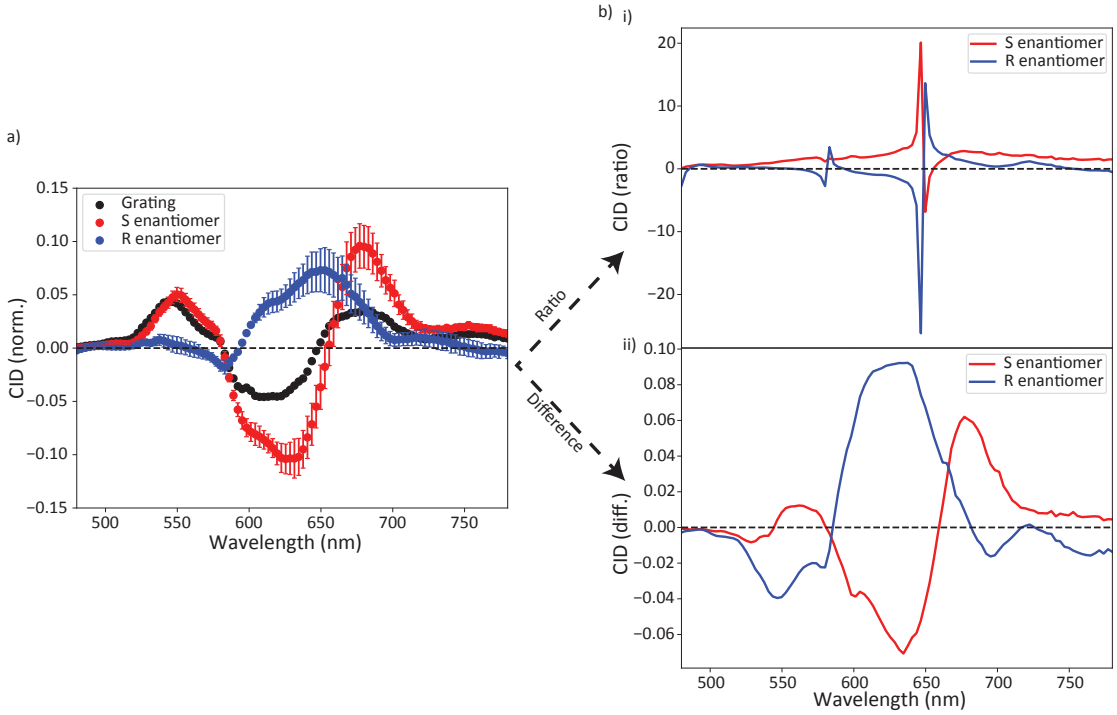

Figure 6.4: Racemic nanograting for enantiomeric sensing. In a), the CID is plotted against the wavelength for the uncovered nanograting (black), the S-enantiomer (red) and the R-enantiomer (blue). The measurements for the S- and R-enantiomers were repeated three times each and the average used for this graph – the error bars correspond to the standard error associated with the averaging. In b), the response of the enantiomers is presented in the normalised form; the ratio in i) and the difference in ii) of covered to uncovered and covered nanograting responses. All graphs show a clear opposite in the enantiomeric response covering the complete spectral range a). The most dominant peak occurs at 650 nm and clearly shows an opposite behaviour associated with the molecular coverage. In the difference plot ii), this opposite behaviour is observable over the complete spectral area.

In Figure 6.5, the results for the enantiomeric excess investigation are shown. Here, the results presented in Figure 6.4 are compared to the responses measured for layers consisting of a mixture of both enantiomers. For this study, three mixtures were used – 75%:25% (R:S), a racemic mixture and 25%:75% (R:S). When studying the response from the racemic mixture, a clear affinity towards the R-enantiomer can be observed. In contrast, for the case of both mixtures consisting three parts more of one enantiomer than the other, the responses correspond closely to the responses of their pure counterparts. While the magnitudes of the responses are different (weaker for the 75% R and stronger for 75% S when compared to the pure responses), the overall trend agrees well with the expectation. The differences in magnitude have also been observed for the pure enantiomer layers which led to the standard error shown in Figure 6.4.

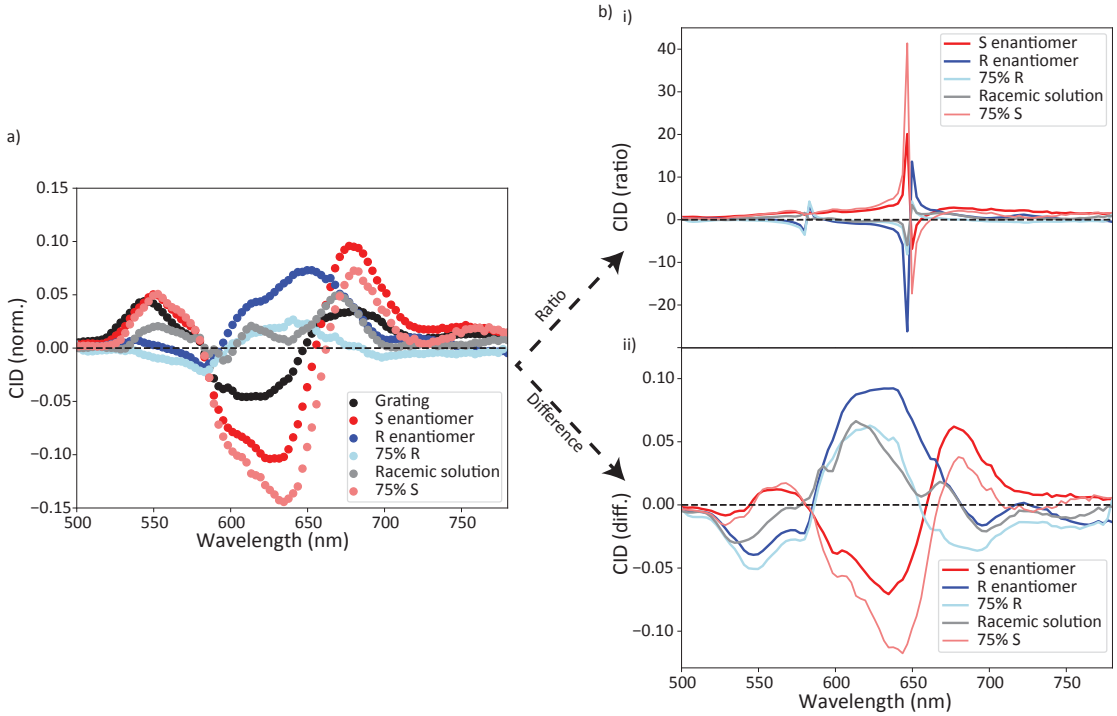

Figure 6.5: Enantiomeric excess study on the racemic nanograting. In a), the responses of the uncovered nanograting (black), *S*- (red) and *R*-enantiomer (blue), a racemic mixture of the solution (grey), as well as a 75%-25% mixture for each enantiomer respectively (light blue and red) are compared. The responses of the mixtures is strongly tending towards the corresponding pure states and therefore allow for the determination of the dominant enantiomer. The racemic response shows a strong affinity towards the *R*-enantiomer. The normalisation plots in b) show this effect clearly.

6.3 Discussion

Although all Pc solutions have been deposited on the nanogratings with the same spin-coating recipe and sample volume, it was difficult to achieve optimal repeatability. The differences with respect to layer quality and thickness are attributable to the exact volume used, and therefore subject to errors associated with the syringe, as well as systematic errors associated with the preparation of the solutions. It was also found that the height and angle used for injection can have a strong influence on the produced layer. A more repeatable injection procedure could therefore improve the molecule deposition. For this reason, simple drop casting was tested in the very beginning of this study but rejected based on the extremely inhomogeneous resulting drying patterns (Figure 6.6). In addition, it was observed that the design of the racemic nanograting favoured the aggregation of solution between the L-shaped nanostructures, which could be due to the fact that these nanogratings offer the largest surface area between gold elements compared to the square-ring

nanogratings.

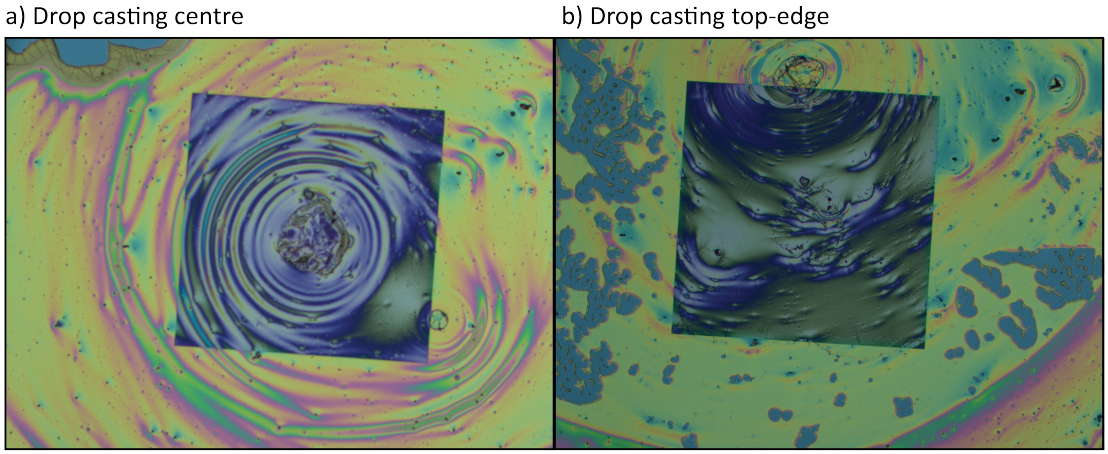

Figure 6.6: Microscope images of helicenes dissolved in chloroform deposited on the nanograting via drop casting. In a), the syringe was situated just over the centre of the nanograting, resulting in a centrosymmetric drying pattern around that point. In b), the syringe was situated at the top-edge of the nanograting. The drying patterns in both cases prevent the forming of a homogeneous layer and were therefore not chosen as the appropriate technique.

Once a good layer quality can be achieved repeatably, it will be interesting to determine the thickness of the layer and use it to estimate the number of molecules illuminated by the light. Such an estimate would allow to meaningfully compare different techniques with respect to their enhancements and sensitivities. Another approach could be to spin-coat the molecules onto treated quartz glass. The spectra measured from the covered quartz glass and from the covered nanostructures are subsequently compared. Such an approach has been used in the study mentioned in the introduction to establish the enhancement of the molecular CD by gold gammadion arrays [136].

In addition to the surface homogeneity, the solutions were prone to aggregation at the concentration used. An example of a strongly aggregated molecule solution spin-coated onto the nanograting, can be found in Appendix C, Figure 6.

Another factor is the sensitivity associated with the diffracted order beam. Interestingly, for the racemic case, it is the third-order diffracted beam that seems the most suitable to enhance the molecular CID. As described in Chapter 4, this could be explained by the fact that the CID is based on an absolute difference in light intensities measured for RCP and LCP; and therefore yield greater CID in less intense diffracted order beams. However, similar to Chapter 5, a numerical model could prove beneficial for more insight but was outside the scope of this thesis.

In order to test the applicability of the racemic nanogratings, it would be interesting to test other chiral molecules consisting of multiple chiral centres and thus

perhaps conflicting supra-structural CD. Furthermore, the results suggest the possibility to distinguish opposite enantiomers at wavelengths away from the absorption wavelength, as noticeable differences were observed in the whole spectral range of 480-780 nm. If off-absorption wavelengths can be used as well, this could be of interest to study molecules with absorption peaks in the UV, which is the case for many biomolecules [36].

6.4 Summary and conclusion

In this proof-of-principle study, the potential use of the developed apparatus and the nanogratings for the sensing of chiral molecules was investigated. The chiral molecules were spin-coated onto achiral and racemic nanogratings. The results show no enhancement of the CID response from the molecules when coated onto the achiral nanogratings. In contrast, when coated onto the racemic nanograting the observed responses are clearly distinguishable and up to 22 times stronger than the response of the uncovered nanograting. Furthermore, the responses from the chiral molecules seem to follow an opposite trend and hence allow to differentiate the two enantiomers. Additionally, it was shown that 75%:25% mixtures of the two enantiomers also yielded distinctive responses attributed to the respective dominant enantiomer presented. The results show the potential of the apparatus and nanogratings for chiral sensing applications.

Chapter 7

Conclusion

The measurement of chiroptical effects of chiral molecules is a highly active area of research due to the fact that the associated responses are typically very weak. The use of plasmonic nanostructures has sparked great interest in this regard, since such nanostructures enable the concentration of electromagnetic fields which can be used to greatly enhance the chiroptical response of chiral molecules. However, chiral nanostructures yield chiroptical effects themselves while the spectral response from achiral as well as racemic nanostructures cannot be tuned to that of the molecules. Thus, it has been difficult to find a satisfactory solution. In order to address this predicament, circular intensity difference (CID) spectroscopy in diffraction has been suggested as a promising candidate offering a more sensitive characterisation technique. However, previous research in this direction had been limited to the first-order diffracted beam and an explanation of the advantages of this technique remained elusive.

This thesis helps to bridge this research gap. First, the theoretical concepts of chirality (Section 2.1), plasmonics (Section 2.2) and diffractive optics (Section 2.3) have been introduced. Subsequently, a commercially available CD spectrometer has been studied in Chapter 3.1.4 and its advantages and limitations with regard to various sample media were discussed. Based on the presented findings, an experimental apparatus has been developed that allows the measurement of linear chiroptical effects for a wide range of samples (diffractive and non-diffractive) necessitating only minor changes, such as choosing the appropriate sample holder (i.e. cuvette holder or grating holder). The results obtained with the developed apparatus agree well with those of the commercial system. The discussion of photoelastic modulators and quarter-waveplates for the polarisation control has been based on Jones calculus (Section 3.1.2.1) and Stokes' analysis (Section 3.1.2.2); and a waveplate was consequently used in the apparatus. Following the description of the final apparatus, the nanofabrication technique used to produce the nanogratings for this thesis has been outlined in Section 2.3.5.

Subsequently, the main research contributions were presented in three chapters. In Chapter 4, a published proof-of-principle study demonstrating the potential of higher-order diffracted beams for diffraction CID spectroscopy for a chiral nanograting was presented. The study's findings illustrate that diffraction spectroscopy in such nanogratings can yield extremely large CID values (up to 20%), offer spectrally-tunable polarisation conversion and up to four diffracted order beams with different spectral features.

In Chapter 5, the findings of the proof-of-principle study were used as a foundation for a rigorous geometrical study of achiral, chiral and racemic nanogratings. The presented results establish CID spectroscopy in diffracted order beams as a broadly-applicable sensing technique. Especially the findings with respect to the racemic nanograting are promising since such nanogratings typically yield no chiroptical response in the far-field and therefore cannot be designed to optimally enhance the molecular CID. However, using CID spectroscopy in diffraction allows to unveil the chirality of such nanostructures and for the first time provides a technique to access the far-field behaviour of racemic nanostructures. The results are supported by a Fourier modal analysis that pinpoints the physical origin of the chiroptical responses measured. Furthermore, the developed theoretical model can be used to predict both the near- and far-field responses, decomposed into the respective Fourier components, for a chosen nanograting design. This tool is therefore useful to design nanogratings with spectral features specifically tailored to that of molecules, allowing the hyper-sensitive measurement of molecular chiroptical effects.

Chapter 6 presents the results of a proof-of-principle study investigating the potential of the developed apparatus and achiral as well as racemic nanogratings, as studied in Chapter 5, to measure the chirality in molecules. Here, specifically synthesised chiral molecules with strong absorption in the visible part of the electromagnetic spectrum have been spin-coated onto the plasmonic nanogratings. The achiral nanograting shows no enhancement of the molecular chiroptical response. In contrast, the observed responses of the covered racemic nanograting yield distinguishable enantioselective behaviour – allowing to differentiate the chirality in the created molecular layers. Furthermore, the results demonstrate that similar responses can be observed for mixtures of both enantiomers.

The field of nanophotonics has led to a great variety of specifically tailored linear and nonlinear optical characterisation techniques in the past. The promise of CID spectroscopy in diffracted order beams will certainly prove to be a valuable addition to these tools and help to advance today's capabilities to design and characterise chiral materials.

References

[1] J. T. Collins, C. Kuppe, D. C. Hooper, C. Sibilia, M. Centini, and V. K. Valev, "Chirality and Chiroptical Effects in Metal Nanostructures: Fundamentals and Current Trends," *Advanced Optical Materials*, vol. 5, no. 16, p. 1700182, 2017.

[2] D. B. Amabilino, *Chirality at the Nanoscale*. Weinheim, Germany: Wiley-VCH Verlag GmbH & Co. KGaA, 2009.

[3] V. K. Valev, J. J. Baumberg, C. Sibilia, and T. Verbiest, "Chirality and Chiroptical Effects in Plasmonic Nanostructures: Fundamentals, Recent Progress, and Outlook," *Advanced Materials*, vol. 25, no. 18, pp. 2517–2534, 2013.

[4] M. Schäferling, D. Dregely, M. Hentschel, and H. Giessen, "Tailoring enhanced optical chirality: Design principles for chiral plasmonic nanostructures," *Physical Review X*, vol. 2, no. 3, pp. 1–9, 2012.

[5] N. A. Abdulrahman, Z. Fan, T. Tonooka, S. M. Kelly, N. Gadegaard, E. Hendry, A. O. Govorov, and M. Kadodwala, "Induced chirality through electromagnetic coupling between chiral molecular layers and plasmonic nanostructures," *Nano Letters*, vol. 12, no. 2, pp. 977–983, 2012.

[6] T. Wu, J. Ren, R. Wang, and X. Zhang, "Competition of chiroptical effect caused by nanostructure and chiral molecules," *Journal of Physical Chemistry C*, vol. 118, no. 35, pp. 20529–20537, 2014.

[7] C. Kuppe, C. Williams, J. You, J. Collins, S. Gordeev, T. Wilkinson, N.-C. Panoiu, and V. Valev, "Circular Dichroism in Higher-Order Diffraction Beams from Chiral Quasiplanar Nanostructures," *Advanced Optical Materials*, vol. 1800098, pp. 1–6, 2018.

[8] A. L. Nafie, *Applications of Vibrational Optical Activity*, vol. 492. Chichester, UK: John Wiley & Sons, Ltd, 2011.

[9] W. Kelvin, "Baltimore lectures on molecular dynamics and the wave theory of light," 1904.

[10] R. W. Smithells and C. G. Newman, "Recognition of thalidomide defects.," *Journal of Medical Genetics*, vol. 29, no. 10, pp. 716–723, 1992.

[11] T. Eriksson, S. Björkman, B. Roth, Å. Fyge, and P. Höuglund, "Stereospecific determination, chiral inversion in vitro and pharmacokinetics in humans of the enantiomers of thalidomide," *Chirality*, vol. 7, no. 1, pp. 44–52, 1995.

[12] T. Mori, T. Ito, S. Liu, H. Ando, S. Sakamoto, Y. Yamaguchi, E. Tokunaga, N. Shibata, H. Handa, and T. Hakoshima, "Structural basis of thalidomide enantiomer binding to cereblon," *Scientific Reports*, vol. 8, no. 1, p. 1294, 2018.

[13] R. Noyori, "Asymmetric Catalysis: Science and Opportunities (Nobel Lecture) Copyright© The Nobel Foundation 2002.," *Angewandte Chemie International Edition*, vol. 41, no. 12, p. 2008, 2002.

[14] G. Subramanian, ed., *Chiral Separation Techniques*. Weinheim, Germany: Wiley-VCH Verlag GmbH & Co. KGaA, 2006.

[15] G. Nair, H. J. Singh, D. Paria, M. Venkatapathi, and A. Ghosh, "Plasmonic interactions at close proximity in chiral geometries: Route toward broadband chiroptical response and giant enantiomeric sensitivity," *The Journal of Physical Chemistry C*, vol. 118, no. 9, pp. 4991–4997, 2014.

[16] J. A. Schuller, E. S. Barnard, W. Cai, Y. C. Jun, J. S. White, and M. L. Brongersma, "Plasmonics for extreme light concentration and manipulation," *Nature Materials*, vol. 9, no. 3, pp. 193–204, 2010.

[17] M. H. Alizadeh and B. M. Reinhard, "Plasmonically enhanced chiral optical fields and forces in achiral split ring resonators," *ACS Photonics*, vol. 2, no. 3, pp. 361–368, 2015.

[18] Y. Liu, W. Zhao, Y. Ji, R.-Y. Wang, X. Wu, and X. D. Zhang, "Strong superchiral field in hot spots and its interaction with chiral molecules," *EPL (Europhysics Letters)*, vol. 110, no. 1, p. 17008, 2015.

[19] T. Cao, C. Wei, L. Mao, and Y. Li, "Extrinsic 2D chirality: giant circular conversion dichroism from a metal-dielectric-metal square array," *Scientific Reports*, vol. 4, p. 7442, 2014.

[20] L. Hu, Y. Huang, L. Fang, G. Chen, H. Wei, and Y. Fang, "Fano resonance assisting plasmonic circular dichroism from nanorice heterodimers for extrinsic chirality," *Scientific Reports*, vol. 5, p. 16069, 2015.

[21] L. Hu, X. Tian, Y. Huang, L. Fang, and Y. Fang, "Quantitatively analyzing the mechanism of giant circular dichroism in extrinsic plasmonic chiral nanostructures by tracking the interplay of electric and magnetic dipoles," *Nanoscale*, vol. 8, no. 6, pp. 3720–3728, 2016.

[22] A. Belardini, M. Centini, G. Leahu, D. C. Hooper, R. L. Voti, E. Fazio, J. W. Haus, A. Sarangan, V. K. Valev, R. Li Voti, E. Fazio, J. W. Haus, A. Sarangan, V. K. Valev, and C. Sibilia, "Chiral light intrinsically couples to extrinsic/pseudo-chiral metasurfaces made of tilted gold nanowires," *Scientific Reports*, vol. 6, p. 31796, 2016.

[23] V. K. Valev, J. J. Baumberg, B. De Clercq, N. Braz, X. Zheng, E. J. Osley, S. Vandendriessche, M. Hojeij, C. Blejean, J. Mertens, C. G. Biris, V. Volskiy, M. Ameloot, Y. Ekinci, G. A. E. Vandenbosch, P. A. Warburton, V. V. Moshchalkov, N. C. Panoiu, and T. Verbiest, "Nonlinear Superchiral Meta-Surfaces: Tuning Chirality and Disentangling Non-Reciprocity at the Nanoscale," *Advanced Materials*, vol. 26, no. 24, pp. 4074–4081, 2014.

[24] G. H. Tompkins, *Handbook of Ellipsometry*. Heidelberg: Springer Berlin Heidelberg, 2005.

[25] S. V. Gaponenko, *Introduction to Nanophotonics*. Cambridge: Cambridge University Press, 2010.

[26] F. Capolino, *Theory and Phenomena of Metamaterials*, vol. 8. CRC Press, 2009.

[27] R. Mohammadi-Baghaee and J. Rashed-Mohassel, "The Chirality Parameter for Chiral Chemical Solutions," *Journal of Solution Chemistry*, vol. 45, no. 8, pp. 1171–1181, 2016.

[28] Q. Zhang and J. Li, "Characteristics of surface plasmon polaritons in a dielectrically chiral-metal-chiral waveguiding structure," *Optics Letters*, vol. 41, no. 14, p. 3241, 2016.

[29] S. S. Oh and O. Hess, "Chiral metamaterials: enhancement and control of optical activity and circular dichroism," *Nano Convergence*, vol. 2, no. 1, p. 24, 2015.

[30] C.-W. Qiu, N. Burokur, S. Zouhdi, and L.-W. Li, "Chiral nihility effects on energy flow in chiral materials," *Journal of the Optical Society of America A*, vol. 25, no. 1, p. 55, 2008.

[31] Y. K. Sirenko, *Modern Theory of Gratings*, vol. 153 of *Springer Series in Optical Sciences*, pp. 361–364. New York, NY: Springer New York, 2010.

[32] J. B. Pendry, "Negative Refraction Makes a Perfect Lens," *Physical Review Letters*, vol. 85, no. 18, pp. 3966–3969, 2000.

[33] J. B. B. Pendry, "A Chiral Route to Negative Refraction," *Science*, vol. 306, no. 5700, pp. 1353–5, 2004.

[34] M. C. K. Wiltshire, J. B. Pendry, and J. V. Hajnal, "Chiral Swiss rolls show a negative refractive index," *Journal of Physics: Condensed Matter*, vol. 21, no. 29, p. 292201, 2009.

[35] S. Zhang, H. Wei, K. Bao, U. Håkanson, N. J. Halas, P. Nordlander, and H. Xu, "Chiral surface plasmon polaritons on metallic nanowires," *Physical Review Letters*, vol. 107, no. 9, pp. 1–5, 2011.

[36] A. O. Govorov, Z. Fan, P. Hernandez, J. M. Slocik, and R. R. Naik, "Theory of Circular Dichroism of Nanomaterials Comprising Chiral Molecules and Nanocrystals: Plasmon Enhancement, Dipole Interactions, and Dielectric Effects," *Nano Letters*, vol. 10, no. 4, pp. 1374–1382, 2010.

[37] J. M. Slocik, A. O. Govorov, and R. R. Naik, "Plasmonic circular dichroism of peptide-functionalized gold nanoparticles," *Nano Letters*, vol. 11, no. 2, pp. 701–705, 2011.

[38] P. J. Stephens, "Theory of vibrational circular dichroism," *The Journal of Physical Chemistry*, vol. 89, no. 5, pp. 748–752, 1985.

[39] T. B. Freedman, X. Cao, R. K. Dukor, and L. a. Nafie, "Absolute configuration determination of chiral molecules in the solution state using vibrational circular dichroism.," *Chirality*, vol. 15, no. 9, pp. 743–758, 2003.

[40] H. Takechi, O. Arteaga, J. M. Ribo, and H. Watarai, "Chiroptical measurement of chiral aggregates at liquid-liquid interface in centrifugal liquid membrane cell by mueller matrix and conventional circular dichroism methods," *Molecules*, vol. 16, no. 5, pp. 3636–3647, 2011.

[41] C. Helgert, E. Pshenay-Severin, M. Falkner, C. Menzel, C. Rockstuhl, E. B. Kley, A. Tünnermann, F. Lederer, and T. Pertsch, "Chiral metamaterial composed of three-dimensional plasmonic nanostructures," *Nano Letters*, vol. 11, no. 10, pp. 4400–4404, 2011.

[42] M. Esposito, V. Tasco, F. Todisco, A. Benedetti, I. Tarantini, M. Cuscunà, L. Dominici, M. De Giorgi, and A. Passaseo, "Tailoring chiro-optical effects by helical nanowire arrangement," *Nanoscale*, vol. 7, no. 43, pp. 18081–18088, 2015.

[43] M. Decker, R. Zhao, C. M. M. Soukoulis, S. Linden, and M. Wegener, "Twisted split-ring-resonator photonic metamaterial with huge optical activity.," *Optics letters*, vol. 35, no. 10, pp. 1593–1595, 2010.

[44] T. Narushima, S. Hashiyada, and H. Okamoto, "Nanoscopic Study on Developing Optical Activity with Increasing Chirality for Two-Dimensional Metal Nanostructures," *ACS Photonics*, pp. 732–738, 2014.

[45] K. Chaudhari and T. Pradeep, "Optical rotation by plasmonic circular dichroism of isolated gold nanorod aggregates," *Applied Physics Letters*, vol. 105, no. 20, 2014.

[46] L. Silvestroni, K. N. H. C. A. Hunter, M. J. K. J. Lehn, S. V. L. M. Olivucci, J. T. M. Venturi, and C. W. H. W. H. Yamamoto, *Electronic and Magnetic Properties of Chiral Molecules and Supramolecular Architectures*, vol. 298 of *Topics in Current Chemistry*. Berlin, Heidelberg: Springer Berlin Heidelberg, 2011.

[47] F. Bai, J. Deng, M. Yang, J. Fu, J. Ng, and Z. Huang, "Two chiroptical modes of silver nanospirals," *Nanotechnology*, vol. 27, no. 11, p. 115703, 2016.

[48] A. Painelli, F. Terenziani, L. Angiolini, T. Benelli, and L. Giorgini, "Chiral interactions in azobenzene dimers: a combined experimental and theoretical study.," *Chemistry (Weinheim an der Bergstrasse, Germany)*, vol. 11, no. 20, pp. 6053–63, 2005.

[49] N. Nishida, Y. Kojima, and H. Tanaka, "Intense Plasmon-induced Cotton Effects in Colloidal Silver Triangular Nanoplates Synthesized by a Ligand-exchange Process," *Chemistry Letters*, vol. 43, no. 8, pp. 1227–1229, 2014.

[50] W. Kuhn, "The physical significance of optical rotatory power," *Transactions of the Faraday Society*, vol. 26, p. 293, 1930.

[51] H. L. Lord, W. Zhan, J. Pawliszyn, S. A. Maier, H. L. Lord, W. Zhan, and J. Pawliszyn, *Plasmonics: Fundamentals and Applications*, vol. 677. Boston, MA: Springer US, 2007.

[52] F. Intravaia and A. Lambrecht, "Surface Plasmon Modes and the Casimir Energy," *Physical Review Letters*, vol. 94, no. 11, p. 110404, 2005.

[53] C. J. Murphy, T. K. Sau, A. M. Gole, C. J. Orendorff, J. Gao, L. Gou, S. E. Hunyadi, and T. Li, "Anisotropic metal nanoparticles: Synthesis, assembly, and optical applications," *Journal of Physical Chemistry B*, vol. 109, no. 29, pp. 13857–13870, 2005.

[54] X. Wang and Z. Tang, "Circular Dichroism Studies on Plasmonic Nanostructures," *Small*, vol. 13, no. 1, p. 1601115, 2017.

[55] H. J. Pain, *The Physics of Vibrations and Waves*. Chichester, UK: John Wiley & Sons, Ltd, 2005.

[56] J. D. Jackson, *Classical electrodynamics*. New York ; Chichester: Wiley, 3rd ed. ed., 1999.

[57] K. A. Willets, R. P. Van Duyne, R. V. Duyne, and R. P. Van Duyne, "Localized Surface Plasmon Resonance Spectroscopy and Sensing," *Annual Review of Physical Chemistry*, vol. 58, no. 1, pp. 267–297, 2007.

[58] S. Yoo and Q.-H. Park, "Enhancement of Chiroptical Signals by Circular Differential Mie Scattering of Nanoparticles," *Scientific Reports*, vol. 5, p. 14463, 2015.

[59] C. Dahmen, B. Schmidt, and G. von Plessen, "Radiation Damping in Metal Nanoparticle Pairs," *Nano Letters*, vol. 7, no. 2, pp. 318–322, 2007.

[60] A. M. Funston, C. Novo, T. J. Davis, and P. Mulvaney, "Plasmon Coupling of Gold Nanorods at Short Distances and in Different Geometries," *Nano Letters*, vol. 9, no. 4, pp. 1651–1658, 2009.

[61] S. Linic, U. Aslam, C. Boerigter, and M. Morabito, "Photochemical transformations on plasmonic metal nanoparticles," *Nature Materials*, vol. 14, no. 6, pp. 567–576, 2015.

[62] S. P. Rodrigues, S. Lan, L. Kang, Y. Cui, and W. Cai, "Nonlinear imaging and spectroscopy of chiral metamaterials," *Advanced Materials*, pp. 6157–6162, 2014.

[63] H. Kim, H.-B.-R. Lee, and W.-J. Maeng, "Applications of atomic layer deposition to nanofabrication and emerging nanodevices," *Thin Solid Films*, vol. 517, no. 8, pp. 2563–2580, 2009.

[64] Y.-L. Zhang, Q.-D. Chen, H. Xia, and H.-B. Sun, "Designable 3D nanofabrication by femtosecond laser direct writing," *Nano Today*, vol. 5, no. 5, pp. 435–448, 2010.

[65] X. Ye and L. Qi, "Two-dimensionally patterned nanostructures based on monolayer colloidal crystals: Controllable fabrication, assembly, and applications," *Nano Today*, vol. 6, no. 6, pp. 608–631, 2011.

[66] D. C. O'Shea, T. J. Suleski, A. D. Kathman, and D. W. Prather, *Diffractive Optics: Design, Fabrication, and Test*. 1000 20th Street, Bellingham, WA 98227-0010 USA: SPIE, 2003.

[67] E. Hecht, *Optics: Pearson New International Edition*. Pearson, 4 ed., 2013.

[68] C. B. Kress and P. Meyrueis, *Applied Digital Optics: From Micro-optics to Nanophotonics*. Chichester: John Wiley & Sons, 2009.

[69] J. R. Marciante, N. O. Farmiga, J. I. Hirsh, M. S. Evans, and H. T. Ta, "Optical measurement of depth and duty cycle for binary diffraction gratings with subwavelength features," *Applied Optics*, vol. 42, no. 16, p. 3234, 2003.

[70] H.-T. Chen, A. J. Taylor, and N. Yu, "A review of metasurfaces: physics and applications," *Reports on Progress in Physics*, vol. 79, no. 7, p. 076401, 2016.

[71] N. Yu, P. Genevet, M. A. Kats, F. Aieta, J.-P. Tetienne, F. Capasso, and Z. Gaburro, "Light Propagation with Phase Discontinuities: Generalized Laws of Reflection and Refraction," *Science*, vol. 334, no. 6054, pp. 333–337, 2011.

[72] C. Williams, R. Bartholomew, G. Rughoobur, G. S. D. Gordon, A. J. Flewitt, and T. D. Wilkinson, "Fabrication of nanostructured transmissive optical devices on ITO-glass with UV1116 photoresist using high-energy electron beam lithography," *Nanotechnology*, vol. 27, no. 48, p. 485301, 2016.

[73] N. C. Lindquist, P. Nagpal, K. M. McPeak, D. J. Norris, and S.-H. Oh, "Engineering metallic nanostructures for plasmonics and nanophotonics," *Reports on Progress in Physics*, vol. 75, no. 3, p. 036501, 2012.

[74] V. K. Valev, "Characterization of Nanostructured Plasmonic Surfaces with Second Harmonic Generation," *Langmuir*, vol. 28, no. 44, pp. 15454–15471, 2012.

[75] Y. Chen, "Nanofabrication by electron beam lithography and its applications: A review," *Microelectronic Engineering*, vol. 135, pp. 57–72, 2015.

[76] H. J. Pain, *The Physics of Vibrations and Waves*. Chichester, UK: John Wiley & Sons, Ltd, 2005.

[77] T. Zentgraf, T. P. Meyrath, A. Seidel, S. Kaiser, H. Giessen, C. Rockstuhl, and F. Lederer, "Babinet's principle for optical frequency metamaterials and nanoantennas," *Physical Review B*, vol. 76, no. 3, p. 033407, 2007.

[78] R. P. R. P. Feynman, *The Feynman lectures on physics. Vol. 1, Mainly mechanics, radiation, and heat.* San Francisco ; London: Pearson/Addison-Wesley, definitive ed., 2006.

[79] L. Liu, X. Zhang, M. Kenney, X. Su, N. Xu, C. Ouyang, Y. Shi, J. Han, W. Zhang, and S. Zhang, "Broadband metasurfaces with simultaneous control of phase and amplitude," *Advanced Materials*, vol. 26, no. 29, pp. 5031–5036, 2014.

[80] A. Pors, O. Albrektsen, I. P. Radko, and S. I. Bozhevolnyi, "Gap plasmon-based metasurfaces for total control of reflected light," *Scientific Reports*, vol. 3, no. 1, p. 2155, 2013.

[81] V. V. Klimov, I. V. Zabkov, A. A. Pavlov, R. C. Shiu, H. C. Chan, and G. Y. Guo, "Manipulation of polarization and spatial properties of light beams with chiral metafilms," *Optics Express*, vol. 24, no. 6, p. 6172, 2016.

[82] Y. Shindo and M. Nakagawa, "Circular dichroism measurements. I. Calibration of a circular dichroism spectrometer," *Review of Scientific Instruments*, vol. 56, no. 1, pp. 32–39, 1985.

[83] P. A. Korevaar, S. J. George, A. J. Markvoort, M. M. J. Smulders, P. A. J. Hilbers, A. P. H. J. Schenning, T. F. A. De Greef, and E. W. Meijer, "Pathway complexity in supramolecular polymerization," *Nature*, vol. 481, no. 7382, pp. 492–496, 2012.

[84] J. Li and N. A. Kotov, "Circular extinction of plasmonic silver nanocaps and gas sensing," *Royal Society of chemistry*, vol. 186, pp. 345–352, 2016.

[85] "Chirascan website." https://www.photophysics.com/systems/chirascan-systems/chirascan/system-information [2019-01-01], 2019.

[86] "Chirascan manual." http://people.bath.ac.uk/gp304/cd/manuals/Chirascan/Chirascan_Series_User_Manual.pdf [2019-01-01], 2019.

[87] A. Franzen, "Components Library." http://www.gwoptics.org/ComponentLibrary [2019-01-01], 2019.

[88] R. W. Boyd, "Nonlinear Optics," No. 3rd, pp. 108–122, Orlando: Elsevier, 2003.

[89] "Inspire laser Website." https://www.spectra-physics.com/products/ultrafast-lasers/inspire [2019-01-01], 2019.

[90] G. H. Tompkins, "Handbook of Ellipsometry," pp. 45–66, Heidelberg: Springer Berlin Heidelberg, 2005.

[91] B. M. Maoz, Y. Chaikin, A. B. Tesler, O. Bar Elli, Z. Fan, A. O. Govorov, and G. Markovich, "Amplification of chiroptical activity of chiral biomolecules by surface plasmons," *Nano Letters*, vol. 13, no. 3, pp. 1203–1209, 2013.

[92] G. D. Pantoş, P. Pengo, and J. K. M. Sanders, "Hydrogen-Bonded Helical Organic Nanotubes," *Angewandte Chemie International Edition*, vol. 46, no. 1-2, pp. 194–197, 2007.

[93] A. G. Mark, J. G. Gibbs, T.-C. Lee, and P. Fischer, "Hybrid nanocolloids with programmed three-dimensional shape and material composition.," *Nature materials*, vol. 12, no. 9, pp. 802–7, 2013.

[94] S. Murugkar, I. De Leon, M. Horton, H. Qassim, J. Leach, and R. W. Boyd, "Planar chiral metamaterials for biosensing applications," *Spie*, vol. 8597, p. 85970Y, 2013.

[95] R. Y. Wang, P. Wang, Y. Liu, W. Zhao, D. Zhai, X. Hong, Y. Ji, X. Wu, F. Wang, D. Zhang, W. Zhang, R. Liu, and X. Zhang, "Experimental observation of giant chiroptical amplification of small chiral molecules by gold nanosphere clusters," *Journal of Physical Chemistry C*, vol. 118, no. 18, pp. 9690–9695, 2014.

[96] R. Kuroda, T. Harada, and Y. Shindo, "A solid-state dedicated circular dichroism spectrophotometer: Development and application," *Review of Scientific Instruments*, vol. 72, no. 10, pp. 3802–3810, 2001.

[97] O. Arteaga, Z. El-Hachemi, A. Canillas, and J. M. Ribó, "Transmission Mueller matrix ellipsometry of chirality switching phenomena," *Thin Solid Films*, vol. 519, no. 9, pp. 2617–2623, 2011.

[98] O. Arteaga, "Useful Mueller matrix symmetries for ellipsometry," *Thin Solid Films*, vol. 571, no. P3, pp. 584–588, 2014.

[99] K. Postava, R. Sýkora, D. Legut, and J. Pištora, "Determination of Anisotropic Crystal Optical Properties Using Mueller Matrix Spectroscopic Ellipsometry," *Procedia Materials Science*, vol. 12, pp. 118–123, 2016.

[100] M. Hentschel, M. Schäferling, X. Duan, H. Giessen, and N. Liu, "Chiral plasmonics," *Science Advances*, vol. 3, no. 5, p. e1602735, 2017.

[101] Y. Zhao, A. N. Askarpour, L. Sun, J. Shi, X. Li, and A. Alù, "Chirality detection of enantiomers using twisted optical metamaterials," *Nature Communications*, vol. 8, p. 14180, 2017.

[102] L.-Y. Y. Y. Wang, K. W. W. Smith, S. Dominguez-Medina, N. Moody, J. M. M. Olson, H. Zhang, W.-S. S. S. Chang, N. Kotov, and S. Link, "Circular Differential Scattering of Single Chiral Self-Assembled Gold Nanorod Dimers," *ACS Photonics*, vol. 2, no. 11, pp. 1602–1610, 2015.

[103] J. Kaschke, L. Blume, L. Wu, M. Thiel, K. Bade, Z. Yang, and M. Wegener, "A Helical Metamaterial for Broadband Circular Polarization Conversion," *Advanced Optical Materials*, vol. 3, no. 10, pp. 1411–1417, 2015.

[104] A. V. Kondratov, M. V. Gorkunov, A. N. Darinskii, R. V. Gainutdinov, O. Y. Rogov, A. A. Ezhov, and V. V. Artemov, "Extreme optical chirality of plasmonic nanohole arrays due to chiral Fano resonance," *Physical Review B - Condensed Matter and Materials Physics*, vol. 93, no. 19, pp. 1–10, 2016.

[105] J. R. Brandt, X. Wang, Y. Yang, A. J. Campbell, and M. J. Fuchter, "Circularly Polarized Phosphorescent Electroluminescence with a High Dissymmetry Factor from PHOLEDs Based on a Platinahelicene," *Journal of the American Chemical Society*, vol. 138, no. 31, pp. 9743–9746, 2016.

[106] S. Allenmark, "Induced circular dichroism by chiral molecular interaction," *Chirality*, vol. 15, no. 5, pp. 409–422, 2003.

[107] Z. Fan and A. O. Govorov, "Plasmonic Circular Dichroism of Chiral Metal Nanoparticle Assemblies," *Nano Letters*, vol. 10, no. 7, pp. 2580–2587, 2010.

[108] J. M. Stone and J. C. Knight, "Visibly "white" light generation in uniform photonic crystal fiber using a microchip laser.," *Optics express*, vol. 16, no. 4, pp. 2670–5, 2008.

[109] J. Stirling, "LabDo:Base code." https://gitlab.com/jtc42/LabDo [2019-01-01], 2019.

[110] J. T. Collins, "LabDo:Adapted version." https://gitlab.com/jtc42/LabDo-CD-Spectrometer [2019-01-01], 2019.

[111] A. Potts, W. Zhang, and D. M. Bagnall, "Nonreciprocal diffraction through dielectric gratings with two-dimensional chirality," *Physical Review A*, vol. 77, no. 4, p. 043816, 2008.

[112] B. Frank, X. Yin, M. Schäferling, J. Zhao, S. M. Hein, P. V. Braun, and H. Giessen, "Large-area 3D chiral plasmonic structures," *ACS Nano*, vol. 7, no. 7, pp. 6321–6329, 2013.

[113] F. Fang, Y. Cheng, and H. Liao, "Giant optical activity and circular dichroism in the terahertz region based on bi-layer Y-shaped chiral metamaterial," *Optik*, vol. 125, no. 20, pp. 6067–6070, 2014.

[114] T. Kuroda, Reiko and Harada, "Solid-State Chiroptical Spectroscopy: Principles and Applications," in *Comprehensive Chiroptical Spectroscopy*, pp. 91–113, John Wiley & Sons, Inc., 2012.

[115] Z. Fan and A. O. Govorov, "Helical Metal Nanoparticle Assemblies with Defects : Plasmonic Chirality and Circular Dichroism Helical Metal Nanoparticle Assemblies with Defects : Plasmonic Chirality and Circular Dichroism," *The Journal of Physical Chemistry C*, vol. 115, no. 27, pp. 13254–13261, 2011.

[116] W. Zhang, A. Potts, and D. M. Bagnall, "Giant optical activity in dielectric planar metamaterials with two-dimensional chirality," *Journal of Optics A: Pure and Applied Optics*, vol. 8, no. 10, pp. 878–890, 2006.

[117] K. Hannam, D. A. Powell, I. V. Shadrivov, and Y. S. Kivshar, "Broadband chiral metamaterials with large optical activity," *Physical Review B - Condensed Matter and Materials Physics*, vol. 89, no. 12, pp. 1–6, 2014.

[118] S.-C. Jiang, X. Xiong, Y.-S. Hu, S.-W. Jiang, Y.-H. Hu, D.-H. Xu, R.-W. Peng, and M. Wang, "High-efficiency generation of circularly polarized light via symmetry-induced anomalous reflection," *Physical Review B*, vol. 91, no. 12, p. 125421, 2015.

[119] K. Hannam, D. A. Powell, I. V. Shadrivov, and Y. S. Kivshar, "Dispersionless optical activity in metamaterials," *Applied Physics Letters*, vol. 102, no. 20, p. 201121, 2013.

[120] Z. Li, K. B. Alici, E. Colak, and E. Ozbay, "Complementary chiral metamaterials with giant optical activity and negative refractive index," *Applied Physics Letters*, vol. 98, no. 16, p. 161907, 2011.

[121] W. Gao and W. Y. Tam, "Optical activities in complementary double layers of six-armed metallic gammadion structures," *Journal of Optics*, vol. 13, no. 1, p. 015101, 2011.

[122] M. Hentschel, T. Weiss, S. Bagheri, and H. Giessen, "Babinet to the half: Coupling of solid and inverse plasmonic structures," *Nano Letters*, vol. 13, no. 9, pp. 4428–4433, 2013.

[123] "Lumerical website." https://www.lumerical.com [2019-01-01], 2019.

[124] D. Lin, P. Fan, E. Hasman, and M. L. Brongersma, "Dielectric gradient metasurface optical elements," *Science*, vol. 345, no. 6194, pp. 298–302, 2014.

[125] A. Potts, W. Zhang, and D. M. Bagnall, "A new polarimeter based on optical non-reciprocity in gratings with two-dimensional chirality," *Applied Physics B*, vol. 99, no. 4, pp. 679–693, 2010.

[126] P. Pagliusi, C. Provenzano, A. Mazzulla, L. Giorgini, and G. Cipparrone, "Spectrograph Based on a Single Diffractive Element for Real-Time Measurement of Circular Dichroism," *Applied Spectroscopy*, vol. 62, no. 5, pp. 465–468, 2008.

[127] Y. Tanaka, S. P. Collins, S. W. Lovesey, M. Matsumami, T. Moriwaki, and S. Shin, "Determination of the absolute chirality of tellurium using resonant diffraction with circularly polarized x-rays," *Journal of Physics: Condensed Matter*, vol. 22, no. 12, p. 122201, 2010.

[128] V. K. Valev, N. Smisdom, A. V. Silhanek, B. De Clercq, W. Gillijns, M. Ameloot, V. V. Moshchalkov, and T. Verbiest, "Plasmonic ratchet wheels: Switching circular dichroism by arranging chiral nanostructures," *Nano Letters*, vol. 9, no. 11, pp. 3945–3948, 2009.

[129] B. Bai, Y. Svirko, J. Turunen, and T. Vallius, "Optical activity in planar chiral metamaterials: Theoretical study," *Physical Review A*, vol. 76, no. 2, p. 023811, 2007.

[130] T. Roy, A. E. Nikolaenko, and E. T. F. Rogers, "A meta-diffraction-grating for visible light," *Journal of Optics*, vol. 15, no. 8, p. 085101, 2013.

[131] B. K. Canfield, S. Kujala, K. Laiho, K. Jefimovs, J. Turunen, and M. Kauranen, "Chirality arising from small defects in gold nanoparticle arrays," *Optics Express*, vol. 14, no. 2, p. 950, 2006.

[132] K. Konishi, B. Bai, Y. Toya, J. Turunen, Y. P. Svirko, and M. Kuwata-Gonokami, "Surface-plasmon enhanced optical activity in two-dimensional metal chiral networks," *Optics Letters*, vol. 37, no. 21, p. 4446, 2012.

[133] H. Zhang and A. O. Govorov, "Giant circular dichroism of a molecule in a region of strong plasmon resonances between two neighboring gold nanocrystals," *Physical Review B*, vol. 87, no. 7, p. 075410, 2013.

[134] I. De Leon, M. J. Horton, S. A. Schulz, J. Upham, P. Banzer, and R. W. Boyd, "Strong, spectrally-tunable chirality in diffractive metasurfaces," *Scientific Reports*, vol. 5, p. 13034, 2015.

[135] S. N. Volkov, K. Dolgaleva, R. W. Boyd, K. Jefimovs, J. Turunen, Y. Svirko, B. K. Canfield, and M. Kauranen, "Optical activity in diffraction from a planar array of achiral nanoparticles," *Physical Review A*, vol. 79, no. 4, p. 043819, 2009.

[136] J. García-Guirado, M. Svedendahl, J. Puigdollers, and R. Quidant, "Enantiomer-Selective Molecular Sensing Using Racemic Nanoplasmonic Arrays," *Nano Letters*, vol. 18, no. 10, pp. 6279–6285, 2018.

[137] G. K. Larsen, Y. He, W. Ingram, and Y. Zhao, "Hidden Chirality in Superficially Racemic Patchy Silver Films," *Nano Letters*, vol. 13, no. 12, pp. 6228–6232, 2013.

[138] Y. He, K. Lawrence, W. Ingram, and Y. Zhao, "Strong Local Chiroptical Response in Racemic Patchy Silver Films: Enabling a Large-Area Chiroptical Device," *ACS Photonics*, vol. 2, no. 9, pp. 1246–1252, 2015.

[139] M. Schäferling, "Chiral Nanophotonics," in *Springer Series in Optical Sciences*, vol. 205 of *Springer Series in Optical Sciences*, pp. 87–100, Cham: Springer International Publishing, 2017.

[140] A. Papakostas, A. Potts, D. M. Bagnall, S. L. Prosvirnin, H. J. Coles, and N. I. Zheludev, "Optical Manifestations of Planar Chirality," *Physical Review Letters*, vol. 90, no. 10, p. 107404, 2003.

[141] S. L. Prosvirnin and N. I. Zheludev, "Polarization effects in the diffraction of light by a planar chiral structure," *Physical Review E*, vol. 71, no. 3, p. 037603, 2005.

[142] P. B. Johnson and R. W. Christy, "Optical Constants of the Noble Metals," *Physical Review B*, vol. 6, no. 12, pp. 4370–4379, 1972.

[143] E. Palik, *Handbook of Optical Constants of Solids*. Academic Press, 1998.

[144] M. S. Dresselhaus, G. Dresselhaus, and A. Jorio, *Group Theory: Application to the Physics of Condensed Matter*. Berlin, Heidelberg: Springer Berlin Heidelberg, 2008.

[145] X. Zheng, V. K. Valev, N. Verellen, Y. Jeyaram, A. V. Silhanek, V. Metlushko, M. Ameloot, G. A. E. Vandenbosch, and V. V. Moshchalkov, "Volumetric

Method of Moments and Conceptual Multilevel Building Blocks for Nanotopologies," *IEEE Photonics Journal*, vol. 4, no. 1, pp. 267–282, 2012.

[146] X. Zheng, V. Volskiy, V. K. Valev, G. A. E. Vandenbosch, and V. V. Moshchalkov, "Line Position and Quality Factor of Plasmonic Resonances Beyond the Quasi-Static Limit: A Full-Wave Eigenmode Analysis Route," *IEEE Journal of Selected Topics in Quantum Electronics*, vol. 19, no. 3, pp. 4600908–4600908, 2013.

[147] X. Zheng, V. K. Valev, N. Verellen, V. Volskiy, L. O. Herrmann, P. Van Dorpe, J. J. Baumberg, G. A. E. Vandenbosch, and V. V. Moschchalkov, "Implementation of the Natural Mode Analysis for Nanotopologies Using a Volumetric Method of Moments (V-MoM) Algorithm," *IEEE Photonics Journal*, vol. 6, no. 4, pp. 1–13, 2014.

[148] X. Zheng, N. Verellen, D. Vercruysse, V. Volskiy, P. Van Dorpe, G. A. E. Vandenbosch, and V. Moshchalkov, "On the Use of Group Theory in Understanding the Optical Response of a Nanoantenna," *IEEE Transactions on Antennas and Propagation*, vol. 63, no. 4, pp. 1589–1602, 2015.

[149] F. Cheng, X. Yang, and J. Gao, "Ultrasensitive detection and characterization of molecules with infrared plasmonic metamaterials.," *Scientific reports*, vol. 5, p. 14327, 2015.

[150] M. L. Nesterov, X. Yin, M. Schäferling, H. Giessen, and T. Weiss, "The Role of Plasmon-Generated Near Fields for Enhanced Circular Dichroism Spectroscopy," *ACS Photonics*, vol. 3, no. 4, pp. 578–583, 2016.

[151] D. M. Răsădean, T. M. Gianga, A. H. Swan, G. Kociok-Köhn, and G. D. Pantoş, "Chiral Phthalocyanines through Axial Coordination," *Organic Letters*, vol. 20, no. 9, pp. 2645–2648, 2018.

Appendices

A Scalar diffraction theory

The behaviour of light can be described by using Maxwell's equations. As before, the derivation will start from the vector form of Maxwell's equations. It will be demonstrated that a series of assumptions can be applied, which reduce the vector to their scalar form.

The aim of scalar diffraction theory is to provide a set of equations that describe the propagation of light between two planes – the aperture and the evaluation plane. Such a set of equations has a twofold advantage. First, if the complex transmission function of an optical element is known, it is possible to determine the light distribution at any distance beyond that optical element. Second, if the desired output is known, the inverse of those equations determine the form of the optical element that produces the necessary output [66].

For a system as shown in Figure 1, a version of Maxwell's equations can be used which does not use auxiliary fields, such that [66]:

$$\nabla \cdot \vec{E} = \frac{\rho}{\epsilon} \tag{1a}$$

$$\nabla \cdot \vec{B} = 0 \tag{1b}$$

$$\nabla \times \vec{E} = -\frac{\partial \vec{B}}{\partial t} \tag{1c}$$

$$\nabla \times \vec{B} = \mu\sigma\vec{E} + \mu\epsilon\frac{\partial \vec{E}}{\partial t}, \tag{1d}$$

where $\vec{E}$ and $\vec{B}$ are the electric and magnetic fields respectively, ρ is the charge density, μ the permeability, ϵ the permittivity and σ the conductivity.

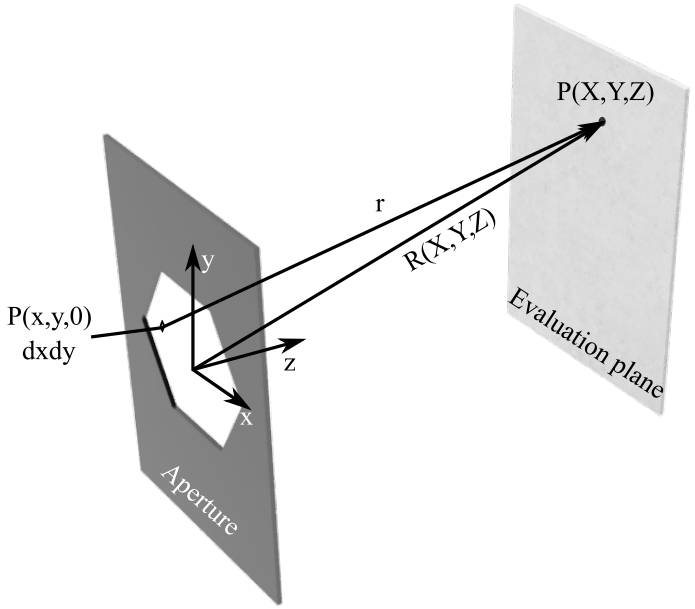

Figure 1: Scalar Diffraction Theory for an arbitrary aperture. Adapted from [66].

In order to allow light propagation in the medium, it is assumed that the medium is uncharged and nonconducting ($\rho = 0$, $\sigma = 0$). Furthermore, the medium is simplified to be homogeneous, uniform as well as isotropic, such that μ and ϵ are constant both spatially and temporally. Lastly, for linear materials, the permeability and permittivity do not change in the presence of electric and magnetic fields. These assumptions are valid for many optical materials [66]. If the material properties do change with time, this change is typically slow compared to the frequency of the light wave and can therefore be assumed to be negligible. While this is true for space, gases, most liquids and glasses, crystals are and therefore not all assumptions hold on the microscopic scale. However, scalar diffraction theory still provides a good approximation and further allows the qualitative description of diffraction-related phenomena.

So, taking these assumptions into account as well as applying suitable vector product identities, the resulting differential wave equations can be shown to take the form [66]:

$$\nabla^2 \vec{E} = \mu\epsilon \frac{\partial^2 \vec{E}}{\partial t^2} \qquad \nabla^2 \vec{B} = \mu\epsilon \frac{\partial^2 \vec{B}}{\partial t^2}, \tag{2}$$

the term on the right-hand side of these equations can be shown to be proportional to the inverse of the speed of the light in the medium, such that $v = \frac{1}{\sqrt{\mu\epsilon}}$. By definition, the index of refraction of a material is given by the ratio of the speed of light in vacuum c and in the material v, such that $n = \frac{c}{v} = c\sqrt{\mu\epsilon}$. Substituting this

into the vector equations (2), the resulting expressions can be separated into three scalar components of $\vec{E}$ and $\vec{B}$ respectively:

$$\frac{\partial^2 E_x}{\partial x^2} + \frac{\partial^2 E_x}{\partial y^2} + \frac{\partial^2 E_x}{\partial z^2} = \frac{n^2}{c^2}\frac{\partial E_x}{\partial t^2} \tag{3a}$$

$$\frac{\partial^2 B_x}{\partial x^2} + \frac{\partial^2 B_x}{\partial y^2} + \frac{\partial^2 B_x}{\partial z^2} = \frac{n^2}{c^2}\frac{\partial^2 B_x}{\partial t^2}. \tag{3b}$$

Similar expressions for E_y, E_z, B_y and B_z exist. Since each component obeys the scalar wave equation, it can be separated into its spatial and temporal terms, such that:

$$E_x = P_x e^{-\frac{\mathrm{i}kct}{n}}, \tag{4}$$

with P_x representing the spatial component of the electric field and k as the wave number, which by definition is $k = \frac{2\pi}{\lambda}$. Since the spatial behaviour of the wave is of more immediate concern for the modelling and are assumed not to change with time, the temporal term can usually be dropped [66]. The spatial behaviour is described by the Helmholtz equation:

$$\nabla^2 P + k^2 P = 0, \tag{5}$$

with P as the field integral over the aperture surface satisfying the *Kirchhoff integral*. Unfortunately, the Helmholtz equation cannot be solved in its current form and therefore additional simplifications have to be used.

Firstly, the light is propagating from a source, through the aperture plane and finally is calculated in the evaluation plane. Secondly, the aperture is large compared to the wavelength. And, finally, the distance from the aperture to the evaluation plane is large compared to the wavelength. While the size assumption is not valid for diffractive micro- and nanostructures, the knowledge of the complex transmission function can still be used in conjunction with the scalar diffraction theory to model the light propagation.

This can be shown to result in the *Rayleigh-Sommerfeld integral* [66]:

$$P(X,Y,Z) = \frac{1}{2\pi}\iint_{x,y} P(x,y,0)\,\frac{e^{-\mathrm{i}kr}}{r}\frac{Z}{r}\left(\mathrm{i}k + \frac{1}{r}\right)\,dx\,dy, \tag{6}$$

where $r = \left[(x-X)^2 + (y-Y)^2 + Z^2\right]^{\frac{1}{2}}$, represents the distance from a point in the aperture plane to the evaluation plane (Figure 1). Here, X, Y and Z refer to the coordinates of a point P in the evaluation plane.

The last approximation made, i.e. that the distance between the aperture and evaluation plane is large compared to the wavelength, is known as the *far-field*

approximation and can be used to further simplify the Rayleigh-Sommerfeld integral. Each infinitesimally small area of the DOE in the aperture plane is represented by $ds = dx\,dy$. Each of those areas contributes to the diffracted field P with a field amplitude density $E_u(x, y)$. Additionally, each wavefront segment generated by these areas can be represented as spherical wavelets, with $\frac{e^{ikr}}{r}$. The field contribution from each area is therefore given by:

$$dP(X, Y, Z) = \frac{E_u(x, y, 0)}{r} e^{\mathrm{i}(\omega t - kr)}\, ds. \tag{7}$$

If the distance from the origin to the evaluation point R is $r = [X^2 + Y^2 + Z^2]^{\frac{1}{2}}$, then the previous definition of r becomes:

$$r = R\left[1 + \frac{x^2 + y^2}{R^2} - 2\frac{xX + yY}{R^2}\right]^{\frac{1}{2}}. \tag{8}$$

In the far-field, the distance between the aperture and the evaluation plane is large, so $R^2 >> x^2 + y^2$. Thus, the second term in Equation (8) will be negligible and the expression can be approximated by:

$$r \approx R\left[1 - 2\frac{xX + yY}{R^2}\right]^{\frac{1}{2}}. \tag{9}$$

If a Taylor series expansion is applied, i.e. $r = R\sqrt{1 - x} \approx R\left(1 - \frac{x}{2}\right)$ and since $R^2 >> xX, yY$:

$$r = R - \frac{xX}{R} - \frac{yY}{R} = R - \alpha x - \beta y, \tag{10}$$

where $\alpha = \frac{X}{R}$ and $\beta = \frac{Y}{R}$. This means that the angles α and β are fixed, resulting in a far-field pattern growing linearly in size with increasing distance. These findings can be used to derive an expression of the diffraction pattern in the far-field. By integrating all contributions of (7) over the whole aperture area, this leads to:

$$P(X, Y, Z) = \int_{\text{aperture}} \frac{E_u(x, y, 0)}{r} e^{\mathrm{i}kr}\, dx\, dy. \tag{11}$$

Substituting the approximation for r:

$$P(X, Y, Z) = \int_{\text{aperture}} \frac{E_u(x, y, 0)}{R} e^{-\mathrm{i}kR} exp\left[-\mathrm{i}k\frac{xX}{R}\right] exp\left[-\mathrm{i}k\frac{yY}{R}\right] dx\, dy. \tag{12}$$

Furthermore, the exponential terms are connected to the Fourier transform, by defining two components of the wavevector $\vec{k}$ as:

$$k_X = \frac{\vec{k}X}{R} = \vec{k}\alpha \qquad\qquad k_Y = \frac{\vec{k}Y}{R} = \vec{k}\beta. \tag{13}$$

In addition, defining the complex amplitude in the aperture plane $u(x, y, 0)$ as:

$$u(x, y, 0) = \frac{E_u(x, y, 0)}{r} e^{-\mathrm{i}kr}. \tag{14}$$

It is now possible to express the far-field diffraction pattern in the form of the two-dimensional Fourier transform:

$$P(X, Y, Z) = \int_{\text{aperture}} u(x, y, 0) exp\left\{\mathrm{i}\phi_0(x, y) exp\left[-\mathrm{i}k\frac{xX}{R}\right] exp\left[-\mathrm{i}k\frac{yY}{R}\right]\right\} dx\, dy, \tag{15}$$

where the term $exp\left[\mathrm{i}\phi_0(x, y)\right]$ accounts for the phase variations over the aperture. This expression is sometimes also given in its compact form $P(X, Y, Z) = \mathcal{F}\left[u(x, y, 0) exp\left\{\mathrm{i}\phi_0(x, y)\right\}\right]$, which demonstrates that the far-field diffraction pattern is the Fourier transform of the aperture function [66].

B Measuring chirality in the far-field from a racemic nanomaterial: diffraction spectroscopy from plasmonic nanogratings

B.1 Robustness checks

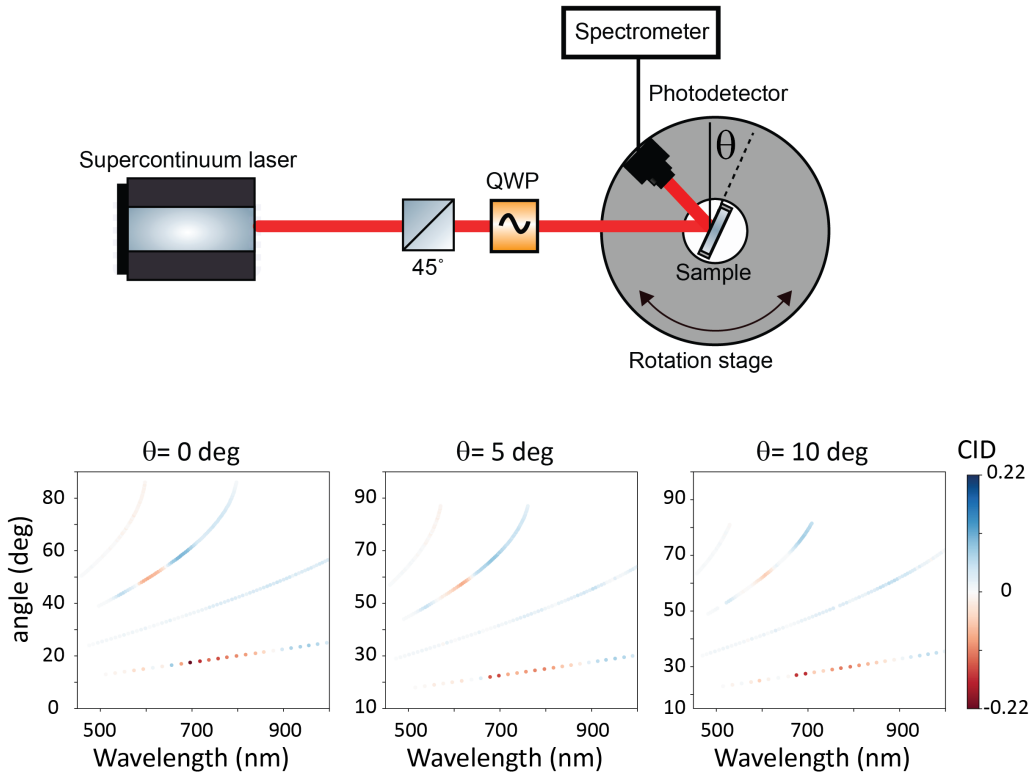

Figure 2: Circular intensity difference measured for racemic nanograting near-invariant under changed angle of incidence.

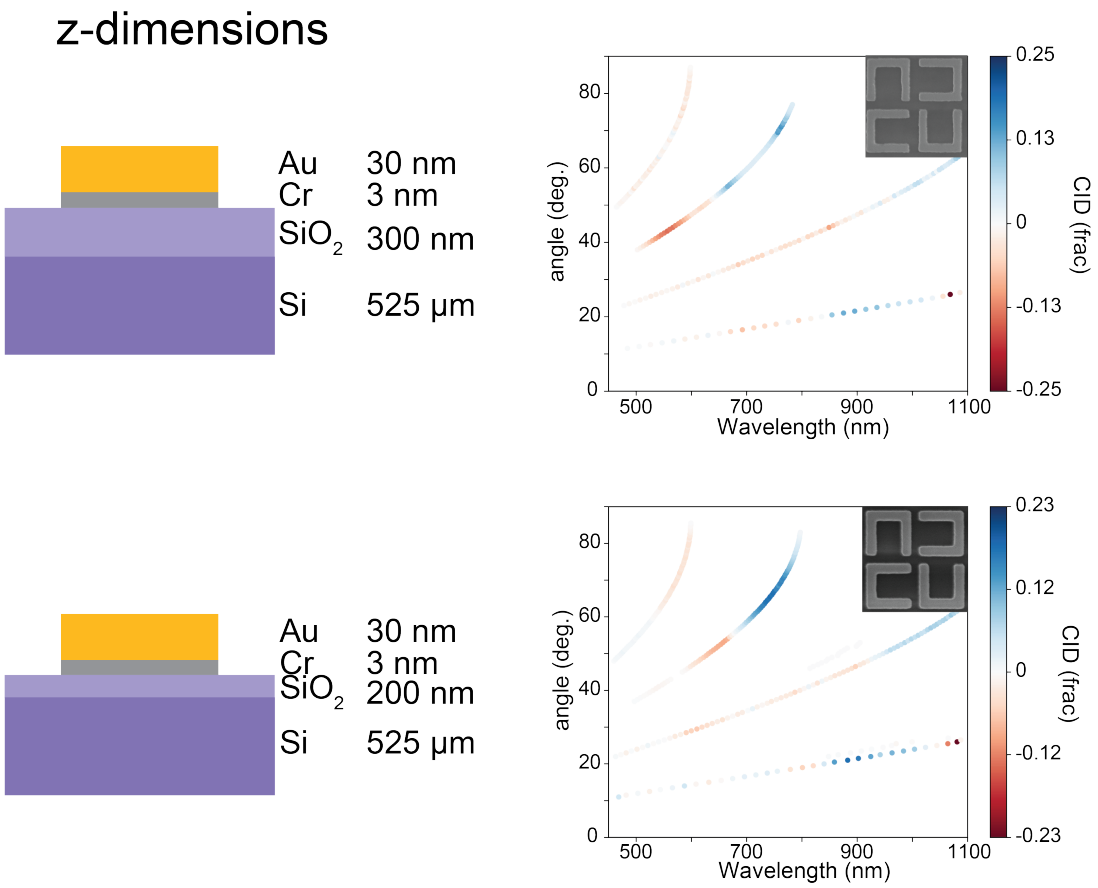

Figure 3: Effect of dioxide layer on chiroptical far-field response for U-shaped nanogratings. Two sets of nanogratings were fabricated – one with a dioxide layer thickness of 200 nm and one with a thickness of 300 nm. These samples were studied to unsure the invariance under different dioxide layer thicknesses. The results confirm that changing the dioxide layer thickness from 300 nm to 200 nm has no effect.

B.2 Additional Lumerical simulations

The following numerical simulations have been carried out by myself using Lumerical [123] to study the spectral response of the nanogratings upon varying the gold and chromium layer thicknesses. However since the total spectrum is calculated, the effect on the individual diffraction orders is not immediately obvious. It can be concluded that the overall effect on the reflected spectrum is insubstantial.

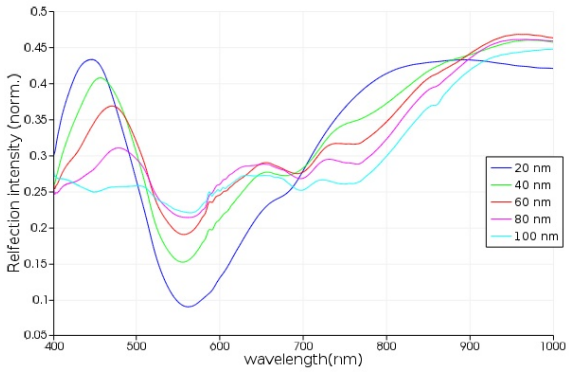

Figure 4: Numerical simulation studying the influence of the gold layer thickness on the reflected spectrum for the L-shape nanograting. The thickness was incremented in steps of 20 nm between 20 nm and 100 nm. The resulting spectra show a flattening of characteristic peaks with increasing gold layer thickness as well as a slight spectral red-shift of the reflection peak at $\approx$ 450 nm.

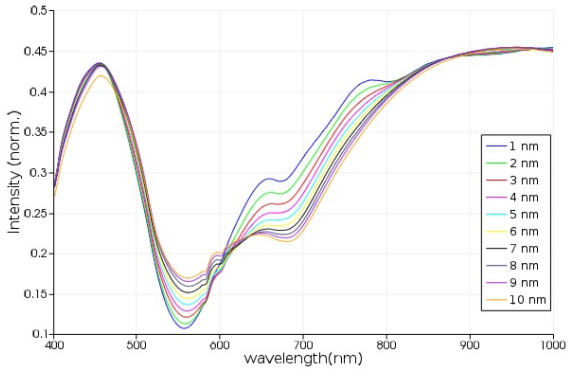

Figure 5: Numerical simulation studying the influence of the chromium layer thickness on the reflected spectrum for the L-shape nanograting. The chromium layer thickness was studied for a range between 1 - 10 nm, with 1 nm increments. The graph shows that with increasing chromium thickness, the absorption of lower wavelengths ($\lambda < 600$ nm) is reduced, while it increases for wavelengths $600 < \lambda < 800$ nm. For wavelengths in excess of 900 nm no net-effect is observed.

C Plasmonic nanogratings as a platform for enhanced molecular CID spectroscopy

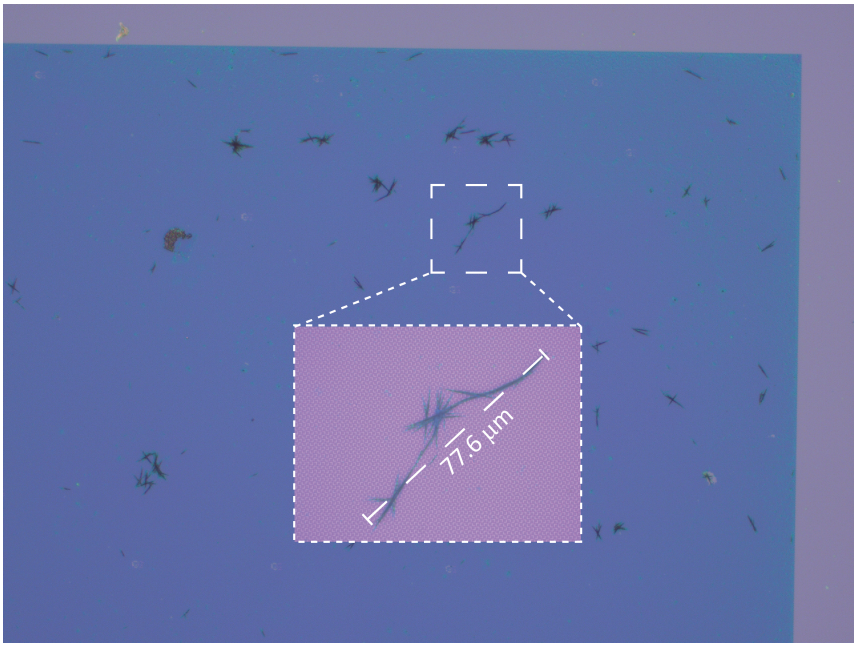

Figure 6: The effect of aggregation of the chiral molecule solution if stored for about 4 weeks. The microscope image shows the resulting layer on top of the racemic nanograting. While a layer has been created, various large black crystallised clusters are visible atop the nanograting area. The area framed by the white dashed lines has been magnified (using a 100x microscope objective) to inspect the cluster in more detail. This particular cluster is roughly 78 μm long and thus 32.5 times larger than the spatial period of the underlying nanograting which can be seen at this magnification as well.

D Figure permission

THE AMERICAN ASSOCIATION FOR THE ADVANCEMENT OF SCIENCE LICENSE TERMS AND CONDITIONS

Feb 07, 2019

This Agreement between University of Bath -- Christian Kuppe ("You") and The American Association for the Advancement of Science ("The American Association for the Advancement of Science") consists of your license details and the terms and conditions provided by The American Association for the Advancement of Science and Copyright Clearance Center.

License Number	4520680611054
License date	Feb 02, 2019
Licensed Content Publisher	The American Association for the Advancement of Science
Licensed Content Publication	Science
Licensed Content Title	Light Propagation with Phase Discontinuities: Generalized Laws of Reflection and Refraction
Licensed Content Author	Nanfang Yu,Patrice Genevet,Mikhail A. Kats,Francesco Aieta,Jean-Philippe Tetienne,Federico Capasso,Zeno Gaburro
Licensed Content Date	Oct 21, 2011
Licensed Content Volume	334
Licensed Content Issue	6054
Volume number	334
Issue number	6054
Type of Use	Thesis / Dissertation
Requestor type	Scientist/individual at a research institution
Format	Print and electronic
Portion	Figure
Number of figures/tables	1
Order reference number	
Title of your thesis / dissertation	Chirality in diffractive plasmonic nanostructures
Expected completion date	Feb 2019
Estimated size(pages)	120
Requestor Location	University of Bath Claverton Down Rd Bath, BA2 7AY United Kingdom Attn: Christian Kuppe
Billing Type	Invoice
Billing Address	University of Bath Claverton Down Rd Bath, United Kingdom BA2 7AY Attn: Christian Kuppe
Total	0.00 GBP
Terms and Conditions	

American Association for the Advancement of Science TERMS AND CONDITIONS